

UNIVERSITY OF CALIFORNIA  
Los Angeles

**Correlations with Non-Photonic Electrons in  
 $\sqrt{s_{NN}} = 200$  GeV AuAu Collisions in STAR**

A dissertation submitted in partial satisfaction  
of the requirements for the degree  
Doctor of Philosophy in Physics

by

**Lloyd Edward Dunkelberger Jr.**

2015

© Copyright by  
Lloyd Edward Dunkelberger Jr.  
2015

The dissertation of Lloyd Edward Dunkelberger Jr. is approved.

Lindley Winslow

Gang Li

Graciela Gelmini

Huan Huang, Committee Chair

University of California, Los Angeles

2015

## TABLE OF CONTENTS

<b>1</b>	<b>Introduction</b>	<b>1</b>
1.1	Quantum Chromodynamics	1
1.2	QCD Phase Diagram and Deconfinement	4
1.3	Experiments on QGP	6
1.3.1	Heavy Ion Collisions	6
1.3.2	Hadron Yields	7
1.3.3	Elliptic Flow	10
1.3.4	$R_{AA}$ and Jet Suppression	12
1.4	Heavy Flavor Probes	15
1.4.1	Motivation	15
1.4.2	Experimental Results	16
1.5	Heavy Flavor Two Particle Correlations	19
<b>2</b>	<b>Experimental Setup</b>	<b>25</b>
2.1	Relativistic Heavy Ion Collider	25
2.2	STAR Detector	27
2.3	Time Projection Chamber	29
2.4	Barrel Electromagnetic Calorimeter	32
2.4.1	EMC Towers	32
2.4.2	Shower Maximum Detector	34
<b>3</b>	<b>Identification of Non-photonic Electrons</b>	<b>36</b>
3.1	Outline of the NPE Identification	36

3.2	Dataset and Event Selection . . . . .	37
3.2.1	Data and Triggers . . . . .	37
3.2.2	Event Level Cuts . . . . .	39
3.3	Track Reconstruction and TPC Cuts . . . . .	40
3.4	BEMC Points and Matching . . . . .	42
3.5	Electron Identification . . . . .	44
3.5.1	BEMC Cuts . . . . .	46
3.5.2	TPC Cuts . . . . .	53
3.6	Electron Purity . . . . .	54
3.7	Photonic Electron Identification . . . . .	56
3.8	Photonic Electron Reconstruction Efficiency . . . . .	59
<b>4</b>	<b>Azimuthal Correlations of Non-Photonic Electrons to Hadrons</b>	<b>62</b>
4.1	Overview of Constructing the NPE-hadron Correlation . . . . .	62
4.2	Acceptance Corrections . . . . .	63
4.2.1	Single Particle $\phi$ -weighting . . . . .	63
4.2.2	Mixed Event Background . . . . .	66
4.3	Background from Flow . . . . .	67
4.3.1	Measurements of Flow . . . . .	67
4.3.2	Background Normalization . . . . .	69
4.4	Correlations in Au+Au . . . . .	70
4.4.1	Associated Hadrons . . . . .	70
4.4.2	Constructing the NPE-hadron correlation . . . . .	71
4.4.3	Raw Correlations . . . . .	73
4.4.4	Subtracted Distributions and Yields . . . . .	74

4.5	Correlations in p+p . . . . .	84
4.5.1	Data and Correlations . . . . .	85
4.5.2	Charm to Bottom Ratios . . . . .	88
4.6	Comparisons of Yields . . . . .	92
4.6.1	Away Side Shape . . . . .	92
4.6.2	$I_{AA}$ . . . . .	94
4.7	Event-Plane Dependent Correlations . . . . .	94
4.7.1	Event Plane Reconstruction . . . . .	97
4.7.2	Correlations . . . . .	102
5	Conclusion . . . . .	108
	References . . . . .	110

## LIST OF FIGURES

1.1	Asymptotic Freedom . . . . .	3
1.2	QCD Phase Diagram . . . . .	5
1.3	$p/T^4$ Calculations . . . . .	6
1.4	Hadron Yields . . . . .	8
1.5	Freeze-out T and $\mu_B$ . . . . .	9
1.6	NCQ Scaling of $v_2$ . . . . .	11
1.7	$R_{AA}$ for $\pi^0$ . . . . .	13
1.8	Jet Quenching is STAR . . . . .	14
1.9	NPE $R_{AA}$ . . . . .	17
1.10	NPE $v_2$ . . . . .	18
1.11	Correlations $c$ and $b$ at LHC Energies . . . . .	20
1.12	Two Particle Correlation from $c\bar{c}$ . . . . .	22
1.13	PHENIX e-h correlation . . . . .	24
2.1	RHIC Facility . . . . .	26
2.2	STAR Detector . . . . .	28
2.3	TPC Diagram . . . . .	30
2.4	TPC Sector . . . . .	31
2.5	BEMC Towers . . . . .	33
2.6	BSMD Diagram . . . . .	35
3.1	RHIC Integrated Luminosities in Run11 and Run12 . . . . .	38
3.2	TPC $V_z$ and TPC VPD Difference . . . . .	40
3.3	Refmult and Centrality Distributions . . . . .	41

3.4	SMD Point $\eta$ and $\phi$	45
3.5	ADC0 Distribution for NPE18	47
3.6	TPC to BEMC $\Delta\phi$	49
3.7	TPC to BEMC $\Delta Z$	50
3.8	SMD Strip Hits	51
3.9	$E/p$ in BEMC	52
3.10	Fits of $n\sigma_e$	55
3.11	Angle Cuts for Phot. Electrons	58
3.12	2D Invariant Mass	60
3.13	Invariant Mass	61
4.1	Phi distribution for all tracks in TPC.	64
4.2	$p_T$ dependence of $\phi$ acceptance	65
4.3	STAR measured hadron $v_2$	68
4.4	STAR NPE $v_2$	69
4.5	Associated hadron efficiency	72
4.6	Raw Correlations 40-60% Centrality	75
4.7	Raw Correlations 20-40% Centrality	76
4.8	Raw Correlations 0-10% Centrality	77
4.9	Subtracted Correlations 40-60% Centrality	78
4.10	Subtracted Correlations 20-40% Centrality	79
4.11	Subtracted Correlations 0-10% Centrality	80
4.12	NPE-hadron correlations in p+p	86
4.13	Raw and Weighted Pythia Generated Hard Processes	88
4.14	D/B Ratio Fit Example	90

4.15	B/D Ratio . . . . .	91
4.16	Shoulder and Head Region Yield Comparison . . . . .	93
4.17	Near Side $I_{AA}$ . . . . .	95
4.18	Away Side $I_{AA}$ . . . . .	96
4.19	$v_2$ and Event Plane Diagram . . . . .	98
4.20	Corrected Event Plane Distribution . . . . .	100
4.21	Event Plane Resolutions . . . . .	101
4.22	Raw NPE-hadron Correlations, In-plane and Out-of-plane . . . . .	104
4.23	Subtracted NPE-hadron Correlations, In-plane and Out-of-plane .	105
4.24	Event Plane Dependent Correlation Comparison . . . . .	107

## LIST OF TABLES

3.1	Dataset and Event Level Cuts . . . . .	39
3.2	Track Quality Cuts . . . . .	42
3.3	Electron Cuts . . . . .	53
3.4	$n\sigma_e$ Cuts . . . . .	54
3.5	Electron Purity . . . . .	56
3.6	Photonic Electron Cuts . . . . .	57
4.1	Associated hadron cuts . . . . .	71
4.2	Yields and Errors in Au+Au Correlations, 40-60%, Low Trigger .	81
4.3	Yields and Errors in Au+Au Correlations, 40-60%, High Trigger .	82
4.4	Yields and Errors in Au+Au Correlations, 20-40%, Low Trigger .	82
4.5	Yields and Errors in Au+Au Correlations, 20-40%, High Trigger .	83
4.6	Yields and Errors in Au+Au Correlations, 0-10%, Low Trigger .	83
4.7	Yields and Errors in Au+Au Correlations, 0-10%, High Trigger .	84
4.8	Yields and Errors in p+p Correlations, Low Trigger . . . . .	87
4.9	Yields and Errors in p+p Correlations, High Trigger . . . . .	87

# CHAPTER 1

## Introduction

### 1.1 Quantum Chromodynamics

Early theoretical work in nuclear physics, after the discovery of the neutron, focused on establishing a theory of the strong force, which is responsible for binding together protons and neutrons. The earliest model, that of Yukawa, relied on the exchange of a massive boson (the  $\pi$  meson). Later experiments looking at harder interactions between nucleons showed that these processes could produce a large variety of hadrons, pointing to a much richer structure within protons and neutrons. Thus it became necessary to think beyond the model of the nuclear force (protons and neutrons exchanging pions), and instead look at the more fundamental strong force which gives rise to the structure and interaction of all hadrons. In the 1960s the quark model was developed and successfully explained the multiple observations of new hadrons being created in collider experiments by supposing that hadrons were not fundamental particles, but rather composed of quarks.

Quantum Chromodynamics (QCD) is the fundamental theory of the strong force and describes the interactions between quarks which is mediated by gluons. Quarks come in 6 flavors: up, down, strange, charm, bottom, and top. All quarks have a fractional electric charge (either  $\pm\frac{1}{3}e$  or  $\pm\frac{2}{3}e$ ). Quarks carry a color (red, green, or blue) and are bound by gluons into groups of three (baryons) or two (mesons). Baryons and mesons have no color, in baryons the three colors add up in a way that is color neutral while in mesons the one quark carries a color and

the antiquark carries a corresponding anticolor.

Deep inelastic scattering (DIS) experiments at SLAC further probed the structure of nucleons and showed that they were composed of three spin-1/2 particles. These measurements confirmed the quark model and showed that quarks were real particles within hadrons. DIS experiments also suggested other peculiar and (at the time) unexpected behaviors in quarks. When bound quarks are probed at higher energy scales they behave as if they were free. In fact it is the case with quarks that with large momentum exchange the coupling between quarks and gluons is weak and we can treat QCD perturbatively. However as the energy scale decreases the coupling becomes stronger and perturbation theory no longer applies. This property of QCD is called asymptotic freedom and was discovered in 1973 by Gross, Wilczek, and Politzer for which they were awarded the Nobel Prize in 2004. Asymptotic freedom arises in QCD because it is a non-Abelian gauge theory. There is screening of the color charge of quarks by the vacuum, however there is also anti-screening from charged spin-1 gluons. The value of the coupling in QCD can be represented by the  $\beta$  function, for QCD it can be shown that to lowest order  $\beta(g)$  is proportional to  $-(\frac{11}{2} - \frac{n}{3})$  where  $n$  is the number of quarks. For QCD, with 8 gluons and 3 colors, the anti-screening from the gluons overcomes the screening of the quarks and thus the theory is asymptotically free. Figure 1.1 shows experimental estimates of  $\alpha_S$  as a function of the scale of the momentum exchange. The experimental results are in agreement with the predictions of asymptotic freedom.

Within baryons and mesons quarks are bound in colorless states, as explained above, and at short distance scales the coupling between the quarks and gluons is weak and we can treat the interaction of quarks perturbatively. However, when we attempt to remove a quark from a hadron, lattice QCD calculations show the potential increases approximately linearly with distance. Eventually the energy put into this hypothetical system increases to a high enough point that a

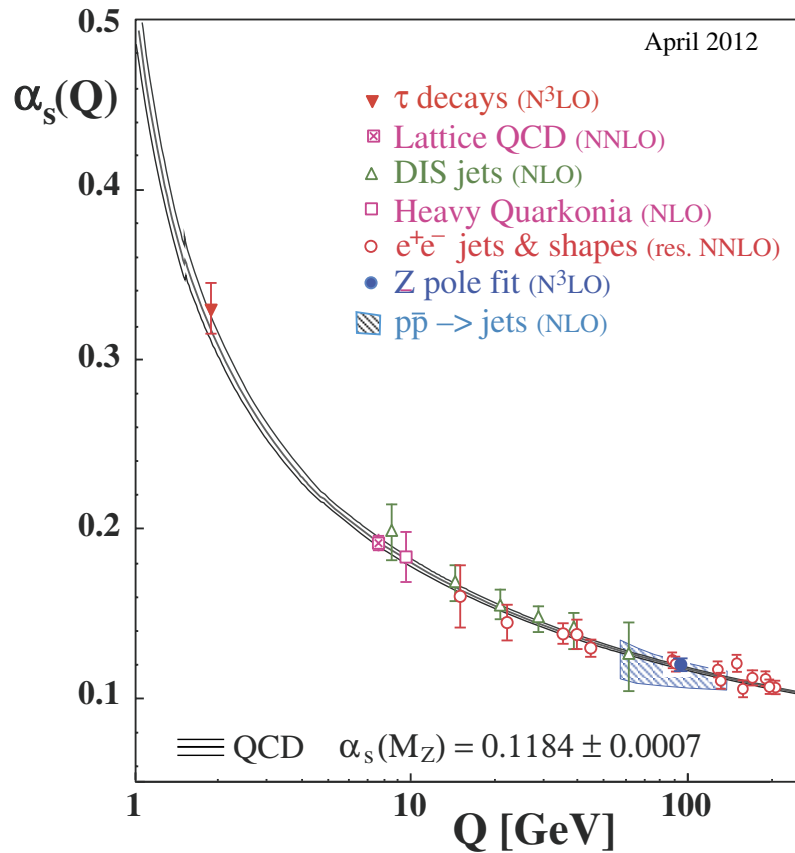


Figure 1.1: Several measurements of the strong coupling constant  $\alpha_S$  showing how it varies with energy scale. Decreasing coupling strength as the interaction energy goes up is consistent with predictions of asymptotic freedom

new quark anti-quark pair is created from the vacuum and we end up with two hadrons. This property of QCD, that quarks and gluons remain bound in colorless states, we refer to as confinement.

Confinement and asymptotic freedom are two of the most interesting properties associated with QCD, and are responsible for many of the interesting phenomena within the strong interaction. As we dive deeper into QCD we will next explore the QCD phase diagram, and look for evidence of confinement being broken.

## 1.2 QCD Phase Diagram and Deconfinement

At low temperatures lattice calculations show that quarks are confined within hadrons, we will now turn our attention to the properties of quark matter under more extreme conditions. Lattice calculations also predict a rich phase structure in QCD beyond just what we observe in low temperature hadronic matter. As we increase the temperature and density of nuclear matter it is predicted that quarks and gluons are deconfined from their hadronic states. We call this hot dense state of matter with strongly interacting free quarks and gluons the Quark Gluon Plasma (QGP). Conditions in the universe allowed for QGP to exist up until about  $10^{-5}$  s after the Big Bang. There is also the chance that colder deconfined matter could exist within neutron stars.

Figure 1.2 shows an illustration of the QCD phase diagram. Nuclear matter exists in the lower right part of the figure, inside nuclei the temperatures are low and the average net baryon number is high. The figure also shows the regions of the phase diagram which are accessible to various collider and fixed-target experiments which we will discuss further in upcoming sections. Also of note is that the phase transition from QGP to hadronic matter can be either a first order or second order phase transition and that there is postulated to be a critical point in the QCD phase diagram. The search for the QCD critical point is an area of active

research, but is beyond the scope of this dissertation.

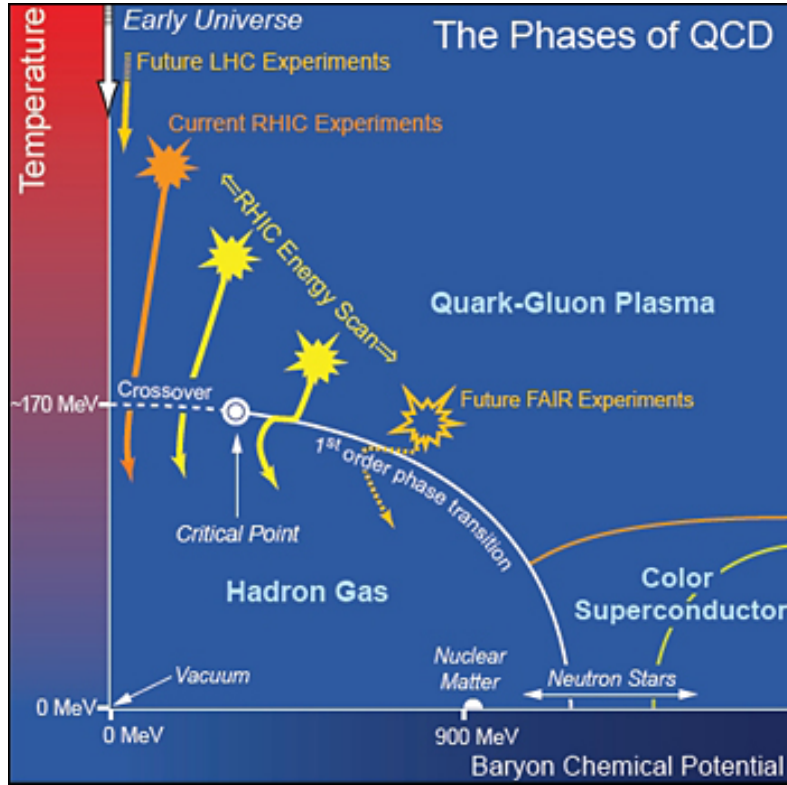


Figure 1.2: Illustration of the QCD phase diagram showing the various regimes as well as the reach of current experiments.

The critical behavior in QCD can be seen in the bulk thermodynamic properties of QGP around the critical temperature  $T_c$ . Figure 1.3 shows lattice QCD calculations of the quantity  $p/T^4$  as a function of temperature for various quark flavor combinations. At the critical temperature there is a transition from hadronic to partonic degrees of freedom which is seen in the large jump in  $p$ . At high temperatures the medium's behavior asymptotically approaches that of an ideal gas.

The increase in degrees of freedom is taken as evidence that the phase transition in QCD coincides with the onset of deconfinement and the switch from hadronic to partonic degrees of freedom.

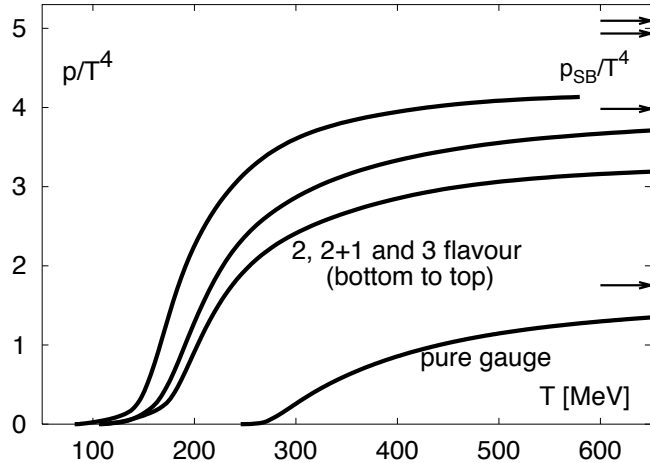


Figure 1.3: Calculations of  $p/T^4$  in QCD for various numbers of quark flavors. Large jump near  $T_c$  is the result of an increase in the number of degrees of freedom in the medium and is caused by the deconfinement of hadronic matter.

## 1.3 Experiments on QGP

### 1.3.1 Heavy Ion Collisions

With the prediction that deconfined matter could exist at sufficiently high temperatures and densities, there was significant interest in creating these conditions experimentally. The idea was to collide the nuclei of heavy elements at relativistic speeds, at high enough energy, these collisions could recreate the conditions in the universe shortly after the big bang and cause hadronic matter to become deconfined. The first experiments looking for QGP were fixed target programs at the Alternating Gradient Synchrotron at Brookhaven National Laboratory and the Super Proton Synchrotron at CERN. Initial hints towards deconfinement were

seen in these experiments. The WA97 and NA49 experiments observed large enhancement for strange baryons in Pb+Pb collisions which could be explained by a phase transition to a state with massless light quarks.

The early fixed target results pointed in the direction of QGP but were not conclusive proof of its existence. The next step for QGP research was to move to collider based experiments. In 2000 the Relativistic Heavy Ion Collider (RHIC) began operating with the capability to collide gold nuclei at 200 GeV center of mass energy per nucleon. Several years later the Large Hadron Collider (LHC) began colliding lead nuclei at over 2 TeV center of mass energy. Key measurements have been made by the experiments at RHIC pointing towards the existence of a strongly interacting deconfined phase of matter. We will now discuss some of these results which include: thermal production of light hadrons, elliptic flow of particles, and suppression of high  $p_T$  particles and jets in central collisions. We will then look in particular at the measurements made in the heavy flavor sector (charm and bottom quarks) and motivate future observations there.

### 1.3.2 Hadron Yields

To look for signs of the QCD phase transition and the QGP, we want to study central collisions of heavy ions. In heavy ion collisions the two nuclei are offset from each other by some impact parameter, and thus their region of overlap is an ellipsoid. We refer to the degree of overlap between the nuclei as the centrality and typically describe events by which percentile of centrality they fall into e.g. 10%-20% central (lower number corresponds to more central). The actual centrality definition is estimated based on models of the multiplicity observed in detector. The most central collisions have the largest and longest lived fireballs and thus create the most favorable conditions for producing QGP.

One measurement to perform in heavy ion collisions is to measure the yields

of hadrons from central collisions and compare them to thermal statistical models to extract the temperature and baryon chemical potential. Figure 1.4 shows the yields for several hadrons as measured by the experiments at RHIC along with the yields as determined by the fits to a thermal statistical model. From this the temperature at chemical freeze-out (the point in the collision at which particle flavors are fixed) can be measured and it is calculated to be 164 MeV.

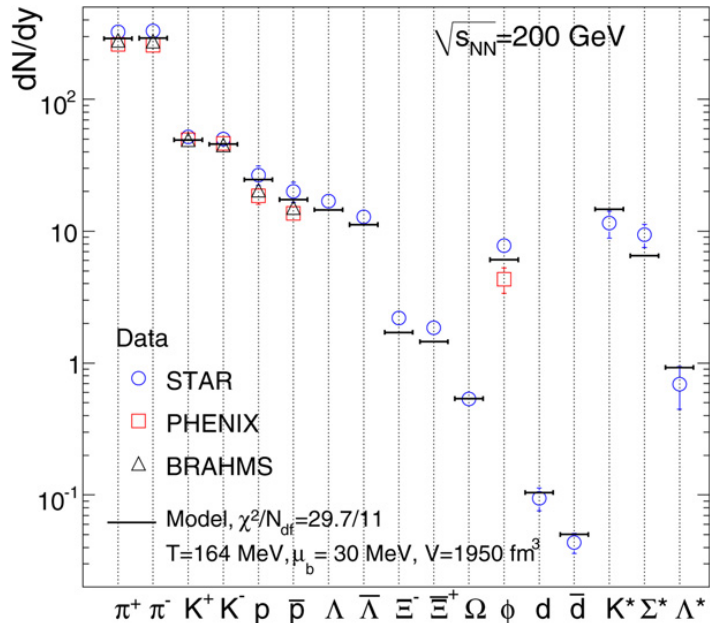


Figure 1.4: Yields for various hadrons in central collisions at RHIC energies compared to calculations from thermal statistical models.

Comparisons can be made across several experiments with different collision energies to look for evidence of a phase transition, this is shown in Figure 1.5. This shows the  $T$  and  $\mu_B$  extracted from the thermal statistical model fits as a function of the collision energy. The lower points come from the fixed target programs at the AGS and SPS while the highest data point corresponds to RHIC energies. The flattening of the temperature at chemical freeze-out around  $T \sim 160$  MeV as energy increases is suggestive of a QCD phase boundary.

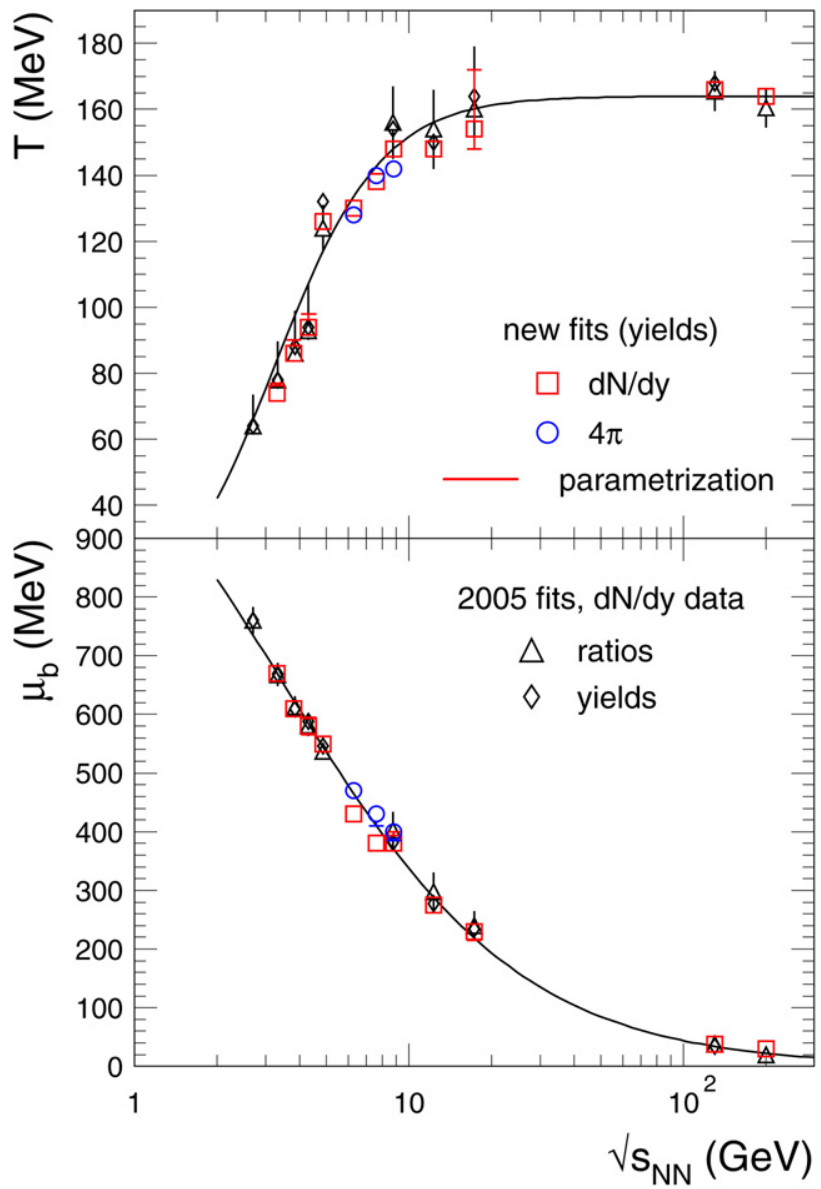


Figure 1.5: Temperature and baryon chemical potential extracted from thermal statistical model as a function of collision energy.

### 1.3.3 Elliptic Flow

In heavy ion collisions the nuclei do not exactly overlap, instead leaving an ellipsoidal region where temperatures and densities are high enough to create quark gluon plasma. This ellipsoidal overlap region creates an initial position space anisotropy which leaves a pressure gradient along the fireball which manifests itself as an momentum dependent azimuthal anisotropy in the final state, which we call elliptic flow. More formally, the distribution of particles as a function of azimuthal angle can be written out as a Fourier expansion:

$$E \frac{d^3N}{d^3p} = \frac{1}{2\pi} \frac{d^2N}{p_T dp_T dy} [1 + \sum_{n=1}^{\infty} 2v_n \cos(n(\phi - \Psi_r))] \quad (1.1)$$

Where  $\Psi_r$  is the angle of the reaction plane, which for our purposes can be thought of as the plane perpendicular to the major axis of the ellipsoid. The elliptic flow is the coefficient of the second term of this expansion,  $v_2$ . In Au+Au collisions at RHIC  $v_2$  is large for light hadrons and consistent with hydrodynamic models at low  $p_T$  ( $\leq 2$  GeV/c), at higher  $p_T$  the contribution of jets to  $v_2$  needs to be considered. These measurements of  $v_2$  point to a high degree of thermalization in collisions at RHIC energies and the mass dependence of  $v_2$  indicates a collective flow of the medium.

An interesting extension for  $v_2$  measurements is to look at how  $v_2$  scales with the number of constituent quarks. To measure this experimentally, measurements of  $v_2$  are performed for identified particles, then the results, scaled by the number of constituent quarks in the particle, are examined. Results for  $v_2$  in 200 GeV Au+Au collisions in STAR scaled by number of constituent quarks are shown in Figure 1.6. From the plots we can see that the scaled  $v_2$  in hadrons follows a universal trend for low  $p_T$ . This points to the main hadronization mechanism at low  $p_T$  to be coalescence of quarks and that in the collective evolution of the medium the partonic, rather than hadronic, degrees of freedom are most relevant.

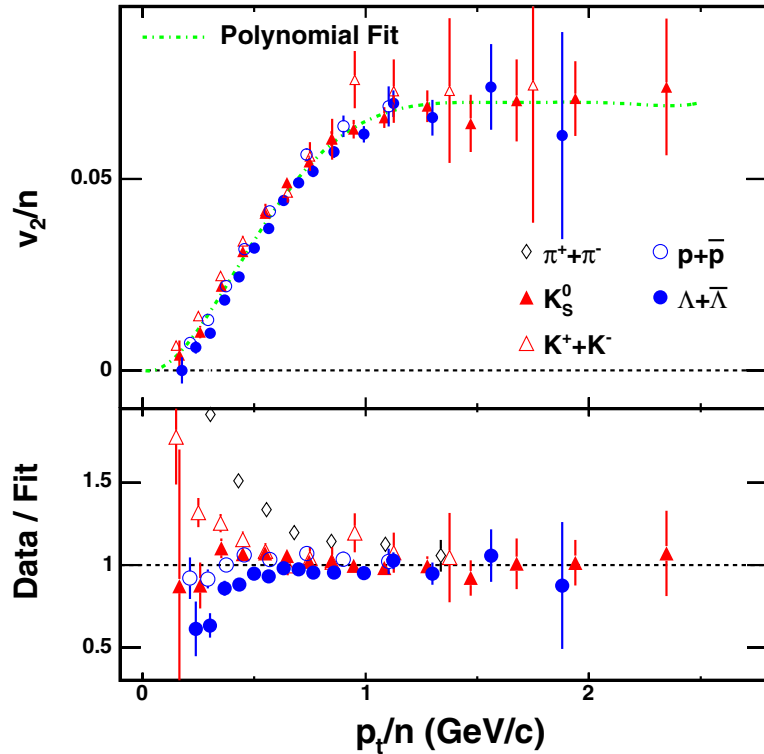


Figure 1.6: Identified particle  $v_2$  as measured in 200 GeV Au+Au minimum bias collisions in STAR scaled by the number of constituent quarks. Common trend across hadrons is evidence for hadronization from coalescence of thermalized quarks.

### 1.3.4 $R_{AA}$ and Jet Suppression

Another technique for studying QGP is to compare observables between heavy ion collisions and p+p data. In proton-proton or proton-nucleus collisions the baryon density is not high enough for a QCD phase transition. Here we will explore two different ways of comparing heavy ion and p+p systems. The first is the nuclear modification factor which compares particle yields in heavy ion systems to the scaled up yields from p+p, differences in these yields could be signs of further interactions with the medium. We will also look at jet modification. Jets are the product of hard scattering of quarks and gluons in the initial collision, as a hard quarks traverses the QGP it will be subjected to strong interactions with the medium and lose energy. The suppression of high  $p_T$  jets is further evidence for the existence of QGP.

In collider experiments, high  $p_T$  particles are generated from the initial hard scattering of partons in the collisions. Without any sort of medium effects from QGP we could model the collision of two heavy nuclei as a superposition of binary proton collisions. Deviation from this behavior indicates extra effects from the medium. We can also investigate and control for the effects of cold nuclear matter by studying modification of yields in d+Au collisions. We define the ratio of yields in heavy ion to scaled p+p as the nuclear modification factor  $R_{AA}$ . Which is explicitly defined as:

$$R_{AA}(p_T) = \frac{(1/N_{AA})d^2N_{AA}/dp_Tdy}{\langle N_{coll} \rangle / \sigma_{pp}^{inel}(d^2\sigma_{pp}/dp_Tdy)} \quad (1.2)$$

where  $\langle N_{coll} \rangle$  is the average number of collisions as calculated by a Glauber model simulation. Figure 1.7 shows the measurement of  $\pi^0 R_{AA}$  in Au+Au collisions in PHENIX. In central collisions, where we expect critical behavior and deconfinement, the yield is highly suppressed for all momenta. In the peripheral bin where no QGP is expected to be formed the  $R_{AA}$  is consistent with 1, mean-

ing the yields are what would be expected from a superposition of p+p collisions. Moving from most central to most peripheral bins, the yields gradually go from highly suppressed to not suppressed at all, as we would expect since the more central bins produce regions of higher temperature and density bringing on the onset of deconfinement.

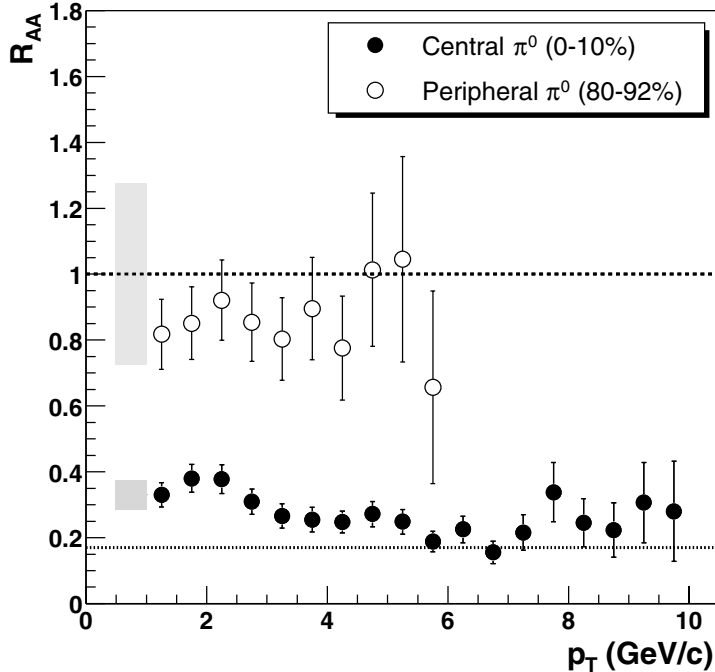


Figure 1.7: PHENIX measurement of  $R_{AA}$  for  $\pi^0$  in central and peripheral Au+Au collisions. Large suppression of yields is seen in central collisions.

The properties of the QGP can also be probed by examining the effects on high  $p_T$  partons as they traverse the medium. The high  $p_T$  light quarks are created by hard processes early in the collision and are theorized to lose energy due to induced gluon radiation in the QGP. The energy loss leaves softer particles in jets and the broadening of spatial jet-like correlations. STAR investigated light flavor jet correlations by looking at azimuthal correlations of particles in Au+Au, p+p, and d+Au collisions. High  $p_T$  particles were used as the leading particles and correlated with other hadrons in the event.

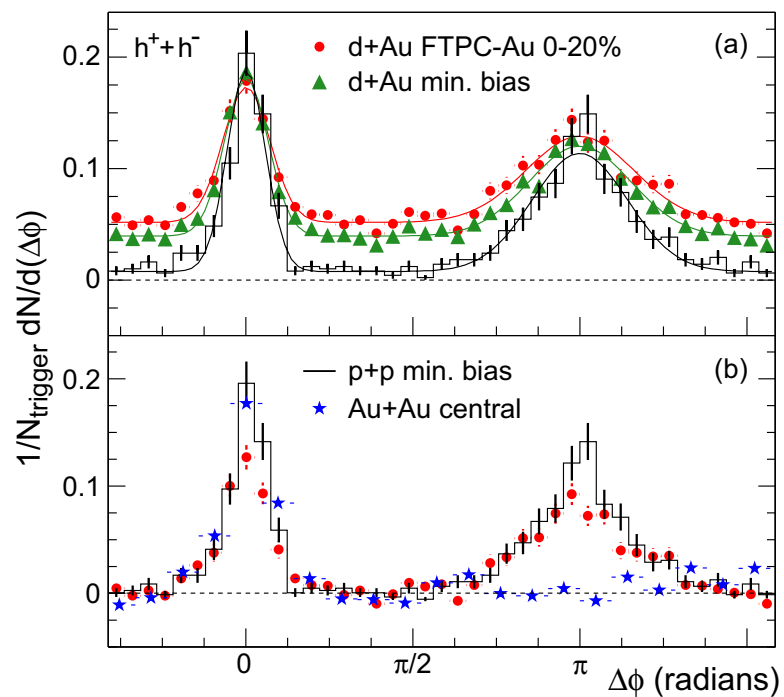


Figure 1.8: Azimuthal dihadron correlations in STAR. Strong quenching of the away side jet is seen in Au+Au collisions but not p+p or d+Au. Lack of suppression in d+Au rules out cold nuclear matter effects on jet suppression.

Figure 1.8 shows the azimuthal dihadron correlations measured in STAR. In p+p and d+Au we see strong back-to-back correlations of particles due to momentum conservation in the initial production of hard partons. The consistency of p+p and d+Au correlations is evidence that cold nuclear matter does not significantly impact the propagation of hard quarks, but the slight broadening and enhanced yields are consistent with expectations from pQCD models with the Cronin effect. However, in Au+Au the away side jet is strongly suppressed, indicating that light quarks lose a substantial amount of energy within the hot and dense medium created in heavy ion collisions leading to reduced yields of high  $p_T$  associated particles in central Au+Au events.

## 1.4 Heavy Flavor Probes

### 1.4.1 Motivation

The observables discussed so far have been largely concerned with phenomena involving the light quarks ( $u$  and  $d$ ) which have different sensitivity to the evolution of the QGP than heavy quarks. Thermal production and coalescence of light quarks into hadrons as well as collectivity of light quarks are evidence for a hot dense strongly interacting phase of matter being produced in heavy ion collisions. Heavy quarks can also be used to probe the QGP and help illuminate additional properties of the medium that are harder to explore with light flavor observables.

Heavy flavor quarks, by which we mean charm ( $c$ ) and bottom ( $b$ ) quarks, are an important additional avenue of study in heavy ion physics for a few reasons. The light quarks have masses  $\sim 2 - 6 \text{ MeV}/c^2$  while the heavy flavor quarks have masses  $\sim 1.3 \text{ GeV}/c^2$  for charm and  $\sim 4.3 \text{ GeV}/c^2$  for bottom. Unlike the light quarks the masses of the heavy quarks are well above the temperatures found in the medium produced by relativistic heavy ion collisions. This means that thermal production, which often complicates light flavor analyses, does not need to be

considered for heavy flavor. Instead heavy flavor is exclusively produced by hard processes in the very early stages of the collision. Thus heavy quark observables will be sensitive the entire evolution of the medium. Also the energy scale for heavy quark production is high enough ( $M_{c,b} \gg \Lambda_{QCD}$ ) that the production can be accurately described with pQCD.

The energy loss of heavy quarks in QGP is also an area of significant interest. Earlier we discussed jet quenching as a result of light flavor quarks losing energy in a strongly interacting medium. The mechanism behind light quark energy loss in the QGP is theorized to be induced gluon radiation, and when calculating the radiative energy loss it can be assumed the light quarks are massless. In the propagation of heavy flavor quarks this assumption cannot be made. Instead for heavy quarks the radiative energy loss differs from the massless case by a factor:

$$\left(1 + \frac{\theta_0^2}{\theta^2}\right)^{-2} \quad (1.3)$$

where  $\theta_0 = \frac{m}{E}$ . This means that relative to light flavor, the gluon radiation from heavy flavor quarks is suppressed at small angles  $\theta$ . This phenomenon is known as the ‘dead cone effect’. Instead, in the heavy flavor sector, it’s possible that collisional losses from elastic scattering in the medium plays a much more significant role.

#### 1.4.2 Experimental Results

While heavy flavor observables are of considerable interest in the study of QGP they come with some serious complications compared to the light flavor observables. Production rates for charm and bottom are lower and thus many heavy flavor measurements are limited by statistics. Only in the last several years has RHIC produced high statistics Au+Au data sets opening up studies in heavy flavor. Another problem is that the heavy quarks hadronize into  $D$  and  $B$  mesons

which are short lived and it is difficult to reconstruct these decays with high efficiency, especially in heavy ion collisions. Since 2014 STAR has installed the Heavy Flavor Tracker to improve secondary vertex resolution and allow better reconstruction of heavy flavor decays. An alternative to direct reconstruction of  $D$  or  $B$  is to look only at the electrons produced from semi-leptonic decays these mesons. At high  $p_T$  ( $> 2 \text{ GeV}/c$ ) the direction of a decay daughter electron is well correlated with the parent meson, these electrons can then be used as a proxy for the  $D$  or  $B$  meson. The branching ratios for semi-leptonic decays of heavy flavor mesons is on the order of 10% which further limits the possible statistics.

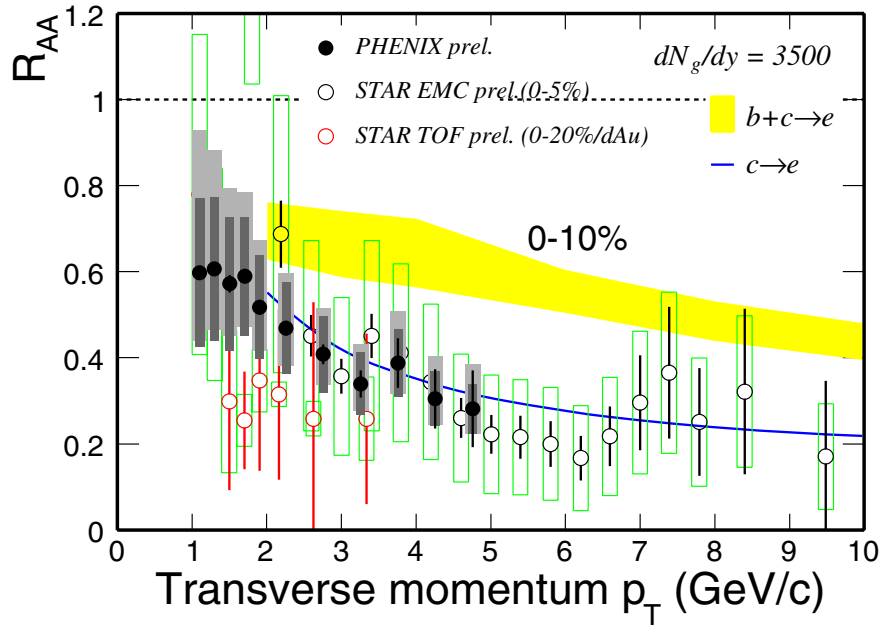


Figure 1.9: Non-photonic electron  $R_{AA}$  from central Au+Au collisions measured by STAR and PHENIX. The theoretical curves show expected suppression due to radiative energy loss. The measured  $R_{AA}$  is consistent with measurements of light flavor  $R_{AA}$ .

Like in light flavor we can measure the  $R_{AA}$  for heavy flavor to look for effects of the medium relative to p+p systems. If we considered that the induced gluon

radiation from heavy quarks is suppressed at low angles, then we might expect to see a higher  $R_{AA}$  (less suppression of yield relative to superposition of binary collisions) in heavy flavor. STAR and PHENIX have measured  $R_{AA}$  for electrons from semi-leptonic  $D$  and  $B$  decays. The results are summarized in Figure 1.9. Both experiments see values of  $R_{AA}$  around .2 – .3 at high  $p_T$  which is consistent with the suppression of yields observed in light flavor hadrons.

The theoretical curves show the predictions of suppression due to radiative energy loss for decays from  $c$  as well as  $c$  and  $b$  combined. It is difficult to explain the large suppression for heavy flavor quarks if it is solely due to gluon radiation. Models which include collisional energy loss for heavy quarks as well predict a larger suppression.

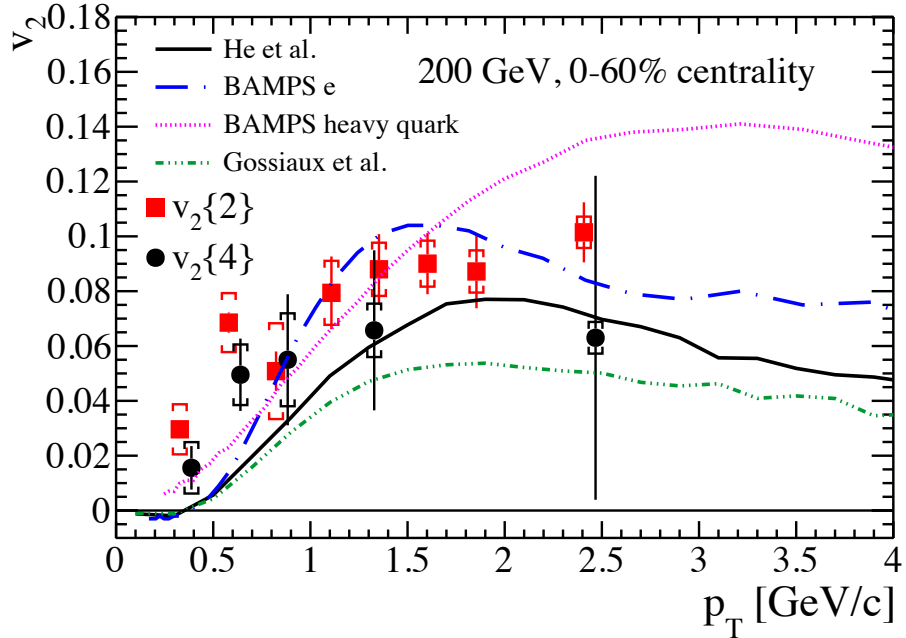


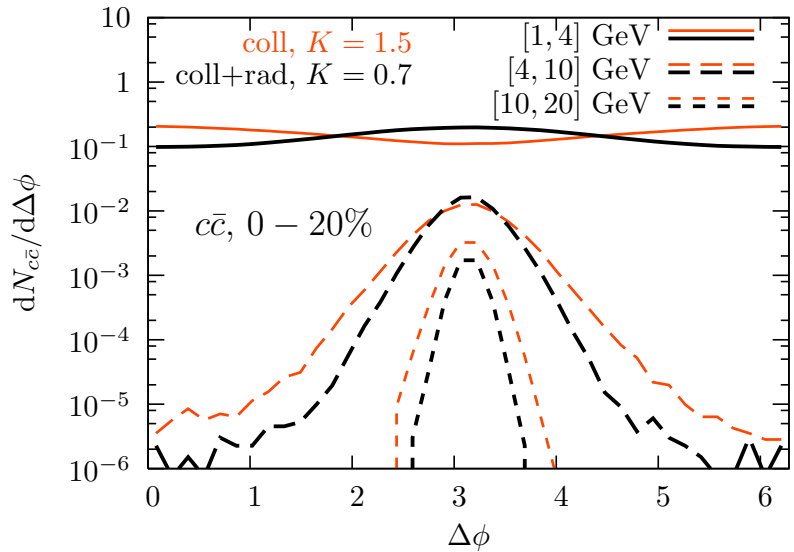
Figure 1.10: Elliptic flow of electrons from heavy flavor decays measured in STAR as well as predictions of  $v_2$  relative to the reaction plane for various models.

Likewise elliptic flow in heavy flavor is also an avenue of active study. The low  $p_T$   $v_2$  can be used to study how thermalized  $c$  and  $b$  quarks are in the medium.

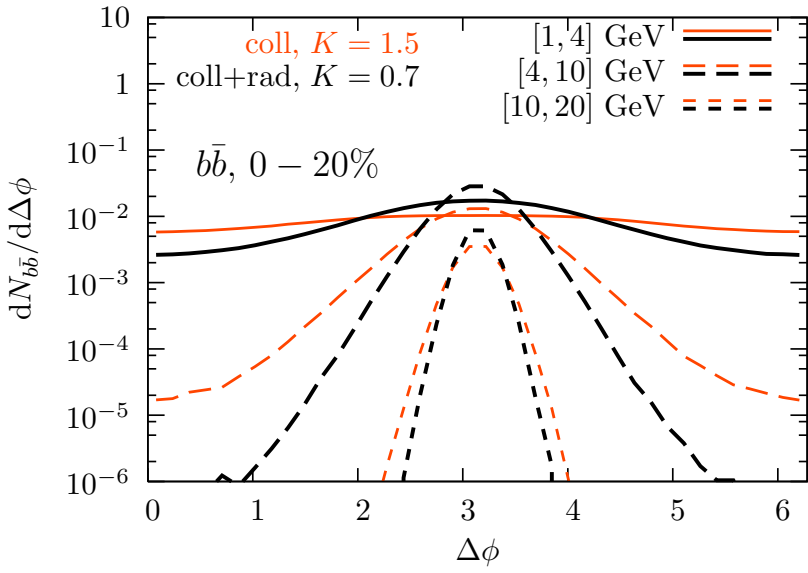
Preliminary STAR measurements of  $v_2$  for heavy flavor decay electrons are shown in Figure 1.10, also included are theoretical predictions for various energy loss models for heavy quarks. The electron  $v_2$  measurement is complicated by contributions from nonflow effects. A heavy quark traversing the medium will see different path lengths if it is in-plane versus out-of-plane. Path length dependence of jet modification for heavy flavor quarks could then contribute to  $v_2$  separately from thermalization and collectivity. Non-flow effects are expected to be more prominent at high  $p_T$

## 1.5 Heavy Flavor Two Particle Correlations

While most analyses in the heavy flavor sector have focused on spectra,  $R_{AA}$ , and flow measurements, two particle correlations are also an important tool for studying the dynamics of heavy quarks. Two particle azimuthal correlations in light flavor were the tool for jet suppression measurements which were shown previously (Figure 1.8) and we hope to extend these measurements to the heavy flavor sector. The correlations rely on the fact that hard processes in the collisions of partons result in back-to-back pairs of dijets due to conservation of momentum. The modification of the resulting back-to-back correlations in the presence of QGP can be used to explore the properties of quarks traversing the medium. Figure 1.11 shows a theoretical calculation of the back-to-back correlations of heavy quarks produced in Pb+Pb collisions at LHC energies. We can see a few of the general modifications to the correlation that may arise from interactions with the medium. There is a difference depending on the energy loss model used, either purely collisional or collisional plus radiative. We also see that higher momentum pairs retain their initial back-to-back correlation more. It has even been suggested that for low momentum pairs the correlation may be enhanced on the near side due to the “partonic wind”.



(a)



(b)

Figure 1.11: Theoretical calculations of azimuthal correlations for heavy quarks in Pb+Pb collisions at LHC energies. Differences in the models for energy loss can be seen as well as the dependence on  $p_T$ .

In central dihadron collisions the two particle correlations showed a double peaked structure on the away side, this was possibly thought to be Mach cones, shockwaves in the QGP produced by the quarks, but it is more likely to be a correlation from triangular flow  $v_3$ . The energy loss of a quark passing through deconfined matter and losing energy due to induced gluon radiation is proportional to the product  $\hat{q}L^2$ . Here  $\hat{q}$  is the transport coefficient, defined as the mean momentum spread per unit length traversed and from previous measurements is thought to be on the order of  $10 \text{ GeV}^2/\text{fm}$ . Two particle correlations can be used to explore the path length dependence of energy loss as the near side trigger jet may traverse through a shorter path in the QGP than the away side jet. However care must be taken as there is potentially bias towards emissions from the surface of the medium when looking at triggered two particle correlations.

Heavy flavor two particle correlations look at the path length dependence of energy loss for heavy quarks and the relative contribution of radiative and collisional energy loss mechanisms. Ideally we would like to study the energy loss of the heavy quarks or the heavy flavor mesons directly, however this is not within the capabilities of current experiments. Instead we will need to rely on the electrons from semileptonic decays of  $B$  and  $D$  mesons. Figure 1.12 shows a cartoon of how two particle correlations can investigate the dynamics of heavy quarks in QGP. A sufficiently high  $p_T$  electron is used as the trigger particle in the correlation. The near side and away side of the correlation contain information on the decay products from the heavy mesons. We are also interested in the response of the medium to the quarks.

One of the largest challenges in constructing two particle correlations is limited statistics. STAR has previously looked at heavy flavor electron-hadron correlations to study the charm to bottom fraction produced in p+p collision. PHENIX has also measured correlations of electrons from heavy flavor decays (Figure 1.13) in both p+p and Au+Au. In 2010 and 2011 RHIC completed high statistics

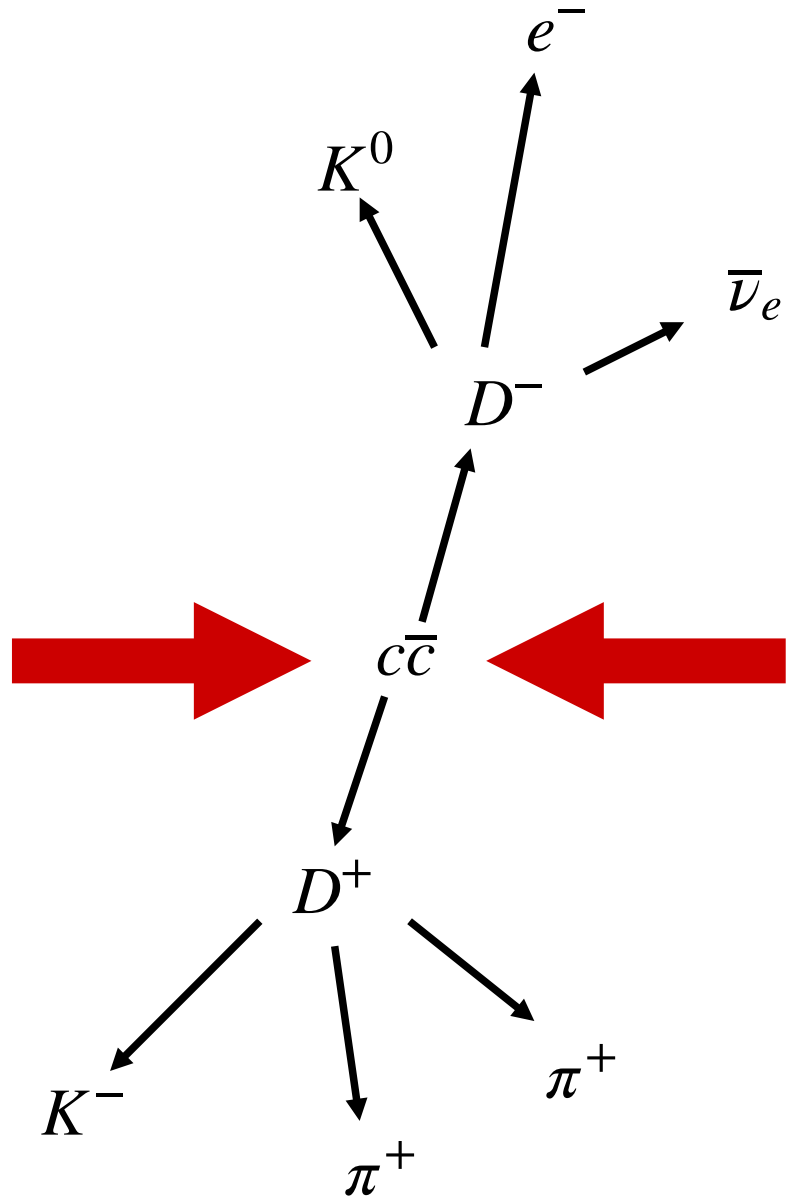


Figure 1.12: Illustration of two particle correlation coming from a produced  $c\bar{c}$  pair. This diagram only shows the particles from the decays of heavy mesons but we are also interested in the effect of the heavy quarks on the medium as well.

Au+Au runs opening up the possibility of much improved measurements of heavy flavor two particle correlations. This dissertation will focus on constructing two particle correlations between electrons from heavy flavor decays (here called *non-photonic electrons*) and hadrons. The chapters will cover the experimental apparatus, the procedure for identifying electrons, and then making correlations themselves as well as calculating backgrounds.

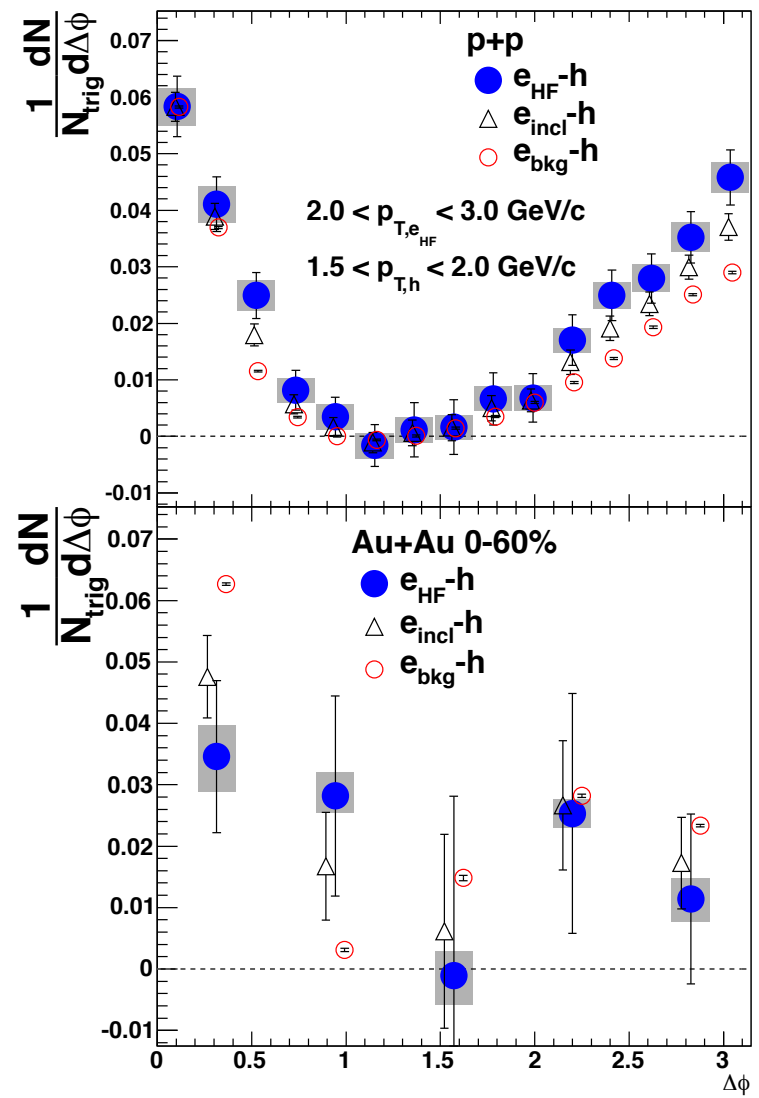


Figure 1.13: Azimuthal correlation of electrons from heavy flavor decays to hadrons in p+p and Au+Au as measured by PHENIX.

# CHAPTER 2

## Experimental Setup

We will discuss the accelerator setup used to collide gold nuclei at relativistic energies which briefly create the strongly interacting medium of quarks and gluons which we wish to study. We also examine the STAR detector, triggering, data acquisition, and its particle identification capabilities. We will specifically talk about the detector subsystems which are most relevant to the identification of electrons from heavy flavor processes.

### 2.1 Relativistic Heavy Ion Collider

The Relativistic Heavy Ion Collider (RHIC) is an accelerator facility located at Brookhaven National Lab which was built for the study of QCD. The collider is capable of colliding a variety of heavy nuclei (to date: gold, uranium, and copper) as well as lighter particles (protons, deuterons, and recently helium-3). RHIC is also capable of colliding polarized proton beams for the program studying the spin structure of the proton. The top energy for collisions in RHIC is 500 GeV for p+p and 200 GeV for Au+Au.

The main collider rings at RHIC are 2.4 miles in circumference and intersect at six interaction points. Particles are brought up to collision energies through a series of linear accelerators and booster synchrotrons. Figure 2.1 shows the layout of the RHIC facilities as well as the location of some experiments that have run or are currently running at RHIC. PHENIX and STAR are the two long

running general purpose detectors at RHIC.

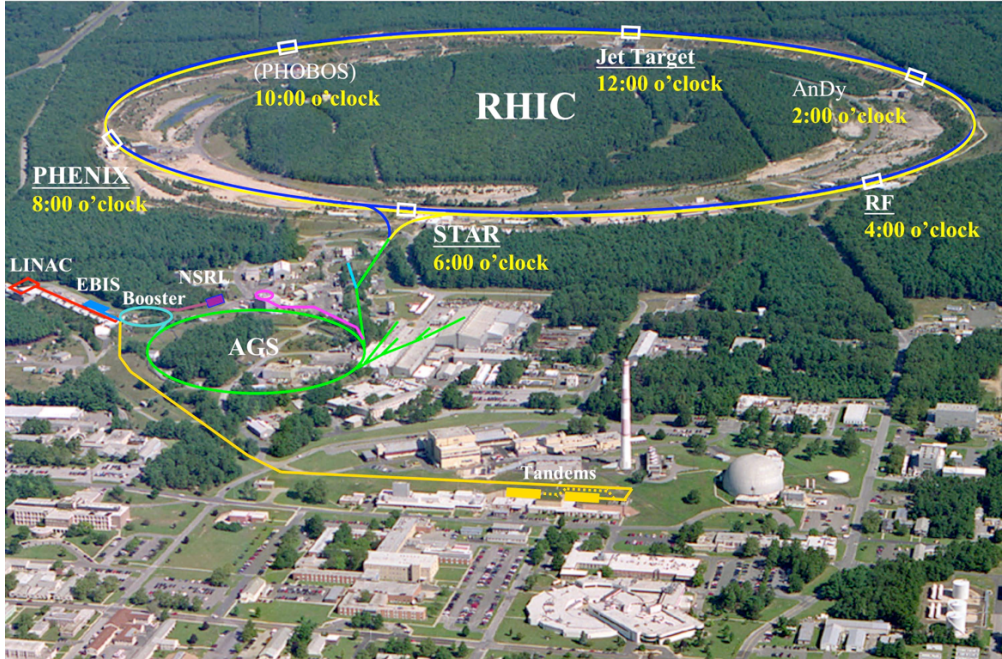


Figure 2.1: RHIC Complex seen from above. Top of the picture shows the main rings and locations of various experiments. Lower part shows the LINAC and booster rings.

For the run in 2011 gold nuclei were generated from an ion source and then initially accelerated in the Tandem Van de Graaff line. RHIC had multiple Van de Graaff accelerators allowing for collisions between mixed nuclei (for example, Au+Cu or d+Au). From 2012 onwards, the function of the tandems was replaced by the Electron Ion Beam Source (EBIS) which generates particles from deuterons to uranium nuclei. Protons beams on the other hand originate from the 200 MeV LINAC. Both protons and other nuclei move to the booster synchrotron which further accelerates the particles using RF waves. After passing through the booster ring the beams then enter the Alternating Gradient Synchrotron (AGS). The AGS was a long running and highly successful facility at BNL, three Nobel Prizes resulted from research conducted at AGS. Now AGS serves as a final booster

ring before sending the beams to the main RHIC rings.

The beams then reach RHIC where the last remaining electrons are stripped away leaving only the nuclei. In the storage rings the particles circulate in bunches, typically around 110 bunches per ring, and the beams are brought to their collision energy. The beams can collide at six interaction points along the ring. Top energy for the heavy ion program is 200 GeV per nucleon, higher energies are used in some p+p collisions and RHIC is also capable of colliding at lower energies as is the case in the beam energy scan program which explores the QCD phase diagram.

## 2.2 STAR Detector

The Solenoidal Tracker at RHIC (STAR) is a general purpose detector located at the 6 o'clock interaction point at RHIC. STAR consists of a variety of detector subsystems which cover a large acceptance region and allow for a variety of physics programs. This analysis will focus only on data taken with STAR's mid rapidity detectors. Figure 2.2 is a diagram showing the configuration of STAR. It should be noted that for the data taking for this analysis the Silicon Vertex Tracker (SVT) was removed and only its support structure remained.

In STAR the primary tracking detector is the Time Projection Chamber (TPC) which surrounds the beam pipe, covering  $2\pi$  in azimuth and capable of tracking particles in pseudorapidity up to around  $\eta \approx 1.3$ . The TPC is also measures ionization energy loss of charged particles, which is used for particle identification. For runs 10 and 11 the TPC was the inner most tracking detector in STAR. Prior to this the SVT was in place as a tracking detector and from 2014 onwards the inner tracking in STAR has been upgraded with the Heavy Flavor Tracker (HFT) which is capable of improving resolution on secondary vertices. Outside of the TPC is the Time of Flight (TOF) detector. TOF greatly improves the particle identification for low momentum hadrons. Further outside of TOF and the TPC

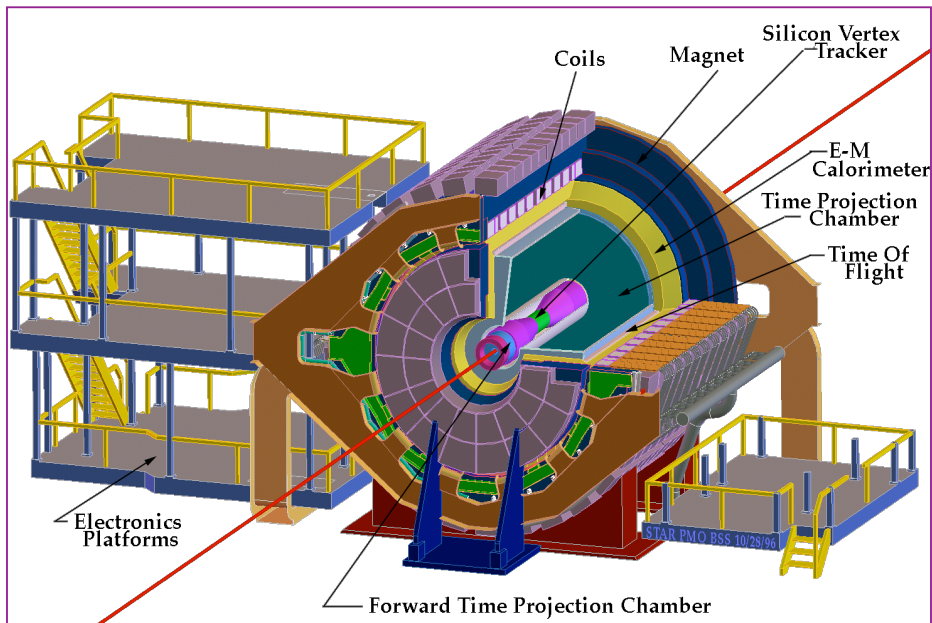


Figure 2.2: The STAR detector as it was configured around the time of the data taking for this analysis. The SVT was removed prior to run 10 and thus only its support structure was in during the runs.

is the Barrel Electromagnetic Calorimeter (BEMC): a lead-scintillator calorimeter and Shower Maximum Detector (SMD). The BEMC allows for measurements of electron energies, improves the identification of high  $p_T$  electrons, and allows for identifying  $\gamma$ 's which cannot be tracked in the TPC. Sitting outside the BEMC is the Muon Telescope Detector (MTD) which is used for the analysis of dimuon and  $e - \mu$  spectra. For measurements of non-photonic electrons we use the tracking and PID from the TPC as well as additionaly PID information from the BEMC systems.

## 2.3 Time Projection Chamber

The TPC is the main tracking and particle identification in STAR, it surrounds the beam pipe and interaction region and has full azimuthal coverage and covers  $\pm 1.8$  in pseudorapidity. The TPC is a cylindrical volume, 4.2 m long, with an inner diameter of 1 m and an outer diameter of 4 m. The enclosed volume is filled with a mixture of 10% methane and 90% argon. The TPC sits inside of the STAR solenoid magnet which is capable of producing magnetic fields of .5 T in two opposite polarities. Bending of tracks of charged particles in the TPC allows for tracking of particles from .1 GeV/c to 30 GeV/c. Midway down the length of the TPC the chamber is divided by the Central Membrane. A potential is established between the Central Membrane, the cathode, and the end caps of the TPC, the anodes. Inner and Outer Field Cages run the length of the TPC along the walls, gradually increasing in potential as they get closer to the Central Membrane. The field cages help establish a uniform electric field in the TPC which is critical for tracking resolution. Figure 2.3 shows an illustration of the TPC and the locations of the Central Membrane and field cages.

Charged particles traverse the TPC and ionize the gas inside. The electrons in the drift along the electric field in the TPC at  $5.45 \text{ cm}/\mu\text{s}$  towards the ends of

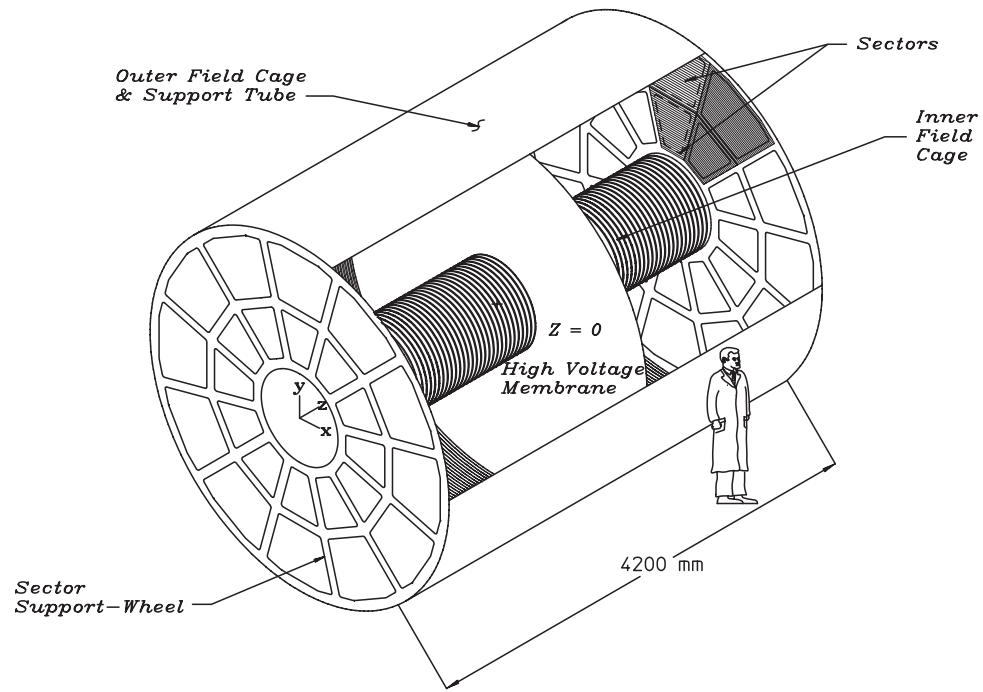


Figure 2.3: Diagram of the STAR TPC showing the main components as well as the scale.

the TPC where the readout pads are located. The endcaps of the TPC chambers are divided radially into 12 sections, each section has an inner and outer segment (Figure 2.4). The TPC readout sectors have 4 components, a pad plane and three wire planes. The outermost wire plane is a gating grid which can block charged particles in the TPC from reaching the readout counters at the endcap. Inside the gating grid are the ground wire plane, a readout plane and the the pad plane. The inner part of the TPC sector consists of 13 pad rows which are spaced 52 mm apart in the radial direction in the outer section there is no spacing between the pads. The inner sector also features smaller pads to improve tracking, particularly for low momentum tracks. Future upgrades to the TPC will replace the TPC sectors with ones that have no gaps between the inner pad rows. This will improve the tracking of the TPC out to larger  $\eta$ .

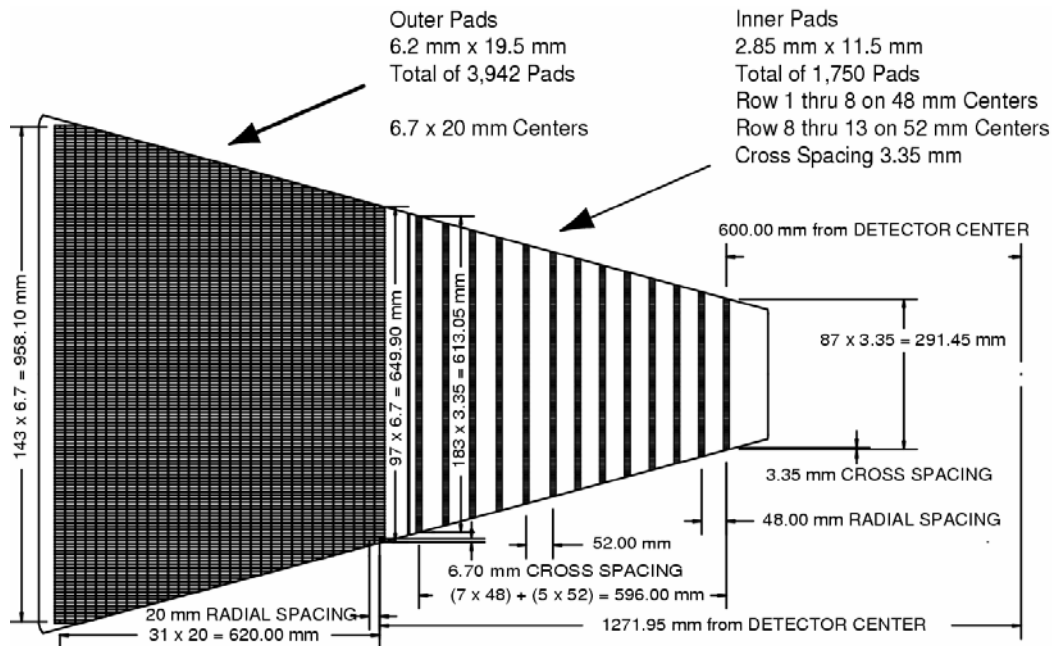


Figure 2.4: Schematic of one TPC pad plane. The difference in spacing between inner and outer pads can be seen.

## 2.4 Barrel Electromagnetic Calorimeter

The Barrel Electromagnetic Calorimeter (BEMC) is a lead-scintillator sampling calorimeter sitting outside of the TPC, the tower assemblies are within the coil of the main STAR magnet but the readout PMTs are located outside. The BEMC is used for studying high  $p_T$  processes such as jets, direct  $\gamma$ 's, and (in the case of this analysis) decays from heavy mesons. The calorimeter, being one of the fastest systems in STAR, is also used in triggering on high  $p_T$  particles. There are two main subsystems of the BEMC: the towers of lead and scintillator, which produce the particle showers and collect the light to measure the energy, and the Shower Maximum Detector (SMD) for measuring the profile of showers in the BEMC which can be used to select showers from electrons.

### 2.4.1 EMC Towers

The towers of the BEMC cover  $2\pi$  in azimuth and have coverage from -1 to 1 in  $\eta$ . The inner surface of the calorimeter sits approximately 2.2 m from the beam line in STAR. The towers are grouped into modules which each cover  $6^\circ$  in  $\phi$  and 1 in  $\Delta\eta$ . There are in total 120 modules, 60 on each half (lengthwise) of the detector. Each tower consists of alternating layers of lead and scintillator. There are 21 scintillating layers and 20 lead layers in each tower, the tower depth is approximately 20 radiation lengths. The towers have a projective geometry so that towers located out farther from  $\eta = 0$  still point back to the center of the interaction region in STAR. Figure 2.5a shows the structure and dimensions of a single tower from near the center of the BEMC ( $\eta \approx 0$ ). In Figure 2.5b is a photograph of a single BEMC module. The left end is near  $\eta = 0$  and the projective geometry of the towers can be seen when moving right along the modules.

Particle showers in the BEMC towers produce light in the scintillating layers

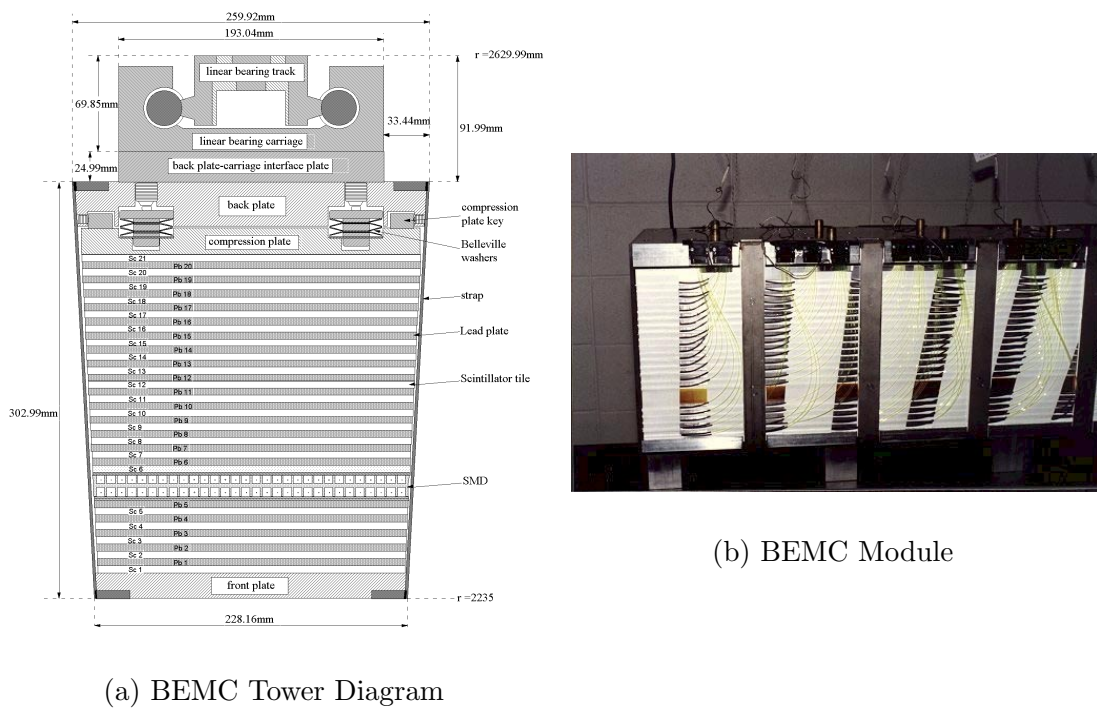


Figure 2.5: Left figure is a diagram of one BEMC tower as seen from the side. The location of the SMD is indicated after the fifth lead layer. Right shows a photograph of a single BEMC module showing the projective geometry of the towers.

which is then collected and read out by a wavelength shifting fiber. The fibers run from each scintillating layer of the tower to a photomultiplier tube (one per tower) located outside the STAR magnet.

#### 2.4.2 Shower Maximum Detector

The Shower Maximum Detector (SMD) is located within the BEMC towers and gives access to finer positional resolution than the BEMC towers alone, allowing us to study the profile and development of showers inside the BEMC. As can be seen in Figure 2.5a the BSMD sits after the fifth lead layer in the tower, which corresponds to  $\approx 5.6X_0$  of material total in STAR in front of the SMD. The SMD itself is a wire proportional counter with strip readout, there are two perpendicular directions for the chambers to measure shower profiles in both  $\eta$  and  $\phi$ . The strips are  $\approx 1.5$  cm in both directions for  $|\eta| < .5$  and 1.88 cm in the  $\eta$  direction outside of that. For electrons with  $p_T > 1$  GeV/c the SMD is near the depth of widest shower development (the Moliere radius for lead is  $\approx 3.2$  cm), however for hadrons the depth of maximum deveopment is around 1 nuclear interaction length, which for the BEMC close to the entire length of one BEMC tower. Thus we can use the development of showers in the SMD as a powerful tool for rejecting showers from hadrons or minimum ionizing particles. Figure 2.6 shows how the SMD works in practice, an electron enters the detector, develops into a wide shower and registers multiple hits in the SMD strips in both directions. The SMD, in addition to profiling showers, also gives much better position resolution for showers within the BEMC. At the front plane of the SMD the position resolution is  $\sigma = 2.4 \text{ mm} + 5.6 \text{ mm}/\sqrt{E}$  GeV. Tracks from the TPC point to the SMD with millimeter precision and thus we can use close spatial matching of tracks in the BEMC to TPC tracks to further improve electron identification.

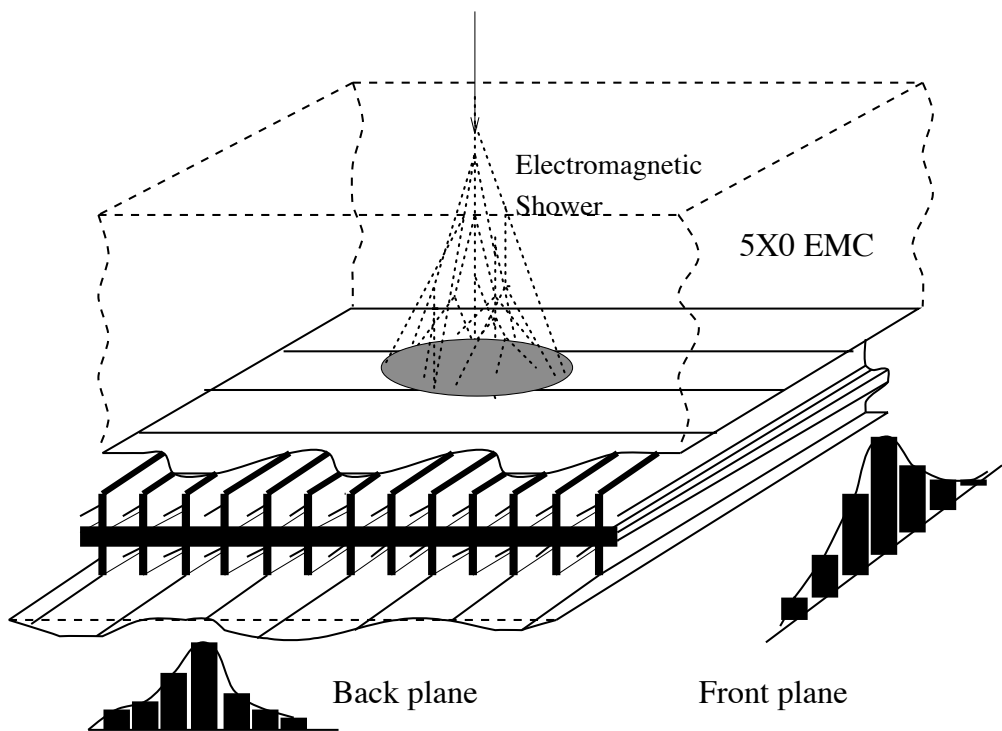


Figure 2.6: Illustration of the function of the BSMD detector. Particle enters the tower (at top) and develops into a shower which registers hits in the  $\eta$  and  $\phi$  directions in the BSMD.

# CHAPTER 3

## Identification of Non-photonic Electrons

We discuss the procedure for identifying electrons in events at STAR and how we remove photonic background. We show the event and track selection criteria and then lastly we will analyze the efficiency for identifying background photonic electrons. The identification of non-photonic electrons (NPE) and efficiency thereof will be critical factors when we construct the NPE-hadron correlations in later chapters.

### 3.1 Outline of the NPE Identification

This chapter will lay out the general methods for event selection, track selection, electron identification, and the removal of photonic electron background for both Au+Au and p+p collisions.

We start by identifying the dataset and the trigger collections we will use for the analysis. We look at the events and check that the quality of the event is good and that there could be candidate tracks for NPE in the event. We then reconstruct all tracks in the TPC and apply track quality cuts. To identify electrons we rely on the energy loss ( $dE/dx$ ) measured in the TPC and on the hits in the EMC towers and shower max detector.

The background from photonic electrons will be removed by searching for the opposite signed partner electron. If the primary track is from Dalitz decays or photon conversion in the detector, the partner and primary track should have a

low invariant mass. We will also investigate, through simulations, the efficiency for determining the background from photonic electrons.

In the end we will have a sample of electrons which we can use as triggers for measuring NPE-hadron correlations.

## 3.2 Dataset and Event Selection

### 3.2.1 Data and Triggers

In 2011 RHIC collided gold nuclei at  $\sqrt{s_{NN}} = 200$  GeV and delivered  $9.79\text{ nb}^{-1}$  integrated luminosity similar to what was delivered during the previous year's run (Figure 3.1a). The STAR detector recorded about 1.1 billion events across all triggers with TPC and BEMC information. In 2012 polarized proton collisions were run in RHIC (the polarization of the beams is not relevant to this analysis) at the same 200 GeV beam energy. RHIC delivered  $74.0\text{ pb}^{-1}$  (Figure 3.1b) which resulted in 1.7 billion triggered events in STAR. Heavy flavor events are rare and detector efficiencies can be low meaning the NPE analysis typically constrained by statistics, necessitating large data sets. The Silicon Vertex Tracker (SVT) was removed from STAR resulting in less material near the beam line which cuts down on background from conversions in the detector. This combination of low material and high statistics make runs 11 and 12 (prior to run 14) the best datasets available for the analysis of non-photonic electrons.

The STAR data acquisition system handles several different triggers the most commonly used is the minimum bias trigger (minbias) which fires based on the coincidence of the STAR vertex position detector(VPD) and Zero Degree Calorimeters (ZDC) these events are prescaled so that only a fixed fraction of triggers are accepted so that the DAQ's data taking rate is not exceeded. STAR can also trigger on hits in the barrel EMC, these are the high tower (HT) triggers. A high

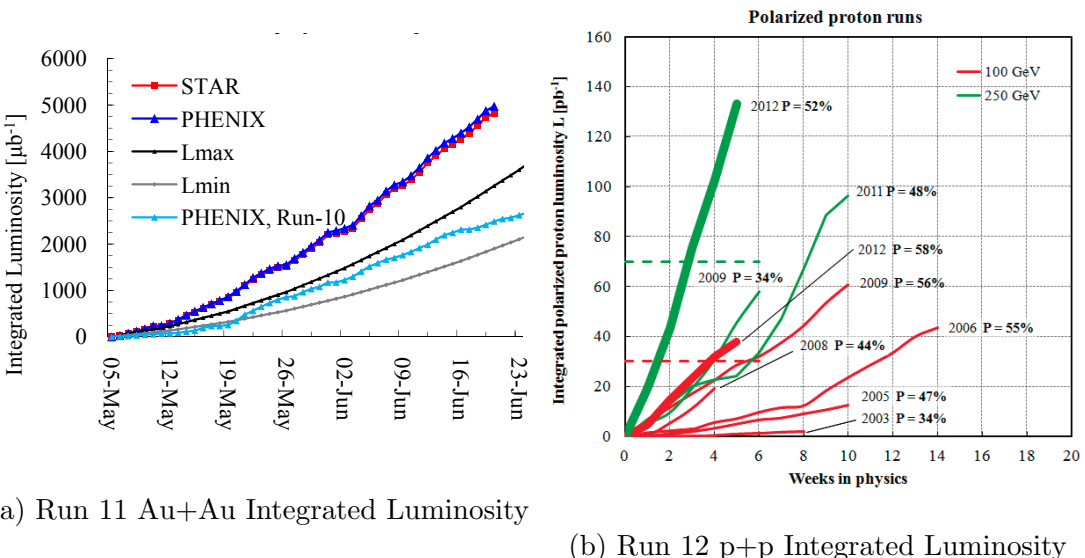


Figure 3.1: Integrated luminosities for run 11 and run 12 in RHIC. Left plot shows Au+Au delivered to STAR and PHENIX as well as run 10 in PHENIX for comparison. Right plot shows all p+p runs, run 12 is shown with thick lines.

tower trigger requires that a hit in a BEMC tower exceeds an ADC threshold determined such that the transverse energy in that tower is high. In run 11 we use the HT triggers NPE11, NPE15, NPE18, and NPE25 which are in increasing order of  $E_T$ . The NPE11 and NPE15 triggers are also prescaled. In p+p we use the BHT0, BHT1, BHT2, and BHT3 triggers, of these only BHT0 is prescaled.

Due to the large dataset sizes it is in our best interest to cut down on the data we need whenever possible. We do this first when we read the data to make BEMC points to match to tracks. Here we look through the tracks in the event and search for electron candidates based on the TPC information only. We throw out events without viable electron candidates. Since these cuts are looser than the electron cuts we will apply later we don't remove events we might actually want and we retain the ability to tighten the cuts later if we need to. After limiting ourselves to high tower triggers and keeping only events with electron candidates we are left with approximately 23 million events in Au+Au and 1.1 million events

Variable	Cut
Triggers (Au+Au)	NPE11 NPE15 NPE18 NPE25
Triggers (p+p)	BHT0 BHT1 BHT2 BHT3
$ V_z^{TPC} $ (Au+Au)	$\leq 30$ cm
$ V_z^{TPC} $ (p+p)	$\leq 40$ cm
$ V_z^{TPC} - V_z^{ZDC} $ (Au+Au only)	$\leq 4$ cm

Table 3.1: Datasets used in the analysis as well as the cuts applied at the event level.

in p+p.

### 3.2.2 Event Level Cuts

At the event level we cut on events with vertex too far out of the center of the detector. We use the tracks in the TPC to reconstruct the vertex, we can also measure the vertex with the Vertex Position Detector (VPD). By convention we have the  $x$  and  $y$  axes as transverse to the beam line. The  $z$  axis then runs along the beam. We require that the vertex be no more than 2 cm from the center of the beam pipe in the radial direction, i.e.  $\sqrt{(V_x^{TPC})^2 + (V_y^{TPC})^2} \leq 2$  cm. We also cut on the TPC vertex in the  $z$  direction, choosing events with  $|V_z^{TPC}| \leq 30$  cm in Au+Au collisions and  $|V_z^{TPC}| \leq 40$  cm in p+p. Additionally we want to have good agreement between the vertices as measured by the TPC and VPD. We require that the difference between the measured  $V_z$  satisfies  $|V_z^{TPC} - V_z^{VPD}| \leq |4$  cm in Au+Au. Figure 3.2 shows the distribution of  $V_z^{TPC}$  and the difference in TPC and VPD  $V_z$  in Au+Au collisions. In p+p because of lower multiplicity and a wider vertex distribution the measured vertex from VPD is not reliable and thus the cut on the difference of  $V_z$  is not used.

At the event level we also determine the centrality using the STAR `StRefMultCorr`

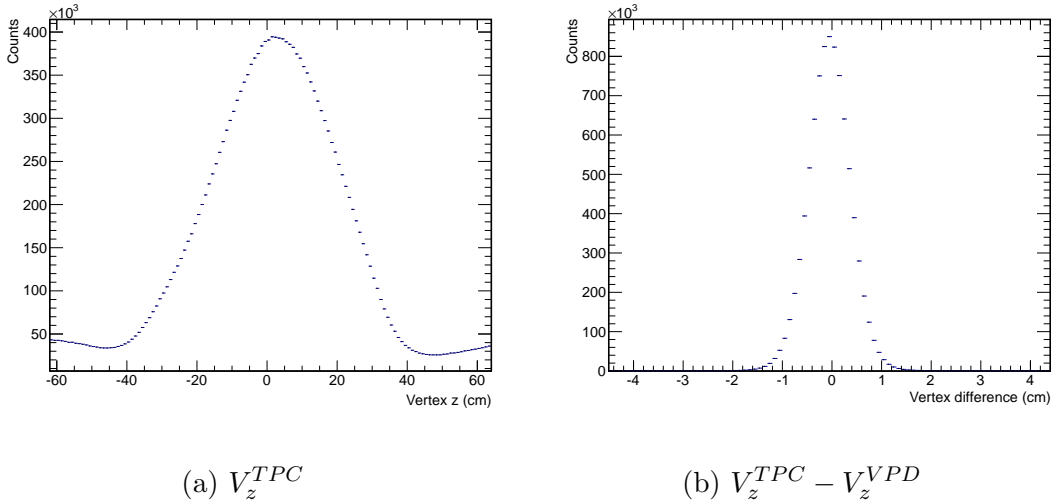


Figure 3.2: Vertex z distribution in run 11 Au+Au. Left plot shows the distribution of the z vertex (cut at  $\pm 30$  cm), right plot shows the difference between TPC and VPD  $V_z$  (cut at  $\pm 4$  cm).

class which calculates the centrality bin based on the reference multiplicity (refmult), vertex z, run number, and ZDC coincidence rate. Figure 3.3 shows the event by event distribution of refmult as well as the number of events from each centrality bin used in the NPE analysis.

### 3.3 Track Reconstruction and TPC Cuts

The TPC is the primary tracking and particle identification system in STAR. Charged particles traverse the TPC chamber which ionizes the gas inside. Due to the nearly uniform electric field in the TPC these ions drift to the ends of the TPC where the currents are read out by the TPC padrows. The magnetic field in the TPC causes charged particle trajectories to be helical making charge sign distinction possible. We can also use the TPC for particle identification by measuring the ionization energy loss in the detector.

In the TPC we consider two types of tracks. The global tracks are those

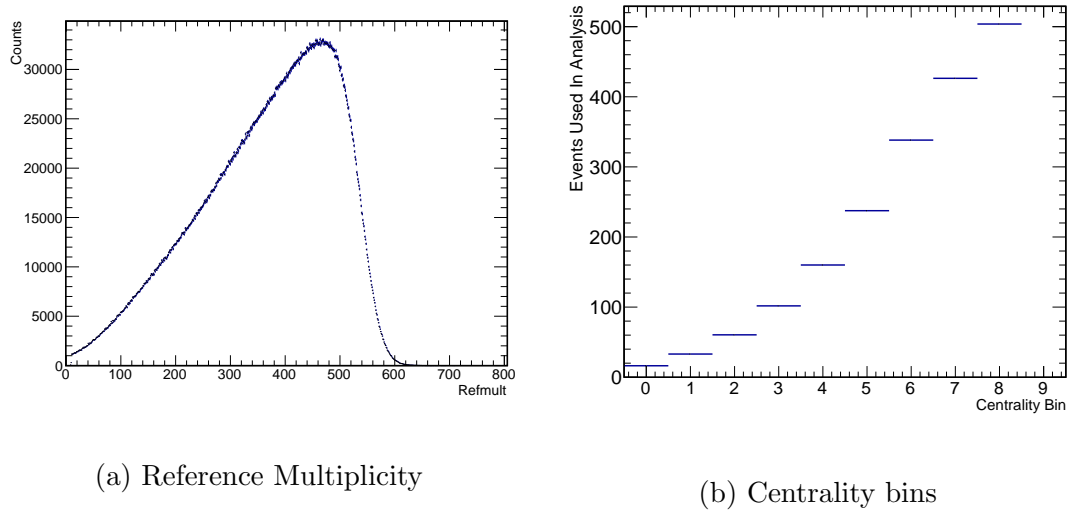


Figure 3.3: Reference multiplicity and centrality bin distributions for HT trigger events in Au+Au.

tracks from the fit to hits inside the TPC. If a global track has a distance of closest approach (DCA) to the primary vertex less than 3 cm then the primary vertex is added to the track hits and the track is refit. The resulting track is a primary track, which should represent particles coming directly from the collision.

We impose track quality cuts to make sure the track fits are good and that we get a good measurement of  $dE/dx$ . For primary tracks we require the number of TPC hits used in the track fit is between 20 and 50. For global tracks we only require that the number of hits is above 15. For all tracks we also cut on the ratio of hits fit to the maximum number possible keeping it between .52 and 1.05.

In run 11 and run 12 we have no tracking information near the beam pipe, the Silicon Vertex Tracker was removed before the runs and the new Heavy Flavor Tracker had not been installed. Due to the relatively short decay length ( 100  $\mu\text{m}$ ) of  $D$  and  $B$  mesons this means that the decay vertex of these particles can not be distinguished from the primary vertex. For electron candidates we require primary tracks with DCA of less than 2 cm. The corresponding global track for that electron must also be less than 3 cm.

Variable	Cut
TPC Hits (Primary Tracks)	$\in (20, 50)$
TPC Hits (Global Tracks)	$\geq 15$
$N_{\text{hits}}/N_{\text{possible}}$	$\in (.52, 1.05)$
Primary DCA	$< 2.0\text{cm}$

Table 3.2: Quality cuts used for TPC tracks.

The energy loss ( $dE/dx$ ) in the TPC is modeled by the Bichsel function which also accounts for the spread in values for different particle species. We will be looking at the deviation of the energy loss compared to the Bichsel function value for electrons. This quantity is called  $n\sigma_e$  and is defined as:

$$n\sigma_e = \frac{\log \frac{dE/dx}{B_e}}{\sigma_e} \quad (3.1)$$

where  $B_e$  is the Bichsel function value and  $n\sigma_e$  is the deviation from the mean Bichsel function value for electrons. Analogous values are defined for protons, kaons, and pions but we will only concern ourselves with  $n\sigma_e$ . We will go over the specific  $n\sigma_e$  cuts used when we discuss the details of electron identification.

### 3.4 BEMC Points and Matching

The BEMC is critical to the identification of high  $p_T$  electrons in STAR. In Au+Au and p+p collisions hadrons (mostly pions and protons) greatly outnumber electrons and the  $n\sigma_e$  cuts in the TPC are not enough to give an acceptable electron purity. With the BEMC electron identification is possible at high  $p_T$ , in the calorimeter electrons are much more likely to interact in the first few layers of the calorimeter and they will also deposit their entire energy within the tower.

The barrel information in an event gives us hits for the BEMC towers as well as

hits in the  $\eta$  and  $\phi$  directions for the shower max detector. From this information we need to cluster the tower hits as well as find hits in the SMD. Then we need to take the BEMC points (tower cluster and SMD hits) and associate it with a track from the TPC. We want to cluster the tower and SMD hits such that each BEMC point is associated with one electron. With the combined TPC and BEMC information we can identify the high  $p_T$  electrons necessary for our analysis.

We will now describe the UCLA BEMC point making program and will use the following definitions:

- **Tower cluster:** Group of tower hits according to some clustering criterion.
- **BSMD hit:** Signal in a single strip in the BSMD in either  $\phi$  or  $\eta$ .
- **BSMD cluster:** Group of BSMD hits in either  $\phi$  or  $\eta$ .
- **BSMD point:** Pair of clusters, one from  $\phi$ , the other  $\eta$ , which give a spatial point on the detector.
- **BEMC point:** A tower cluster and an associated BSMD point which will be matched up with tracks from the TPC.

To use the UCLA EMC point maker, described in detail in ref, to construct points and associate them with TPC tracks. The first step in reconstructing the BEMC points is to find and cluster the hits in the BEMC towers. To do this we first look for seed towers which have deposited energy above .1 GeV/c. Once we have found a seed tower adjoining towers within the same BEMC module are clustered with the seed, there is no clustering of towers or SMD hits across the modules.

The BSMD uses a similar clustering procedure for both the  $\phi$  and  $\eta$  directions. If EMC towers and BSMD clusters are found then the program will check for multiple clusters and attempt to merge them by relaxing the SMD clustering

criteria. If one direction in the BSMD has no hits then clustering is rerun with relaxed criteria to try and find a good SMD point for that module. If neither tower nor SMD clusters are found in a module then the algorithm moves on to the next module.

With clusters in the towers and possibly the SMD found we move on to associating tower clusters to SMD hits. We only use SMD hits adjacent to the tower cluster and if there is only one SMD point associate it with the cluster. For the case of multiple SMD hits adjacent to the tower the tower energy is divided between the SMD points. If there are no points in the SMD but we still have tower clusters then the tower cluster is kept but not used as a BEMC point for matching with the TPC. The SMD info is used as the  $\phi$  and  $\eta$  location of the hit and the tower cluster is used for the point's energy. Figure 3.4 shows the distribution of SMD points in  $\phi$  and  $\eta$ .

From the TPC we only consider tracks with  $p_T$  above 1.5 GeV/c for association with points in the BEMC. When the TPC tracks are reconstructed they are fit to a helix to describe their trajectory through the TPC magnetic field. We then project these helices to the inner surface of the BEMC. After the projection we then associate the track with a BEMC point. We require that the distance between the points ( $d = \sqrt{\Delta\phi^2 + \Delta\eta^2}$ ) be smaller than .05. If multiple BEMC points are close enough to be matched, then we select the one with the smallest distance. In general tracks from electrons will match better to the points in the BEMC, we will use this to improve the cuts for electron identification which will be discussed in the next section.

### 3.5 Electron Identification

We can now use the matched TPC tracks and BEMC points to identify electrons in Au+Au and p+p collisions. We will use the TPC information to find tracks that

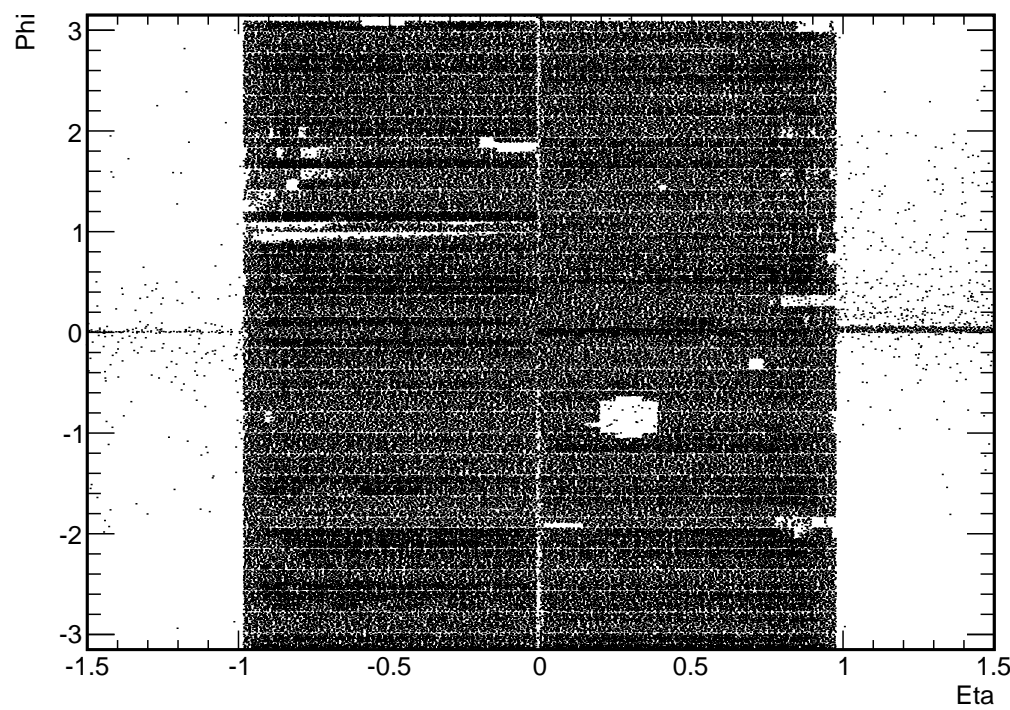


Figure 3.4: SMD points in  $\eta$  and  $\phi$  for the EMC points used in the analysis

originate from the primary vertex, traverse the TPC depositing energy consistent with what we would expect from electrons, then interact in the first few layers of the BEMC leaving a wide shower that terminates within the tower.

### 3.5.1 BEMC Cuts

Our analysis only uses data from high tower trigger events. The only requirement for a high tower trigger is that a tower in the event register a hit above a certain threshold. There is no guarantee that the tower will be matched to a track or that an electron triggered the tower. However we may still find electrons in these events they will just be below the trigger threshold. This effect is called random trigger benefit and it is important to remove in NPE analyses where the production cross-section of NPE is important. It is likely not critical in this analysis because we will be looking at correlations which are normalized per trigger but we still attempt to cut out the random trigger benefit.

When we make the BEMC points we also record the highest tower ADC value in the BEMC cluster and record this as the ADC0 for that point. Figure 3.5 shows the distribution of ADC0 from primary tracks matched to BEMC points. Near 325 ADC counts we see a large rise in the ADC0 of points, this corresponds to the threshold for the NPE18 trigger. Any electrons with ADC0 much below this value can be assumed to come from random trigger benefits and are not used.

For NPE, due to the short lifetime of the parent mesons, we only consider tracks originating from the primary vertex. Further we cut on the DCA of the track to the primary vertex, requiring that the DCA be less than 1.5 cm. This cut is tighter than the 2 cm cut we used when considering the TPC track quality. We also remove tracks with  $p_T > 2.0 \text{ GeV}/c$ , generally the tracks coming from triggered electrons will be much higher than this anyway. For our acceptance we want the electron to be  $-0.7 \leq \eta \leq 0.7$  in pseudorapidity. This corresponds to

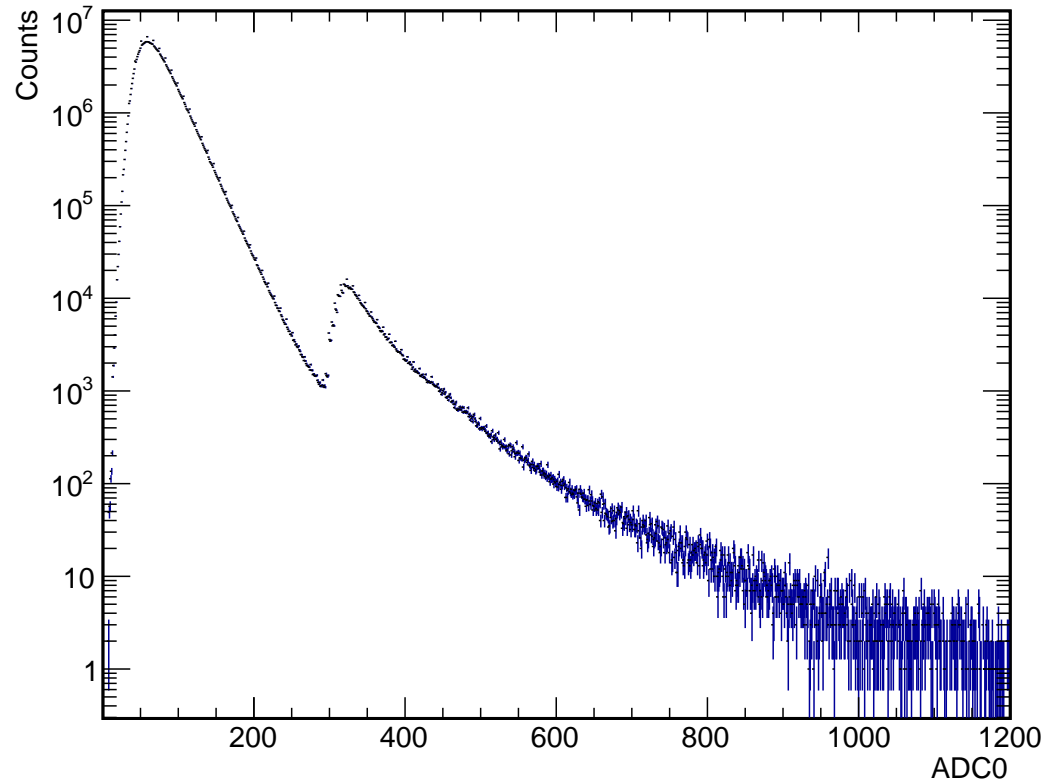


Figure 3.5: ADC0 for primary tracks in NPE18 triggered events. Turn on of the NPE18 trigger is apparent around 325 ADC counts.

the  $\eta$  acceptance of the BEMC. Run 10 analyses also cut out areas in  $\phi$  which correspond to the position of the SVT support structure. The reasoning behind that cut is that the remaining structure could cause more photon conversions in those regions, but this cut is not applied here.

Now we apply the BEMC information to select electrons. Electrons begin showering much earlier in the BEMC than hadrons, the SMD sits at  $5.6X_0$  where electromagnetic showers are widest. With more hits in the SMD the spatial resolution of the BEMC points is better as so the BEMC matching for electrons tends to be better. This is illustrated in Figures 3.6 and 3.7 which show the BEMC matching in  $\Delta\phi$  and  $\Delta Z$ . Black points are for all matched primary tracks and red points show the matching for identified electrons (with the matching cuts excluded). We set the  $\Delta\phi$  cut such that  $|\Delta\phi| \leq .013$  and for  $\Delta Z$  we use  $-2.5 \text{ cm} \leq \Delta Z \leq 1.1 \text{ cm}$  (for  $\eta > 0$ ) and  $-1.5 \text{ cm} \leq \Delta Z \leq 1.9 \text{ cm}$  (for  $\eta < 0$ ). Figure 3.7 different cuts on  $\Delta Z$  are applied in the different halves of the TPC due to a discreet jump when crossing the central membrane of the TPC.

The wider showers for electrons also make it possible to cut on electrons based on the number of hits in the BSMD. The strips in the SMD are approximately twice the Moliere radius for electrons in lead, thus for developed EM showers we expect to see hits in multiple strips. Most hadrons will not leave hits in the BSMD, but since we are only considering reconstructed points in the BEMC we know that we will have at least one hit in both  $\eta$  and  $\phi$  in the SMD. Figure 3.8 shows the hits in the SMD for hadrons and for photonic electrons. We show the cuts with photonic electrons because without the SMD cuts the sample of BEMC points is not pure enough to illustrate the difference in behavior between hadrons and electrons. For electrons we require that number of strip hits in both  $\phi$  and  $\eta$  be greater than or equal to 2.

We can also select for electrons by looking at how much energy tracks deposit into the BEMC towers. The towers of the BEMC are around 20 radiation lengths

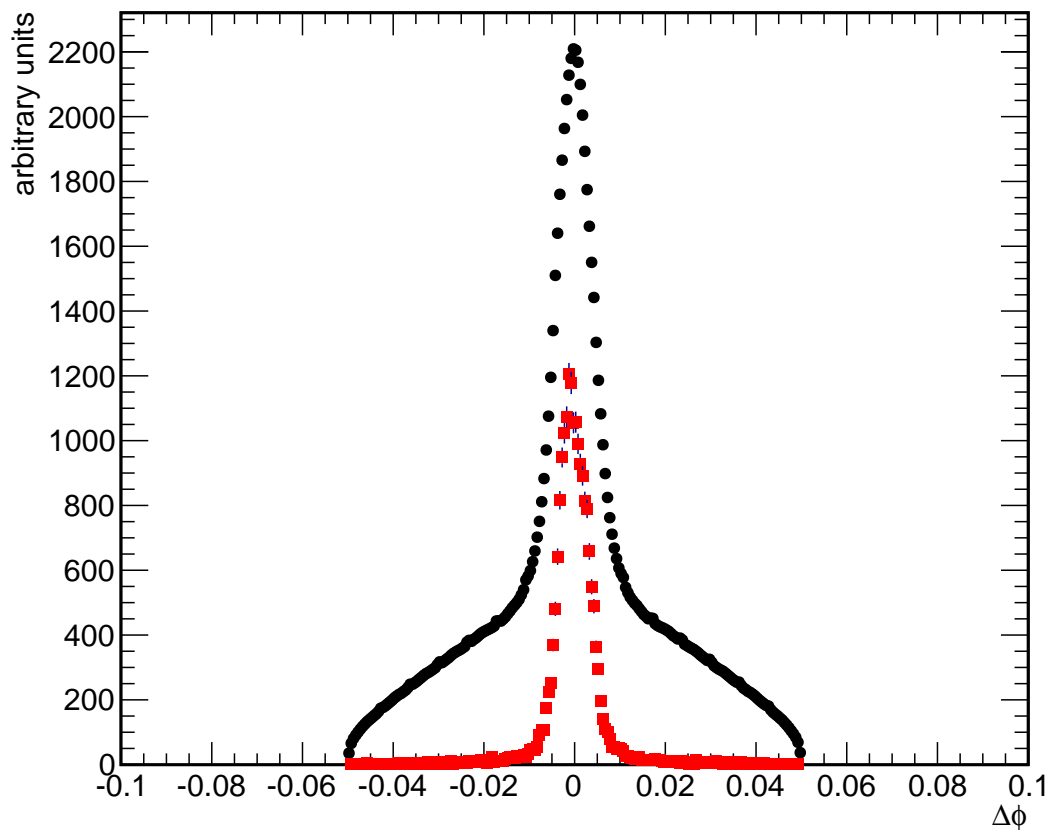
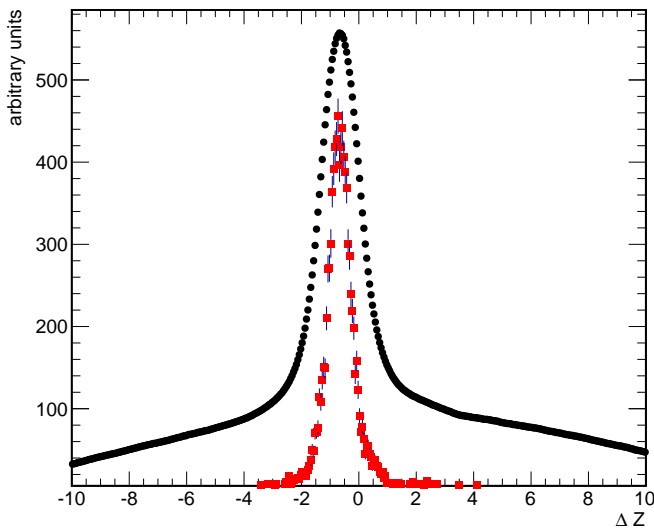
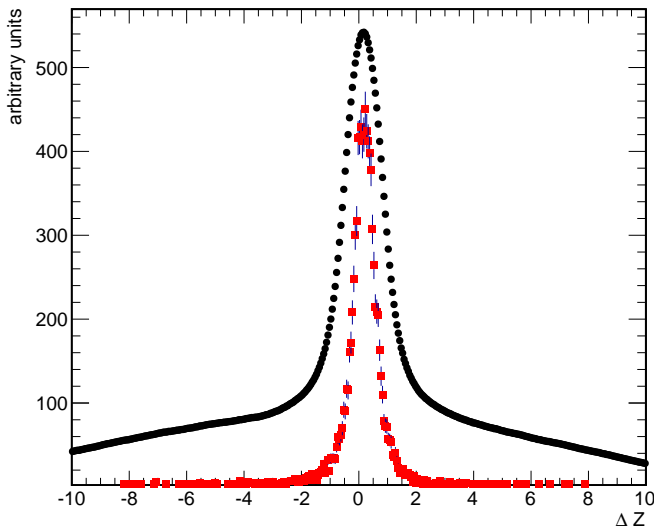


Figure 3.6:  $\Delta\phi$  between the TPC and BEMC for all matched primary tracks (black) and identified electrons (red). Y-axis is arbitrary units scaled to show all tracks and electrons on the same figure. Matching is better for electrons and we cut on such that  $|\Delta\phi| \leq .013$ .

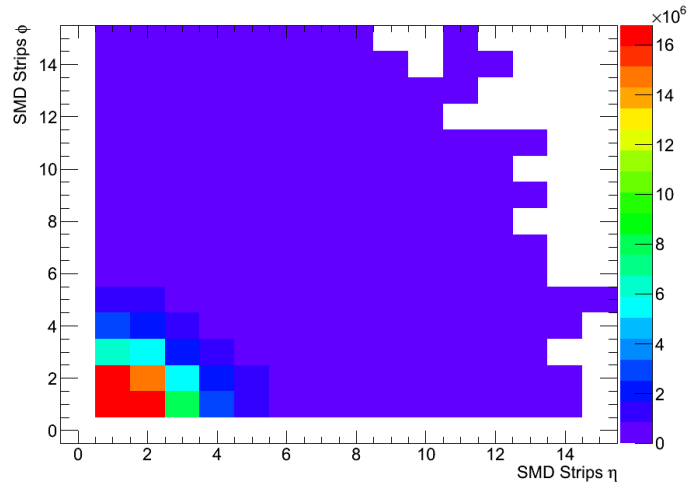


(a)  $\eta > 0$

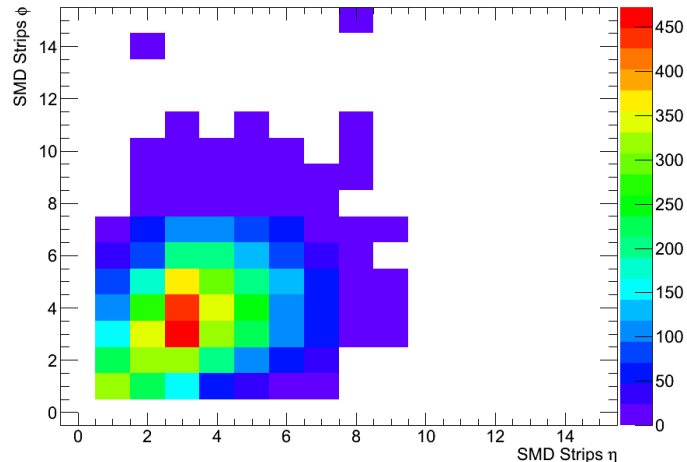


(b)  $\eta < 0$

Figure 3.7:  $\Delta Z$  of the TPC track to BEMC point for all points and for electrons. Different cuts are used in the two halves of the TPC due to a jump when moving from the positive  $\eta$  region to negative.



(a) Hadrons



(b) Photonic electrons

Figure 3.8: SMD strip hits for hadrons and electrons. For the electron sample we take photonic electrons (a relatively pure electron sample) and remove the SMD cuts to see the number of strip hits in each direction.

thick meaning electrons will shower and deposit all of their energy within the tower. Hadrons or muons are not likely to develop full showers in the tower and we can use this to pick out electrons. We are interested in the  $E/p$  ratio for tracks hitting the BEMC. For high  $p_T$  electrons, they will deposit all of their energy  $E$  in the tower and since we are at high  $p_T$  ( $> 2 \text{ GeV}/c$ ) we also expect that  $E \approx pc$ . Thus for electrons we should see  $E/p \approx 1$  (ignoring factors of  $c$ ). Figure 3.9 shows the  $E/p$  shape for electrons before applying  $E/p$  cuts and hadrons. Peak is seen for electrons around 1, we set the cut for electrons to be  $.5 \leq E/p \leq 1.7$ .

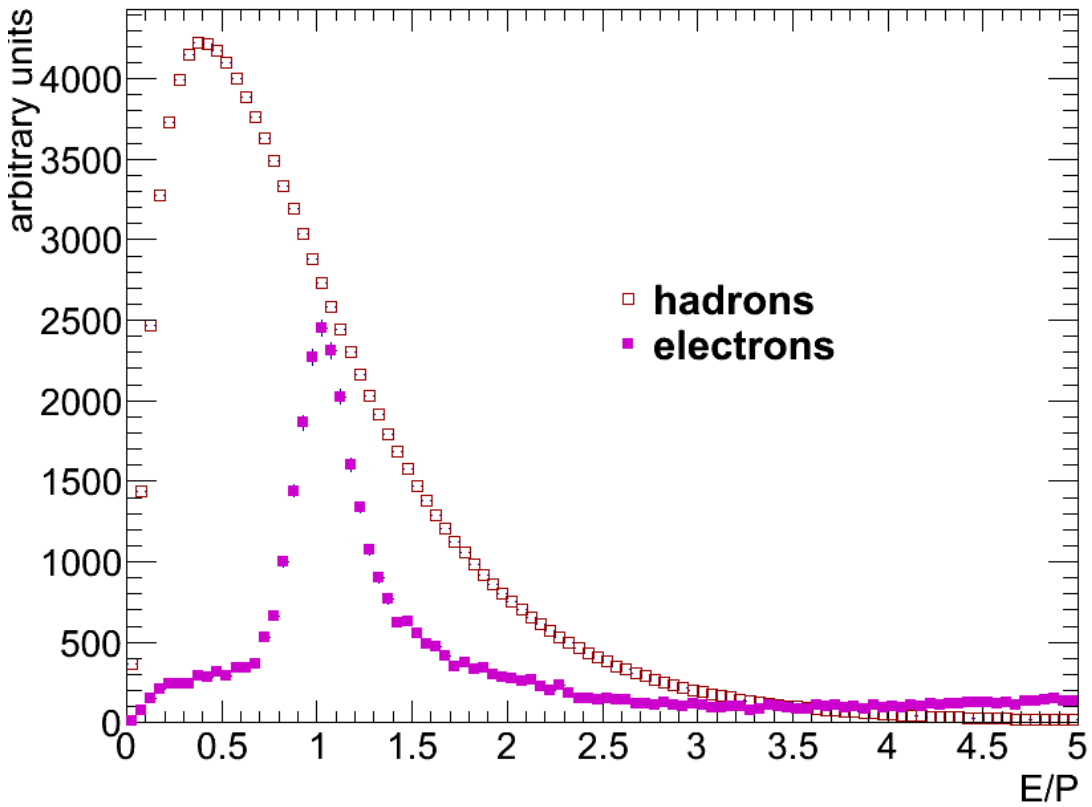


Figure 3.9:  $E/p$  for points in the BEMC for electrons (without  $E/p$  cut applied) and hadrons. Scale is arbitrary to show both cases. Electron cut is set  $.5 \leq E/p \leq 1.7$ .

Variable	Cut
Track Type	$< .5$ (Primary)
$\eta$	$\in (-.7, .7)$
Charge	$\pm 1$
ADC0	$\geq 205,270,325,425$ (NPE11/15/18/25)
SMD $\phi$ Strips	$\geq 2$
SMD $\eta$ Strips	$\geq 2$
$E/p$	$\in (.5, 1.7)$
DCA Global	$\leq 1.5$
BEMC $\Delta\phi$	$\in (-.013, .013)$
BEMC $\Delta Z$ ( $\eta > 0$ )	$\in (-2.5, 1.1)$
BEMC $\Delta Z$ ( $\eta < 0$ )	$\in (-1.5, 1.9)$

Table 3.3: Track level electron cuts, excluding  $n\sigma_e$ , cuts for Au+Au collisions.

Table 3.3 summarizes the electron cuts used so far, for the most part these cuts are applied to all tracks equally and do not depend on the track  $p_T$  (the ADC0 cuts being an event-by-event exception). In the next section we will show the  $n\sigma_e$  cuts which will depend on the track  $p_T$  and then later we will look at the overall electron purity that these cuts give to our inclusive sample.

### 3.5.2 TPC Cuts

The only remaining cuts are those for ionization energy loss in the TPC. The energy loss varies significantly for different particle species as a function of the particle's momentum. Since we are looking for electrons the cuts we will be applying to tracks are based on the calculated  $n\sigma_e$  as defined in Equation 3.1. For electrons  $n\sigma_e$  should be distributed around 0, but for negative values of  $n\sigma_e$  the electrons are overwhelmed by contamination from hadrons. We keep these cuts

$p_T$ Range	$n\sigma_e$ Cut
1.0 GeV/c < $p_T$ < 2.0 GeV/c	-1.25 < $n\sigma_e$ < 2
2.0 GeV/c < $p_T$ < 4.0 GeV/c	-0.75 < $n\sigma_e$ < 2
4.0 GeV/c < $p_T$ < 6.0 GeV/c	-0.25 < $n\sigma_e$ < 2
6.0 GeV/c < $p_T$ < 7.0 GeV/c	0.25 < $n\sigma_e$ < 2
7.0 GeV/c < $p_T$ < 8.0 GeV/c	0.25 < $n\sigma_e$ < 2
8.0 GeV/c < $p_T$ < 10.0 GeV/c	0.5 < $n\sigma_e$ < 2
10.0 GeV/c < $p_T$ < 12.0 GeV/c	0.5 < $n\sigma_e$ < 2

Table 3.4:  $n\sigma_e$  cuts as a function of  $p_T$ .

the same as they are in the run 10 NPE analysis, but they could be further tuned to improve electron purity and efficiency. Table 3.4 summarizes the  $n\sigma_e$  cuts used for electron identification. The cuts are the same for both Au+Au and p+p data.

### 3.6 Electron Purity

We will now investigate the purity of the electron sample we get from applying our electron identification cuts. To do this we will be relying on the  $n\sigma_e$  distributions we have measured. First we will look at the  $n\sigma_e$  distributions with all of the BEMC and track quality cuts applied. Then we will fit the peaks in  $n\sigma_e$  with gaussian functions, apply the  $n\sigma_e$  cuts as established in Table 3.4, and then calculate the yields from the electron and hadron peaks. This will give us an estimate of the purity of the electron sample we will use in the NPE analysis.

Figure 3.10 shows the  $n\sigma_e$  distributions as well as the fit functions. Each distribution was fit with three gaussian functions, one each for  $e^\pm$ ,  $\pi^\pm$ , and a final function for  $K^\pm + p^\pm$  combined. To estimate the purity we take the parameters (height,  $\mu$ ,  $\sigma$ ) gaussian component of the electron and hadron peaks. Then we integrate the peaks over the range specified by the  $n\sigma_e$  cuts. The purity is then

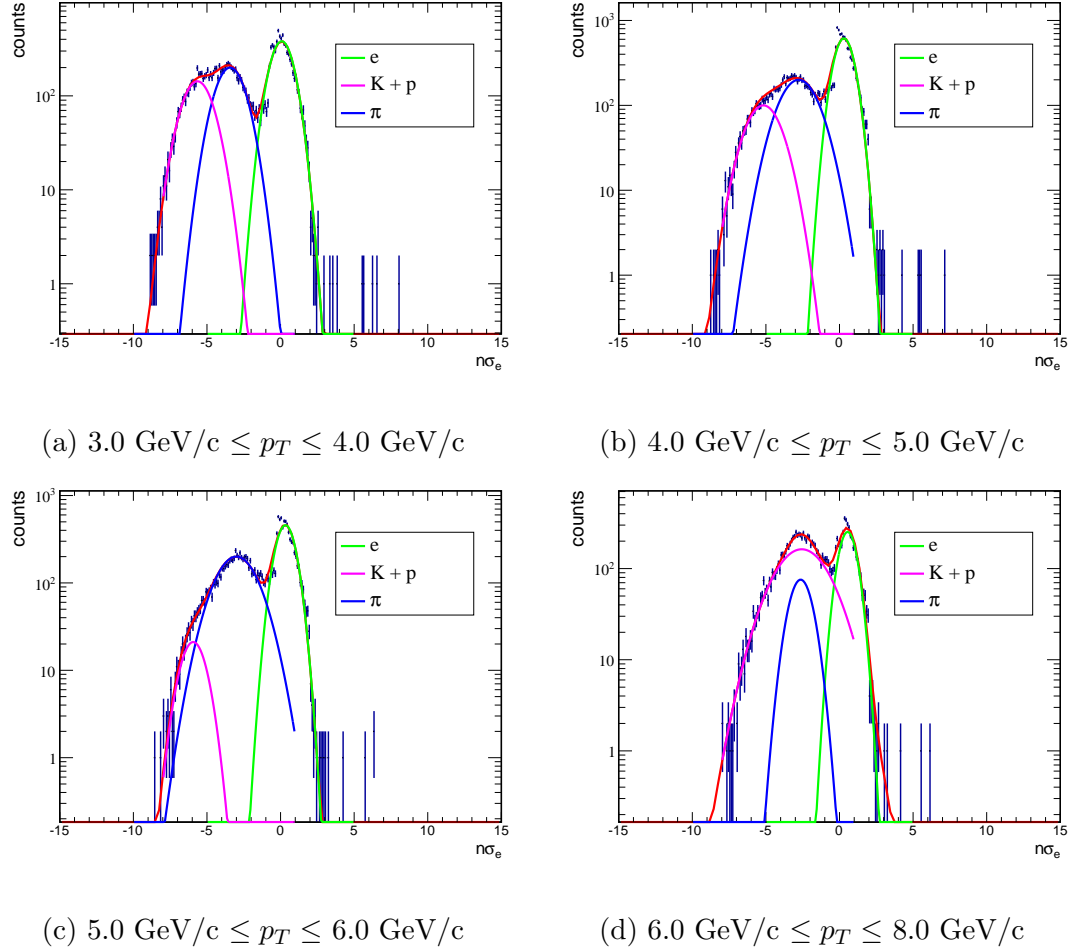


Figure 3.10: Fits to the  $n\sigma_e$  distributions for primary electron candidates (particles that pass all electron cuts excluding the  $n\sigma_e$  cut) as a function of particle  $p_T$ .

Electron $p_T$	Purity
$3.0 \text{ GeV}/c < p_T < 4.0 \text{ GeV}/c$	99.8%
$4.0 \text{ GeV}/c < p_T < 5.0 \text{ GeV}/c$	97.0%
$5.0 \text{ GeV}/c < p_T < 6.0 \text{ GeV}/c$	96.1%
$6.0 \text{ GeV}/c < p_T < 8.0 \text{ GeV}/c$	79.6%

Table 3.5: Purity of electrons obtained from fits to  $n\sigma_e$ .

the fraction of the total yield that comes from the electron peak. Table 3.5 lists the purities obtained by this method for a range of electron  $p_T$ . Below 6  $\text{GeV}/c$  the purity is quite high between 96% and 100%, it begins to drop for higher  $p_T$  due to narrowing and shifting of the electron peak as well as closer merging of the hadron peaks with the electrons. The peak shape is biased by the fact that we only select events with high  $p_T$  tracks and  $n\sigma_e$  within certain values. This causes the peaks to have non-gaussian features and prevents us from taking the purities obtained at face value. However, in this analysis we will not directly need the electron purity unlike if we were looking at NPE  $v_2$ . We will be normalizing our observations per trigger particle, so we only need to look at purity to estimate the contribution of hadron contamination in the NPE sample when we construct NPE-h correlations.

### 3.7 Photonic Electron Identification

The main background to electrons from the decay of heavy flavor mesons comes from photon conversions in the detector and Dalitz decay of  $\pi$  and  $\eta$  mesons. Collectively we refer to these background electrons as *photonic electrons*, and in this section we will summarize how we remove them from our electron sample. When the electrons are produced by these background processes they come in  $e^+e^-$  pairs. To tell whether an electron is of photonic origin we search through

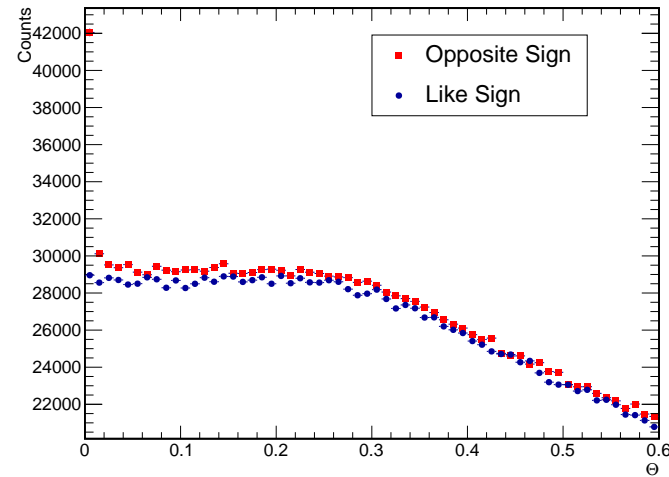
Variable	Cuts
TrackType	Global
$\eta$	$\in (-1.3, 1.3)$
$p_T$	$> 0.3 \text{ GeV}/c$
Pair DCA	$< 1.0 \text{ cm}$
Pair $\Theta$	$< 0.05$
Pair $\phi$	$< 0.10$
2D Invariant Mass	$< 0.10 \text{ GeV}/c^2$

Table 3.6: Cuts used for partner tracks and for identifying photonic electrons.

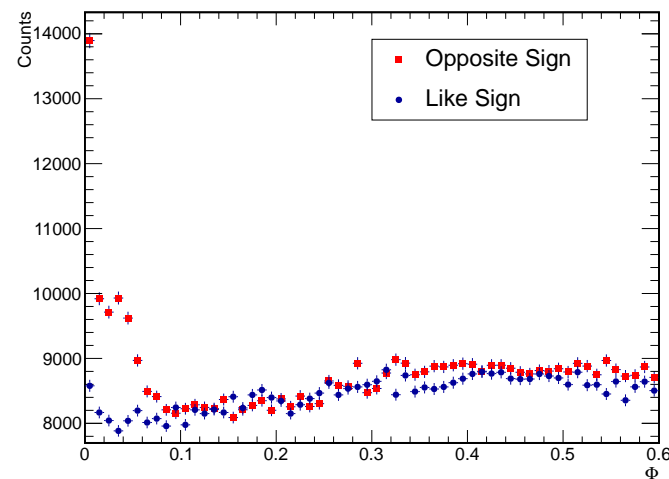
the tracks in the event and try to find its partner.

When searching for the partner electron we use very relaxed cuts. We search through all global tracks (rather than primary) within a pseudorapidity of  $-1.3 \leq \eta \leq 1.3$ . To cut out hadrons we require that  $-3 \leq n\sigma_e \leq 3$ . Tracks from photonic background will be very close together in the detector and will have a small opening angle. We apply cuts on the pairwise DCA of the two tracks, requiring the DCA be less than 1.0 cm. Also the opening angle between the tracks should be small, we want the total angle  $\Theta < 0.05$  and the azimuthal angle  $\phi < 0.1$ . Table 3.6 summarizes the track cuts and pairing criteria for reconstructing photonic electrons. The partner for a photonic electron must have opposite charge to the primary track. We look for both opposite-sign as well as like-sign pairs. The like sign pairs which satisfy the photonic partner cuts let us estimate the number of photonic electrons that are misidentified due to combinatorial pairing of tracks.

For photonic electrons we expect the pair of particles to have a low invariant mass (exactly 0 for photon conversions and  $< .1 \text{ GeV}/c^2$  for Dalitz decays). However the measurement of the invariant mass is degraded by the finite tracking



(a) Pair  $\Theta$



(b) Pair  $\phi$

Figure 3.11: Angle cuts for partner tracks used to reconstruct photonic electrons.

resolution of the TPC. Reconstructed TPC tracks form helices in the detector volume. The resolution of the TPC effectively means that the helices can shift around relative to each other. Due to this effect, there is a large uncertainty in the location of the secondary vertex where the electrons have their minimum DCA. This causes an uncertainty in the opening angle between the tracks and smears out the invariant mass distribution of the pairs. To correct this we instead consider the 2D invariant mass. The tracks are rotated into the same plane before calculating the mass. The cutoff for photonic electrons is that this 2D invariant mass be below  $.10 \text{ GeV}/c^2$ . Figure 3.12 shows the 2D invariant mass distribution. The 3D invariant mass is not used in identifying photonic electrons but is plotted in Figure 3.13. The peak near 0 is from photon conversions while the peak at  $.05 \text{ GeV}/c^2$  comes from the Dalitz decays. The Dalitz decay is a three body decay and thus the missing photon causes the mass peak to be smeared.

### 3.8 Photonic Electron Reconstruction Efficiency

Clearly just pairing up all tracks to look for photonic electrons will not guarantee that we remove all of the background. It is possible for the partner track to be outside of our acceptance or otherwise fail to pass the photonic electron cuts. We will quantify how much background we miss by the parameter  $\epsilon_\gamma$ , the photonic reconstruction efficiency, which is essentially the fraction of all photonic electrons we are able to reconstruct from searching for partner tracks. This section will discuss how  $\epsilon_\gamma$  is calculated.

We calculate the photonic electron reconstruction efficiency by using embedding simulations. Photon conversions and Dalitz decays of pions are simulated and then embedded into real STAR data. The data are generated flat in  $p_T$  and thus must be weighted according to the measured spectra of  $\gamma$  and  $\pi^\pm$ .

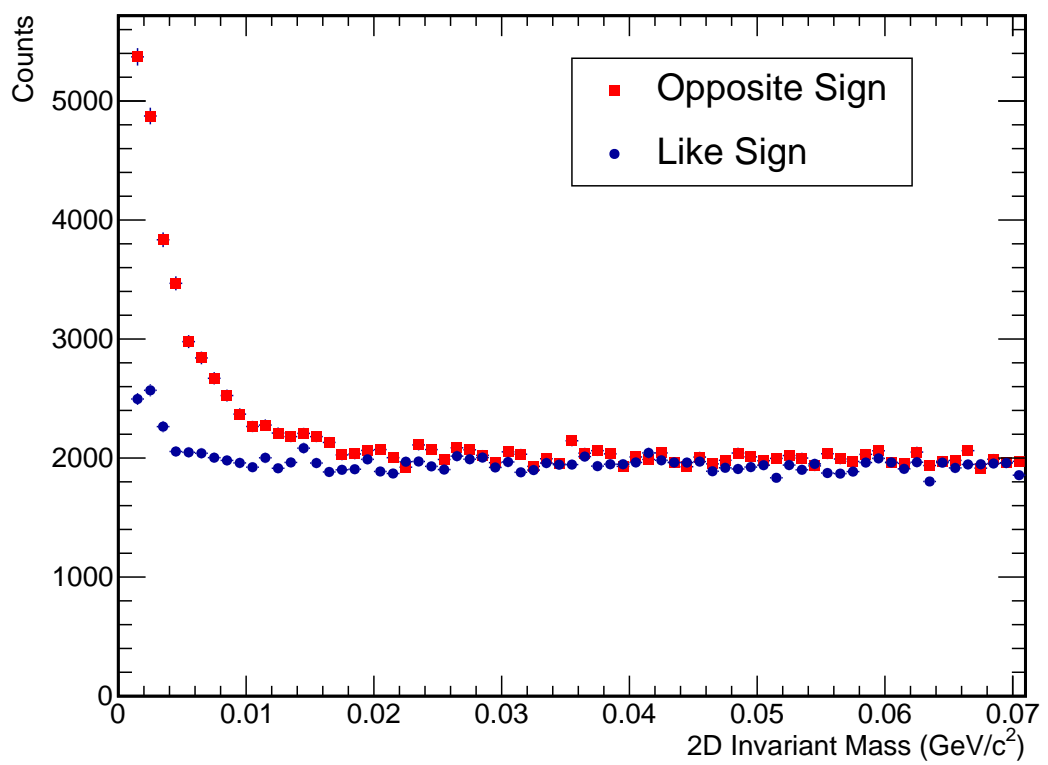


Figure 3.12: 2D invariant mass for opposite sign and same sign pairs. For photonic electron identification we require that  $m_{2D} < 0.10 \text{ GeV}/c^2$ .

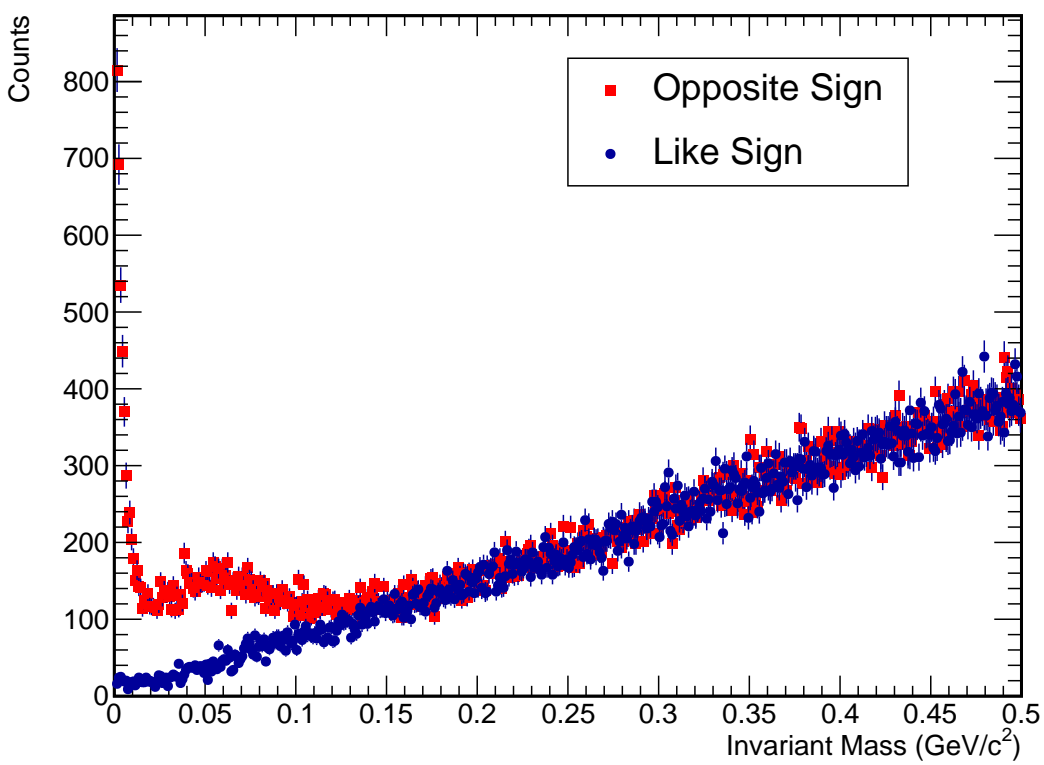


Figure 3.13: Invariant mass distribution for pairs of tracks. Opposite sign pairs show low mass excess which corresponds to the photonic electrons.

# CHAPTER 4

## Azimuthal Correlations of Non-Photonic Electrons to Hadrons

We will now investigate the correlations of triggered non-photonic electrons to hadrons in  $Au + Au$  and  $p + p$  collisions at 200 GeV. Hard processes in these collisions will produce back to back jets in the azimuthal angle  $\phi$ . We search for potential modification of the jet in  $Au + Au$  collisions compared to  $p + p$ .

### 4.1 Overview of Constructing the NPE-hadron Correlation

Several steps are needed to produce the NPE-h correlation. The trigger particle electrons are identified by the procedure described in the previous chapter. The nonuniform acceptance of detector results in false correlations which are not a result of the underlying physics. This is corrected in two ways, the  $\phi$  distribution of all particles is flattened and then the correlations from mixed events are calculated and then a weighting is determined so as to flatten these as well.

In correlations from  $Au + Au$  collisions there is an underlying background correlation from the flow of both the trigger electron and the associated hadron. In this analysis we only consider the second order harmonic of flow,  $v_2$ . For hadrons,  $v_2$  is very accurately measured across a wide range centralities and  $p_T$ . For non-photonic electrons, the measurements of  $v_2$  are not so precise, thus we can only estimate its contribution to the background. This uncertainty will be

reflected in the analysis of systematic error.

We will also look at the dependence of the correlation on the angle between the triggered electron and the event plane. A dependence on this angle could point to path length dependence on the jet suppression in QGP.

## 4.2 Acceptance Corrections

The STAR detector give full  $2\pi$  azimuthal coverage, however there are still regions of the detector which have noticeably poorer efficiency. This causes an uneven azimuthal acceptance which in turn lead to spurious correlations between detected particles. To correct this we need to apply a weighting to each track depending on where it is in the detector.

### 4.2.1 Single Particle $\phi$ -weighting

We begin by correcting for the single particle acceptance in  $\phi$ . The boundaries between sectors produce regions of lower efficiency, also in Run11 one sector of the TPC had noticeably lower efficiency than the rest. These effects are both shown in Figure 4.1.

The dependence of the acceptance on  $\phi$  however is not the same for all tracks. Whether a track crosses a sector boundary or passes through the dead sector will depend on that particular track's geometry. Tracks at low  $p_T$  curve more in the magnetic field and thus the effects of these lower efficiency areas apply to wider regions in track  $\phi$ . The dependence of acceptance on  $p_T$  is shown in Figure 4.2. At low  $p_T$  the dependence is especially strong thus for  $p_T \leq 1$  GeV/c we divide tracks into  $p_T$  bins of .1 GeV/c, which is near the limit of the momentum resolution of the TPC. Above 1 GeV/c the tracks are roughly straight so the effects on acceptance from the sector boundaries and dead sector are consistent bin-to-bin up to arbitrarily large  $p_T$ .

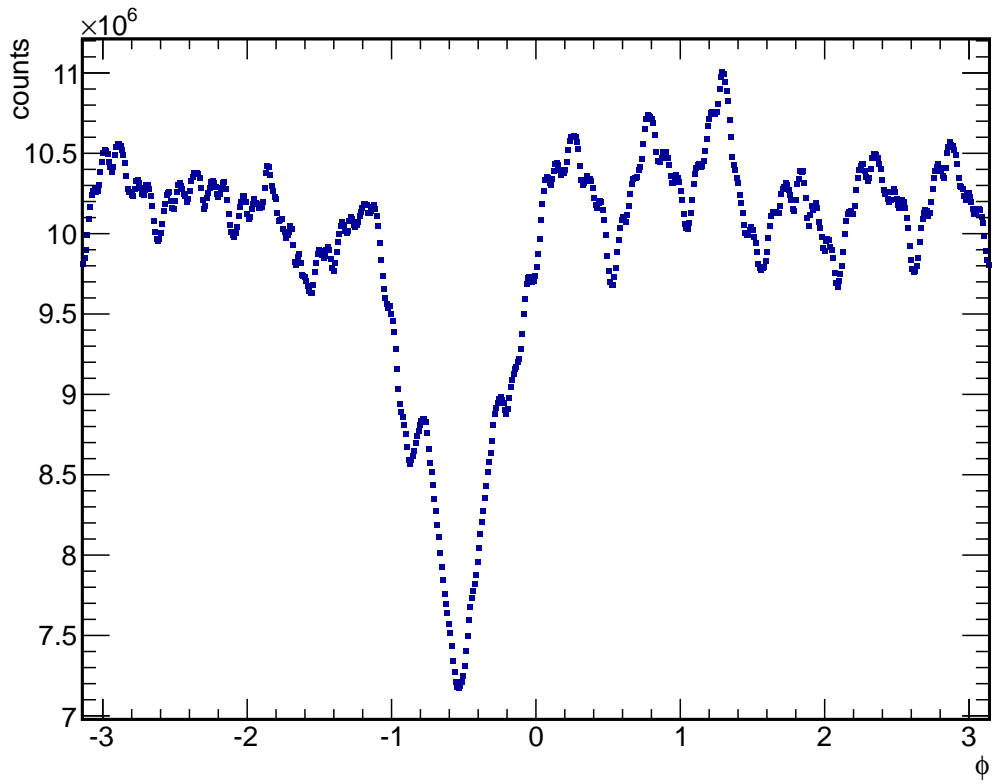
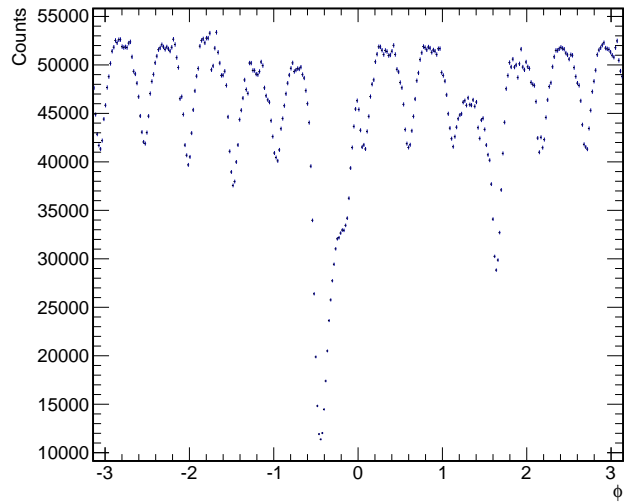
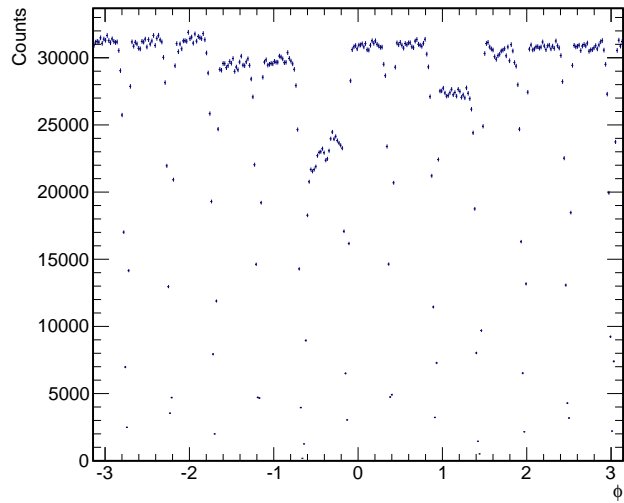


Figure 4.1: The azimuthal angular distribution of all tracks in Run11  $Au + Au$  collisions at 200 GeV. Periodic bumps can be seen from the sector boundaries, as well as a dip in the poorly performing sector.



(a)  $.5 \text{ GeV}/c \leq p_T \leq 1.0 \text{ GeV}/c$



(b)  $1.5 \text{ GeV}/c \leq p_T \leq 2.0 \text{ GeV}/c$

Figure 4.2:  $\phi$  distributions for single particles in different  $p_T$  bins. Strong  $p_T$  dependence is seen especially below 1 GeV/c due to the different track geometries.

While the dependence of acceptance on track  $p_T$  is by far the largest effect, we still further subdivide the tracks to make acceptance corrections. It is possible for the acceptance to depend on  $\eta$ , and we are especially concerned with edge effects when  $|\eta| \sim 1$ , thus we divide into 4 even bins in pseudorapidity ranging from -1 to 1.

Likewise we account for dependence on the event vertex (in both  $p + p$  and  $Au + Au$ ) and multiplicity (only for  $Au + Au$ ) by dividing into bins of vertex-z and centrality. For the centrality bin divisions, all centrality bins from 30% – 80% are taken together since in the peripheral bins the statistics are too low to get a reliable acceptance correction.

Finally, since the tracks in the TPC are curved, there will be a dependence on which direction the track curves. For example, two particles may start on opposite sides of a sector boundary separated by some distance in  $\phi$  but both may cross the boundary if they curve in opposite directions. So we need to take separate weightings based on the product of the magnetic field and the particle's charge,  $B \cdot q$ .

After calculating the single  $\phi$  correction we apply it to each track in the analysis whenever we calculate event planes or 2-particle correlations. Since some areas of the detector have very low efficiencies they can introduce huge weights for a small number of particles. This can destabilize results, so we cap the weight an individual particle can get at 5.0.

#### 4.2.2 Mixed Event Background

To further correct for nonuniformities in detector acceptance we use a mixed event weighting. In an ideal detector the correlations of trigger particles to associated hadrons from a different event should be flat, however acceptance effects will result in nonphysical correlations which need to be removed.

Similar to the single particle corrections we divide the mixed event corrections into bins to account for various systematic differences. In mixed event we bin according to associated particle  $p_T$ , triggered particle  $p_T$ , centrality, vertex z position, and  $\eta$ . As in single particle corrections, the most extreme bin to bin variations occur between the low associated  $p_T$  bins.

## 4.3 Background from Flow

### 4.3.1 Measurements of Flow

The motivations behind two-particle correlation studies are typically the investigation of jet modification in QGP and the response of the medium to jets. But even in the absence of jets we still expect to see some correlation within events from flow. The azimuthal anisotropy resulting from the second order flow harmonic,  $v_2$ , of both the trigger and associated particles produces a background shape with the form:

$$B[1 + v_2^{trig}v_2^{asso} \cos(2\Delta\phi)] \quad (4.1)$$

where  $B$  is an overall constant factor. Higher order harmonics  $v_3$ ,  $v_4$ , etc. can also contribute to the background. Large  $v_3$  in particular is a potential explanation for some of the results in dihadron correlations, but these effects are not considered for this analysis.

Hadron  $v_2$  has been measured to high precision in a wide range of  $p_T$  bins at STAR. Figure 4.3 shows the results of STAR  $v_2$  measurements using an event plane method and illustrates the general dependence on  $p_T$  and centrality. To calculate the hadron  $v_2$  we extrapolate the  $v_2$  measurement to the center of the associated hadron  $p_T$  bin. Then when looking at correlations across multiple hadron  $p_T$  bins we use the weighted average of  $v_2$  based on the number of hadrons in each  $p_T$  bin.

Measurements of electron  $v_2$  at STAR have shown that non-photonic electrons

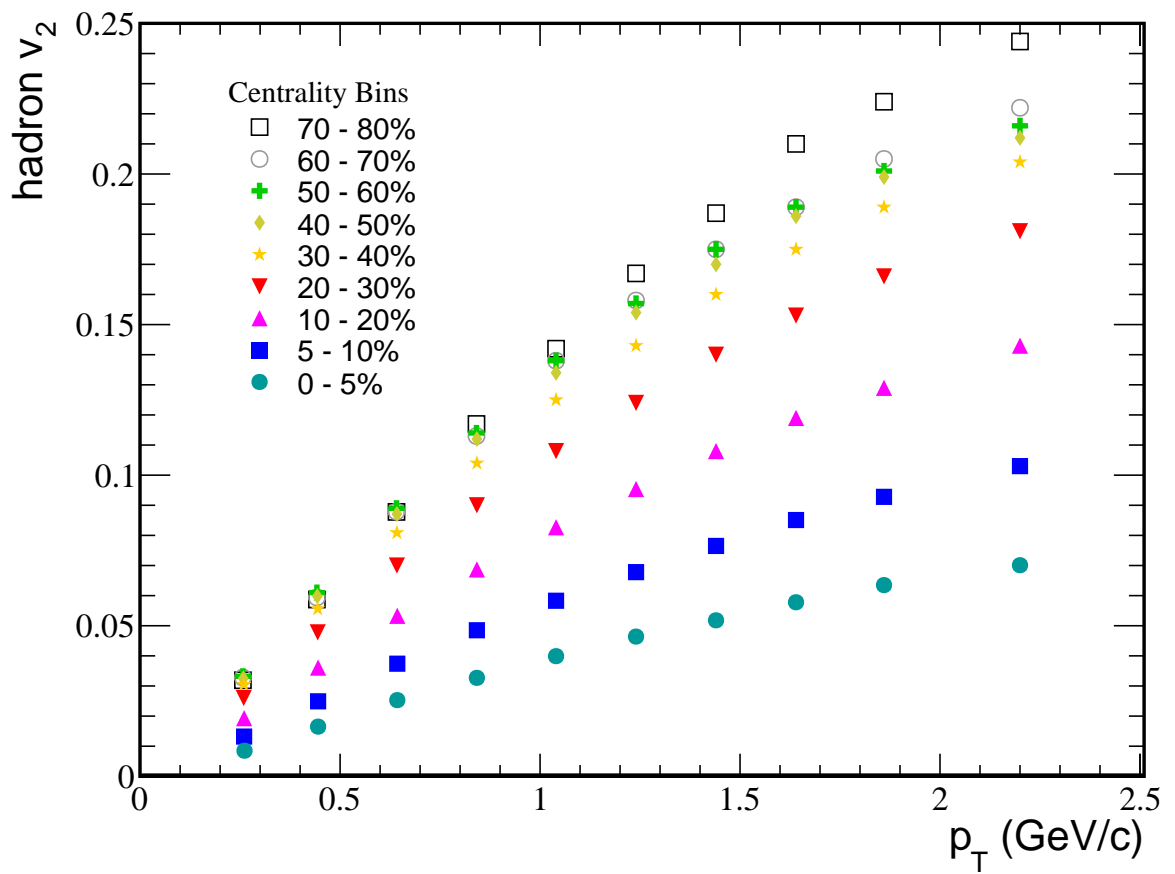


Figure 4.3: Measured  $v_2$  values for hadrons across a range of  $p_T$  and centralities.

also have large elliptic flow. Because of limited statistics electron  $v_2$  is measured in much larger  $p_T$  and centrality bins. Various measurements of NPE  $v_2$  are seen in Figure 4.4, showing that they tend to fall in a range between .05 and .15 depending on the measurement procedure. For this analysis we assume that NPE  $v_2$  is .1 in all bins, we then vary the NPE  $v_2$  between .05 and .15 and take the difference in final correlations as a systematic error.

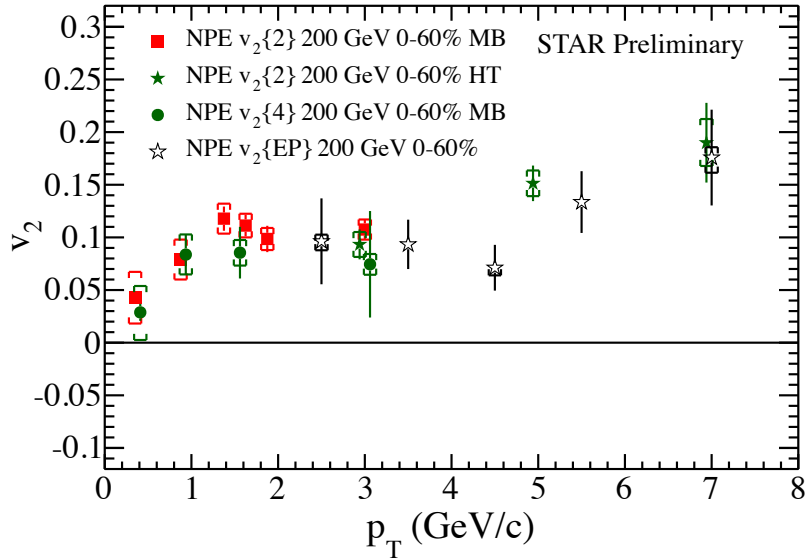


Figure 4.4: Various measurements of NPE  $v_2$  in STAR. Going forward we assume .1 to be the value for NPE  $v_2$  in all bins.

### 4.3.2 Background Normalization

Knowing the values of  $v_2$  for hadrons and non-photonic electrons, we then need to determine the overall normalization constant  $B$  as in Equation 4.1. There are two simple ways of estimating this, both relying on the assumption that the jet like contributions to the azimuthal correlation are concentrated in peaks around 0 and  $\pi$ , and that any remaining correlations there are the result of the underlying  $v_2$  background.

In one case we can simply pick a point between the near and away sides and then set  $B$  so that the overall yield of particles above background at that point is 0. This point is typically taken to be around 1 radian and thus this method is called the zero yield at 1 (ZYA1) normalization. Although when we implement ZYA1 normalization we take the lowest absolute yield of the 3 points closest to 1 radian. Alternatively we can instead pick the point in the raw correlation with lowest value and normalize so that that point produces zero yield. This is the zero yield at minimum (ZYAM) method. These methods tend to coincide in practice and unless otherwise noted we use ZYAM normalization. There is another technique called absolute background subtraction used by PHENIX in their NPE-hadron correlation measurement but we do not use this method.

When using ZYAM or ZYA1 normalization our background subtracted yield can be very susceptible to downward fluctuations of points causing an abnormally high yield. To account for this we also look at the effect of normalizing to the next highest point in the correlation. We then compare the values of  $B$  that we get and then quote the difference as the systematic error of background normalization.

## 4.4 Correlations in Au+Au

We will now look at putting together the results of the previous sections and creating the NPE-h correlation in Au+Au collisions. We will then discuss the results in Au+Au before moving on to p+p and event plane dependent correlations.

### 4.4.1 Associated Hadrons

The basic quantity we will measure is the yield  $\frac{dN}{d\Delta\phi}$  of associated hadrons at various relative to some triggered electron. For the associated hadrons the cuts we use are summarized in Table 4.1.

The correlations are further broken up into bins in event centrality and asso-

Variable	Cut
Track Type	< .5 (Primary)
Global DCA	< 2.0cm
$\eta$	$\in (-1.0, 1.0)$
$p_T$	$\geq .2$ GeV

Table 4.1: Cuts for associated hadrons used in e-h correlations

ciated hadron  $p_T$ . This is the point at which we apply the acceptance corrections from the single particle  $\phi$  weighting as well as the mixed event weighting. Additionaly we also correct the yield for the efficiency of the associated hadron yield. The TPC efficiency is lower for the high occupancy events in central collisions, and efficiency is also significantly worse for very low  $p_T$  hadrons. The efficiency is calculated from embedding and the results are summarized in Figure 4.5.

#### 4.4.2 Constructing the NPE-hadron correlation

Now with azimuthal electron-hadron correlation functions we look at how we create the NPE-h correlation. The definition of the NPE-h correlation is:

$$\frac{dN_{NPE-h}}{d\Delta\phi} = \frac{dN_{semi-h}}{d\Delta\phi} - \left(\frac{1}{\epsilon_\gamma} - 1\right) \frac{dN_{photonic-h}}{d\Delta\phi} + \frac{dN_{same-h}}{d\Delta\phi} \quad (4.2)$$

An explanation of these terms:

- **Semi-inclusive electrons:** This is the correlation of inclusive electrons for which no photonic partner track could be found. This sample will include many non-photonic electrons as well as some photonic background for which we could not find a partner track.
- **Unidentified photonic electrons:** the term:

$$\left(\frac{1}{\epsilon_\gamma} - 1\right) \frac{dN_{photonic-h}}{d\Delta\phi}$$

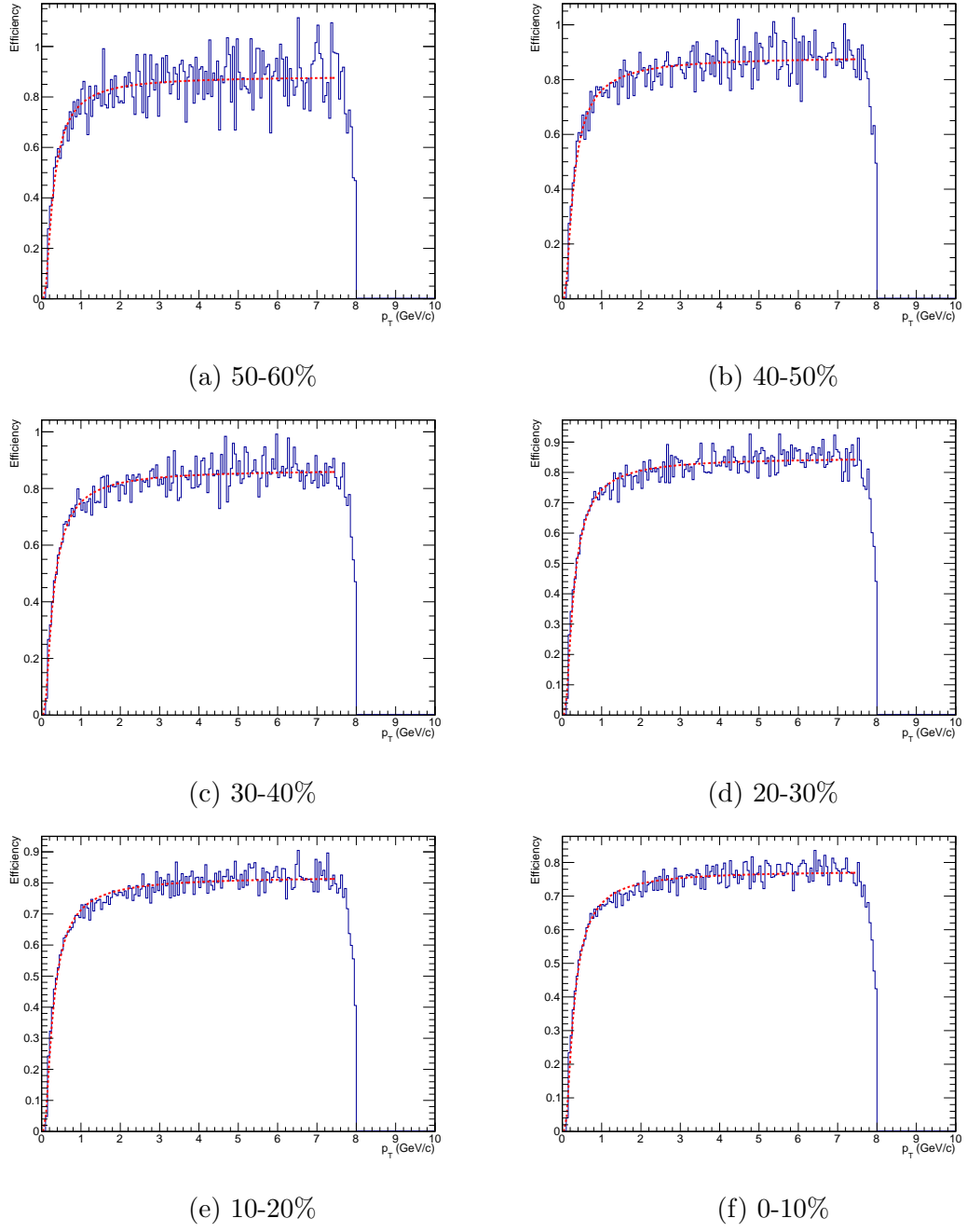


Figure 4.5: The TPC efficiency for hadrons as a function of hadron  $p_T$ . The different plots are for different centralities which correspond to 0-10%, 10-20%, 20-30%, 30-40%, 40-50%, and 50-60%.

is intended to remove the remaining photonic background triggers from the semi-inclusive sample. To do this we take the correlation for identified photonic electrons to hadrons and scale it up according to the estimated photonic electrons reconstruction efficiency,  $\epsilon_\gamma$ . The reconstruction efficiency is determined by embedding simulations.

- **Same-sign electrons:** The method for identifying photonic electrons, pairing all tracks and calculating DCAs and invariant masses, will result in some oversubtraction of NPE signal. We account for the combinatorially removed points by looking at the results of same sign pairing tracks, i.e. the tracks which pass all of the photonic partner cuts except that they have the same sign. We add this term back make up for the NPE signal which was removed by the previous two terms.

There is also the potential for contamination of the triggered electrons with hadrons. This would require the subtraction of a dihadron correlation term:

$$\frac{dN_{h-h}}{d\Delta\phi}$$

We expect the purity of our triggered electrons to be high in the relevant  $p_T$  ranges so for this analysis we will not include it.

#### 4.4.3 Raw Correlations

The raw correlation is the distribution  $\frac{dN_{NPE-h}}{d\Delta\phi}$  before we subtract the background from  $v_2$ . The subtraction and correction spelled out in Equation 4.2 has already been performed and what is shown in the following figures is the NPE-h correlation with no background subtraction. The raw correlations serve as an initial check of the correlation method to spot any problems with our procedure.

Figures 4.6, 4.7 and 4.8 show the raw correlations in 200 GeV AuAu collisions and that they conform to our rough expectations. Overall particle yields are

also higher at lower  $p_T$  and are much higher in central events where multiplicity is higher. The general trend is for particle yields to be higher around 0 angle relative to the triggered NPE and at  $\pi$ , this is normal dijet distribution which is seen in hard processes. We also see that these dijets sit on top of a modulated background from  $v_2$ . We can see that the calculated backgrounds are reasonable and we also get a sense of the performance and limitations of the ZYAM method. For example in Figure 4.8a we see that a low fluctuation in one bin may have pulled down the normalization causing the near side peak to sit farther above the background. We will account for these types when we estimate the systematic uncertainties.

#### 4.4.4 Subtracted Distributions and Yields

We now want to look at how the jet-like distributions of particles changes as a function of collision centrality and trigger particle  $p_T$ . We subtract off the background from the underlying event and  $v_2$  to examine effects of the heavy quark fragmentation and propagation through the medium. The subtracted plots are summarized in Figures 4.9, 4.10and 4.11.

For these NPE-h correlations we also consider three sources of systematic error: Uncertainty from NPE  $v_2$ , uncertainty in photonic electron reconstruction efficiency, and background normalization. Results NPE  $v_2$  are over wide ranges in  $p_T$  and centrality and are roughly around .1 we take that value when calculating the background but we also calculate backgrounds with  $v_2$  of .05 and .15. We then take the difference between these extremes as the uncertainty.

The photonic electron reconstruction efficiency ( $\epsilon_\gamma$ ) is determined from embedding simulations but the extracted values tend to vary from analysis to analysis. To be safe we allow the efficiency to vary by 10% and then take the difference in distributions as the error. This is done point by point. The combined NPE  $v_2$

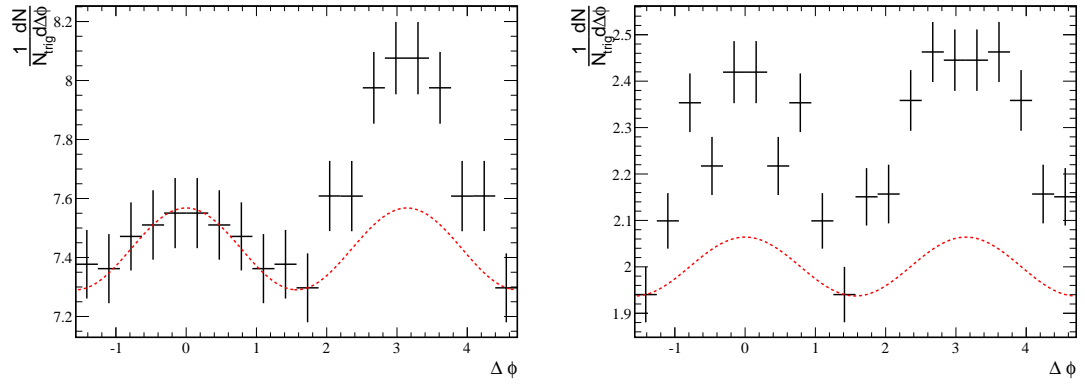
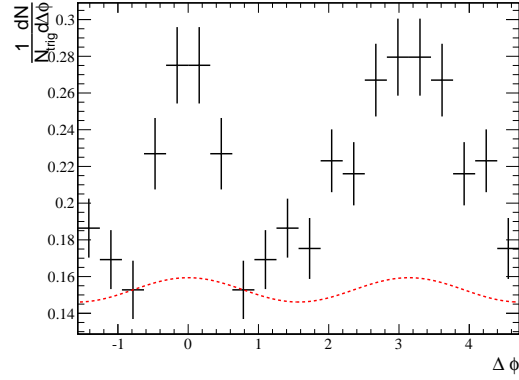
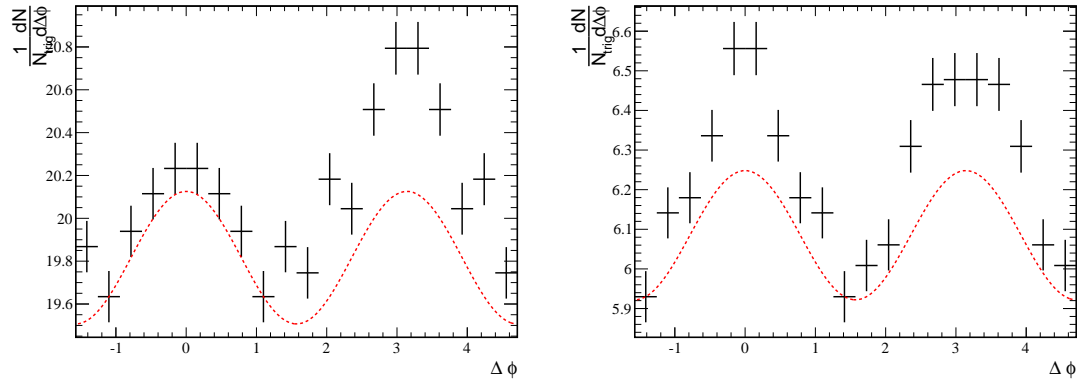
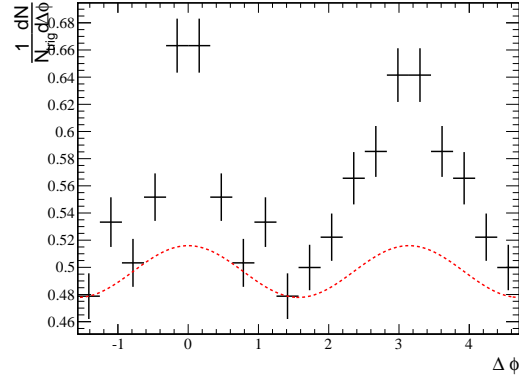
(a)  $.5 \text{ GeV}/c \leq p_{T,h} \leq 1.0 \text{ GeV}/c$ (b)  $1.0 \text{ GeV}/c \leq p_{T,h} \leq 2.0 \text{ GeV}/c$ (c)  $2.0 \text{ GeV}/c \leq p_{T,h} \leq 4.0 \text{ GeV}/c$ 

Figure 4.6: Raw NPE-h Correlations for 40-60% centrality events. Trigger  $p_T$  is  $4.0 \text{ GeV}/c \leq p_{T,trig} \leq 6.0 \text{ GeV}/c$



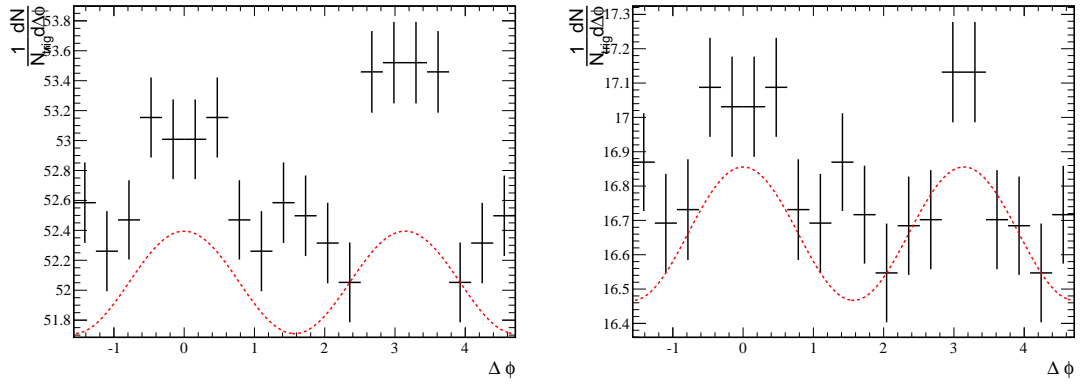
(a)  $.5 \text{ GeV}/c \leq p_{T,h} \leq 1.0 \text{ GeV}/c$

(b)  $1.0 \text{ GeV}/c \leq p_{T,h} \leq 2.0 \text{ GeV}/c$



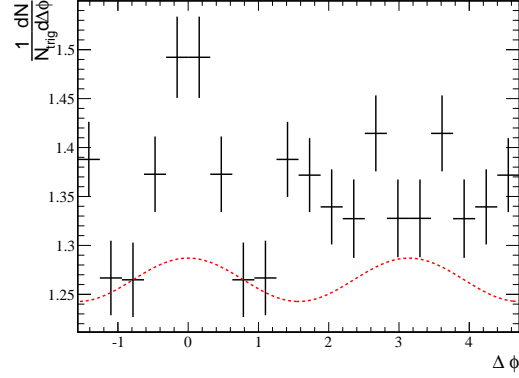
(c)  $2.0 \text{ GeV}/c \leq p_{T,h} \leq 4.0 \text{ GeV}/c$

Figure 4.7: Raw NPE-h Correlations for 20-40% centrality events. Trigger  $p_T$  is  $4.0 \text{ GeV}/c \leq p_{T,trig} \leq 6.0 \text{ GeV}/c$



(a)  $.5 \text{ GeV}/c \leq p_{T,h} \leq 1.0 \text{ GeV}/c$

(b)  $1.0 \text{ GeV}/c \leq p_{T,h} \leq 2.0 \text{ GeV}/c$



(c)  $2.0 \text{ GeV}/c \leq p_{T,h} \leq 4.0 \text{ GeV}/c$

Figure 4.8: Raw NPE-h Correlations for 0-10% centrality events. Trigger  $p_T$  is  $4.0 \text{ GeV}/c \leq p_{T,trig} \leq 6.0 \text{ GeV}/c$

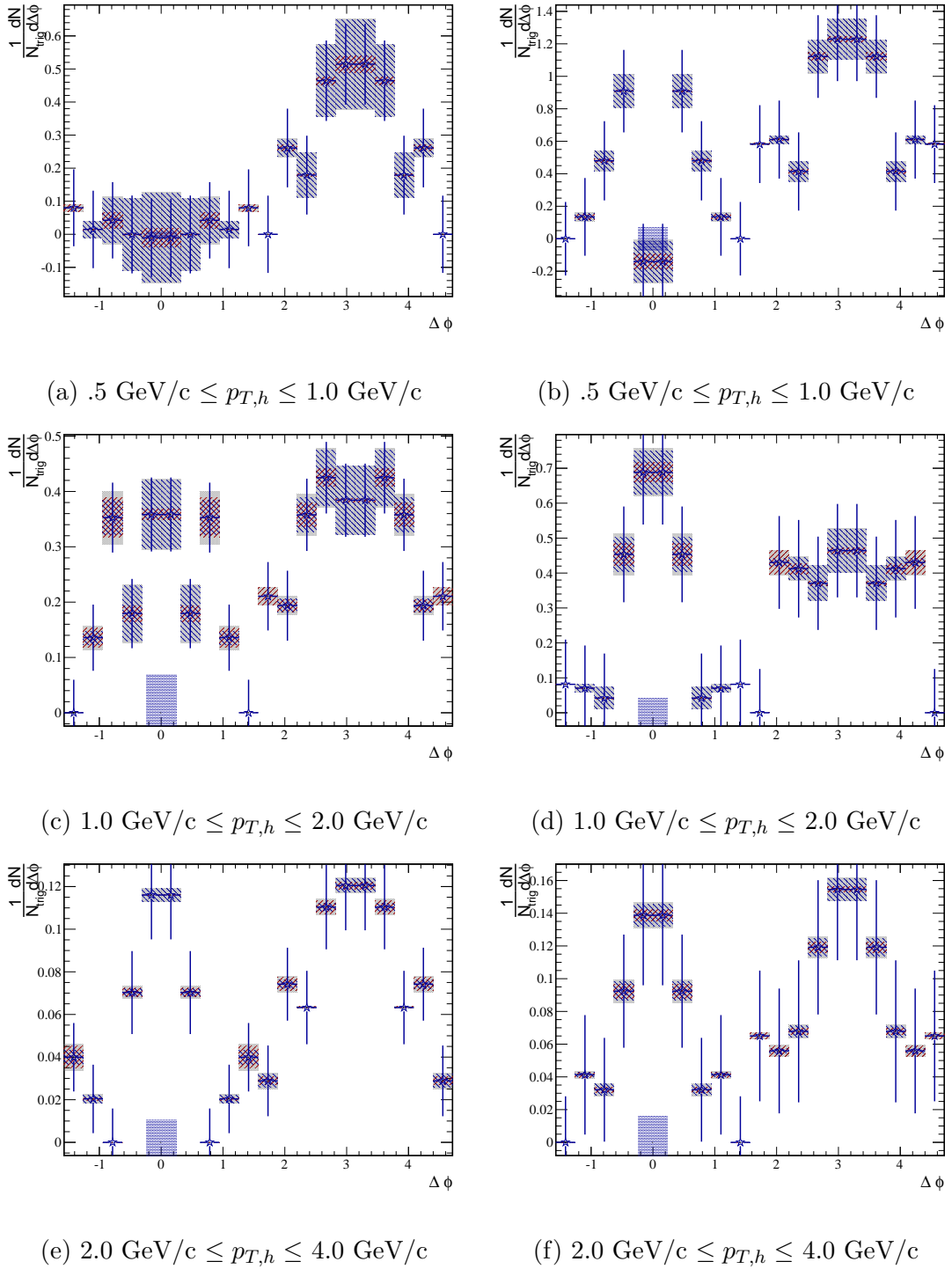


Figure 4.9: Background subtracted NPE-h correlations for 40-60% centrality events. Trigger  $p_T$  is  $4.0 \text{ GeV/c} \leq p_{T,\text{trig}} \leq 6.0 \text{ GeV/c}$

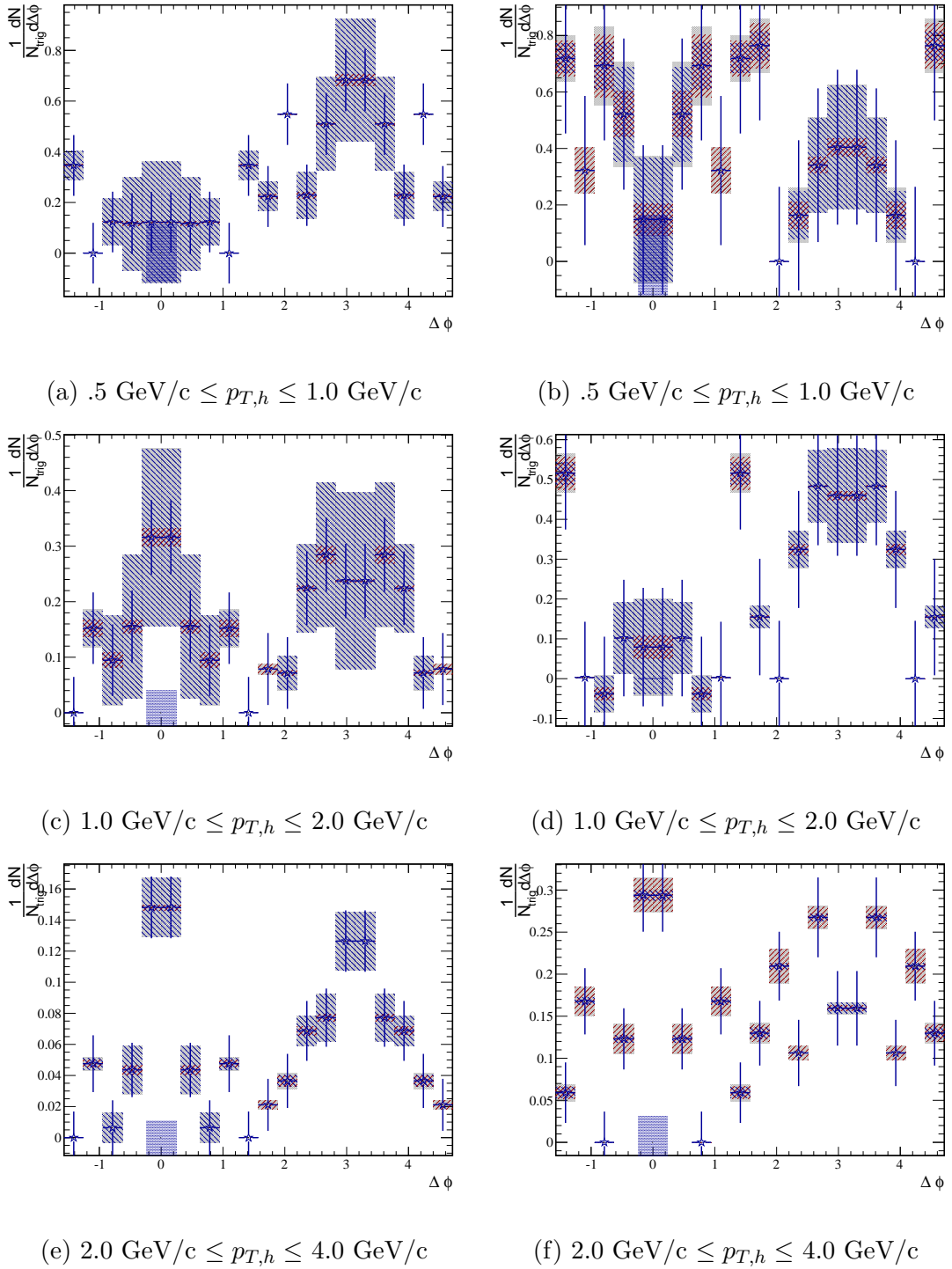


Figure 4.10: Background subtracted NPE-h correlations for 20-40% centrality events. Trigger  $p_T$  is  $4.0 \text{ GeV/c} \leq p_{T,\text{trig}} \leq 6.0 \text{ GeV/c}$

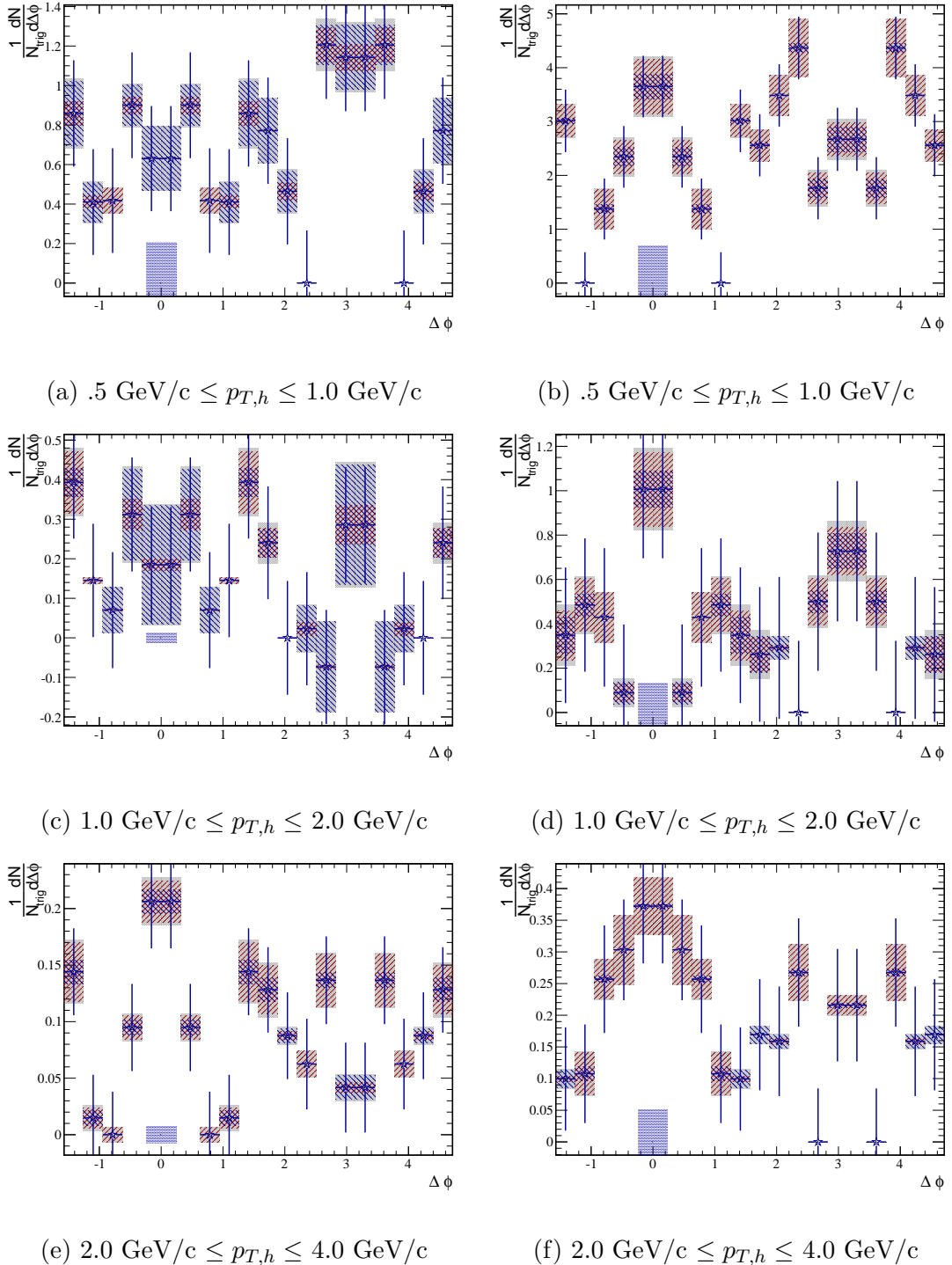


Figure 4.11: Background subtracted NPE-h correlations for 0-10% centrality events. Trigger  $p_T$  is  $4.0 \text{ GeV}/c \leq p_{T,\text{trig}} \leq 6.0 \text{ GeV}/c$

Associated $p_T$	$\Delta\phi$ region	Yield $\frac{1}{N_{trig}\Delta\phi}$	Stat. Error	Sys. Error
$p_{T,asso} \in (.5, 1.0)$ GeV/c	Near-side	0.0143632	0.0737196	0.0599507
$p_{T,asso} \in (.5, 1.0)$ GeV/c	Head	0.363855	0.0659528	0.0589941
$p_{T,asso} \in (.5, 1.0)$ GeV/c	Shoulder	0.107132	0.063884	0.00917141
$p_{T,asso} \in (1.0, 2.0)$ GeV/c	Near-side	0.322385	0.0396921	0.030521
$p_{T,asso} \in (1.0, 2.0)$ GeV/c	Head	0.366602	0.0355859	0.0283117
$p_{T,asso} \in (1.0, 2.0)$ GeV/c	Shoulder	0.126959	0.0335234	0.00708298
$p_{T,asso} \in (2.0, 4.0)$ GeV/c	Near-side	0.0649261	0.0114213	0.00148537
$p_{T,asso} \in (2.0, 4.0)$ GeV/c	Head	0.0923857	0.0105544	0.00160527
$p_{T,asso} \in (2.0, 4.0)$ GeV/c	Shoulder	0.0449183	0.00902871	0.00252461

Table 4.2: Yields and Errors from NPE-h correlations in 40-60% central Au+Au collisions with trigger  $4.0\text{GeV}/c \leq p_t \leq 6.0\text{ GeV}/c$ .

and  $\epsilon_\gamma$  systematics are represented on the plots by the shaded region around the points. The NPE  $v_2$  error tends to be the dominant source of uncertainty and the systematics are much larger for lower associated hadron  $p_T$ .

The systematic uncertainty from background normalization is calculated by performing the ZYAM procedure on the two lowest points in the correlation. The difference in normalization factors is taken as the uncertainty and we display this as a shaded bar at 0 yield and 0 angle. This uncertainty would move all points together in a uniform manner.

The subtracted distributions give some insight into the interactions of heavy quarks with the QGP medium. For all trigger  $p_T$  shown the direction of trigger electron is well correlated to the direction of the parent B or D meson. Thus we look to the near and away side yields for clues to the nature of the initially created heavy quarks interactions. We calculate the background subtracted yield for the near side region  $\Delta\phi \leq .942$ , in the away side “head”  $\Delta\phi \geq 2.2$ , and in

Associated $p_T$	$\Delta\phi$ region	Yield $\frac{1}{N_{trig}\Delta\phi}$	Stat. Error	Sys. Error
$p_{T,asso} \in (.5, 1.0)$ GeV/c	Near-side	0.43422	0.152473	0.0568138
$p_{T,asso} \in (.5, 1.0)$ GeV/c	Head	0.868317	0.136648	0.0549569
$p_{T,asso} \in (.5, 1.0)$ GeV/c	Shoulder	0.37479	0.128162	0.00797441
$p_{T,asso} \in (1.0, 2.0)$ GeV/c	Near-side	0.39401	0.0845325	0.0303613
$p_{T,asso} \in (1.0, 2.0)$ GeV/c	Head	0.391791	0.0738275	0.0275223
$p_{T,asso} \in (1.0, 2.0)$ GeV/c	Shoulder	0.160784	0.0700681	0.0111099
$p_{T,asso} \in (2.0, 4.0)$ GeV/c	Near-side	0.0956762	0.0230099	0.00354069
$p_{T,asso} \in (2.0, 4.0)$ GeV/c	Head	0.107273	0.0231531	0.00321996
$p_{T,asso} \in (2.0, 4.0)$ GeV/c	Shoulder	0.0379724	0.0194678	0.00122931

Table 4.3: Yields and Errors from NPE-h correlations in 40-60% central Au+Au collisions with trigger  $6.0\text{GeV}/c \leq p_t \leq 9.0\text{ GeV}/c$ .

Associated $p_T$	$\Delta\phi$ region	Yield $\frac{1}{N_{trig}\Delta\phi}$	Stat. Error	Sys. Error
$p_{T,asso} \in (.5, 1.0)$ GeV/c	Near-side	0.113593	0.0752799	0.0993901
$p_{T,asso} \in (.5, 1.0)$ GeV/c	Head	0.446483	0.0664356	0.0996666
$p_{T,asso} \in (.5, 1.0)$ GeV/c	Shoulder	0.351208	0.0655682	0.0254741
$p_{T,asso} \in (1.0, 2.0)$ GeV/c	Near-side	0.225576	0.0410495	0.0702893
$p_{T,asso} \in (1.0, 2.0)$ GeV/c	Head	0.234525	0.0363017	0.0692495
$p_{T,asso} \in (1.0, 2.0)$ GeV/c	Shoulder	0.0472435	0.035183	0.0101302
$p_{T,asso} \in (2.0, 4.0)$ GeV/c	Near-side	0.0771784	0.0115255	0.00835489
$p_{T,asso} \in (2.0, 4.0)$ GeV/c	Head	0.0855548	0.0104771	0.00824166
$p_{T,asso} \in (2.0, 4.0)$ GeV/c	Shoulder	0.0180967	0.00924105	0.0017841

Table 4.4: Yields and Errors from NPE-h correlations in 20-40% central Au+Au collisions with trigger  $4.0\text{GeV}/c \leq p_t \leq 6.0\text{ GeV}/c$ .

Associated $p_T$	$\Delta\phi$ region	Yield $\frac{1}{N_{trig}\Delta\phi}$	Stat. Error	Sys. Error
$p_{T,asso} \in (.5, 1.0)$ GeV/c	Near-side	0.529239	0.16639	0.104476
$p_{T,asso} \in (.5, 1.0)$ GeV/c	Head	0.285343	0.147377	0.0922544
$p_{T,asso} \in (.5, 1.0)$ GeV/c	Shoulder	0.465791	0.144077	0.0391084
$p_{T,asso} \in (1.0, 2.0)$ GeV/c	Near-side	0.0457684	0.0909543	0.0497525
$p_{T,asso} \in (1.0, 2.0)$ GeV/c	Head	0.398024	0.0809105	0.0490142
$p_{T,asso} \in (1.0, 2.0)$ GeV/c	Shoulder	0.21068	0.0785307	0.0177771
$p_{T,asso} \in (2.0, 4.0)$ GeV/c	Near-side	0.183656	0.0245176	0.0100624
$p_{T,asso} \in (2.0, 4.0)$ GeV/c	Head	0.1675	0.0238689	0.00546355
$p_{T,asso} \in (2.0, 4.0)$ GeV/c	Shoulder	0.125145	0.0209576	0.00807931

Table 4.5: Yields and Errors from NPE-h correlations in 20-40% central Au+Au collisions with trigger  $6.0\text{GeV}/c \leq p_t \leq 9.0\text{ GeV}/c$ .

Associated $p_T$	$\Delta\phi$ region	Yield $\frac{1}{N_{trig}\Delta\phi}$	Stat. Error	Sys. Error
$p_{T,asso} \in (.5, 1.0)$ GeV/c	Near-side	0.74085	0.167485	0.0727868
$p_{T,asso} \in (.5, 1.0)$ GeV/c	Head	0.737388	0.147269	0.0693534
$p_{T,asso} \in (.5, 1.0)$ GeV/c	Shoulder	0.658026	0.146362	0.0826822
$p_{T,asso} \in (1.0, 2.0)$ GeV/c	Near-side	0.223651	0.0911303	0.0636431
$p_{T,asso} \in (1.0, 2.0)$ GeV/c	Head	0.0738618	0.078665	0.0643826
$p_{T,asso} \in (1.0, 2.0)$ GeV/c	Shoulder	0.199047	0.0777526	0.0314492
$p_{T,asso} \in (2.0, 4.0)$ GeV/c	Near-side	0.0992778	0.0245557	0.0086265
$p_{T,asso} \in (2.0, 4.0)$ GeV/c	Head	0.0756338	0.0215144	0.00918282
$p_{T,asso} \in (2.0, 4.0)$ GeV/c	Shoulder	0.112994	0.0207828	0.0118356

Table 4.6: Yields and Errors from NPE-h correlations in 0-10% central Au+Au collisions with trigger  $4.0\text{GeV}/c \leq p_t \leq 6.0\text{ GeV}/c$ .

Associated $p_T$	$\Delta\phi$ region	Yield $\frac{1}{N_{trig}\Delta\phi}$	Stat. Error	Sys. Error
$p_{T,asso} \in (.5, 1.0)$ GeV/c	Near-side	2.31516	0.358503	0.238676
$p_{T,asso} \in (.5, 1.0)$ GeV/c	Head	2.76404	0.316466	0.233436
$p_{T,asso} \in (.5, 1.0)$ GeV/c	Shoulder	2.84518	0.315039	0.180387
$p_{T,asso} \in (1.0, 2.0)$ GeV/c	Near-side	0.631058	0.193553	0.0816061
$p_{T,asso} \in (1.0, 2.0)$ GeV/c	Head	0.385498	0.172518	0.0558037
$p_{T,asso} \in (1.0, 2.0)$ GeV/c	Shoulder	0.283197	0.168621	0.0576901
$p_{T,asso} \in (2.0, 4.0)$ GeV/c	Near-side	0.326725	0.052348	0.0266922
$p_{T,asso} \in (2.0, 4.0)$ GeV/c	Head	0.151844	0.0469381	0.0147477
$p_{T,asso} \in (2.0, 4.0)$ GeV/c	Shoulder	0.134278	0.0464204	0.00730969

Table 4.7: Yields and Errors from NPE-h correlations in 0-10% central Au+Au collisions with trigger  $6.0\text{GeV}/c \leq p_t \leq 9.0\text{ GeV}/c$ .

the away side shoulder  $1.25 \leq \Delta\phi \leq 2.2$ . For the separated shoulder and head regions we are looking for signs of away side broadening in the correlation. We might expect to find that the ratio of the shoulder to head yields is larger in more central collisions as a result of jets being diverted or smeared out as a result of interactions with the QGP. We can also look for evidence of medium responses to a heavy quark traversing it. The yields from these plots are listed in Table AAA. We will summarize these results once we have the correlations from p+p as well.

## 4.5 Correlations in p+p

With correlations from Au+Au collisions we can study the effects on observed particles resulting from heavy quark interactions with the medium. By looking across centralities we can select different fireball sizes and durations to see how the presence of QGP affects the formation of dijets. Now we can also look at p+p collisions also at  $\sqrt{s_{NN}} = 200$  GeV to see the correlation without any QGP and

use this as a baseline for comparison with our Au+Au results.

NPE-h correlations have also been used to study the charm to bottom produced in these collisions. This is done by fitting the observed correlations to Pythia simulations of NPE-h correlations from charm and bottom decays. Those resulting from bottom will have a broader distribution because of the higher mass of the  $B$  mesons compared to  $D$ . We will show a calculation of this as a consistency check with previous NPE-h analyses.

#### 4.5.1 Data and Correlations

The dataset for the p+p correlations is the BHT triggered events in STAR run 12 p+p 200 GeV. The procedure for identifying non-photonic electrons and constructing the NPE-h correlation is nearly identical to Au+Au. We still need to perform the acceptance corrections as in Au+Au, however because of the lower multiplicities in p+p collisions it is difficult to get enough statistics for mixed event correlations so we will rely only on the single particle  $\phi$  weighting. In run 12 the TPC performed much better and has a more uniform acceptance than in run 11 so practically these corrections are far less important.

In p+p correlations there is no need to perform the background subtraction as in Equation 4.1 since there is no elliptic flow in p+p collisions. So we no longer need to consider raw correlations, we can just take the results from Equation 4.2 and use those as our correlations. Since there is no NPE-h  $v_2$  and no need to normalize to some background distribution we no longer have to consider 2 of the 3 sources of systematic uncertainty present in Au+Au. We only need to account for uncertainty in  $\epsilon_\gamma$ , the photonic electron reconstruction efficiency. We do this as in Au+Au collisions, allowing the efficiency to vary by 10%. Tables 4.8 4.9 summarize the yields with errors obtained from p+p collisions.

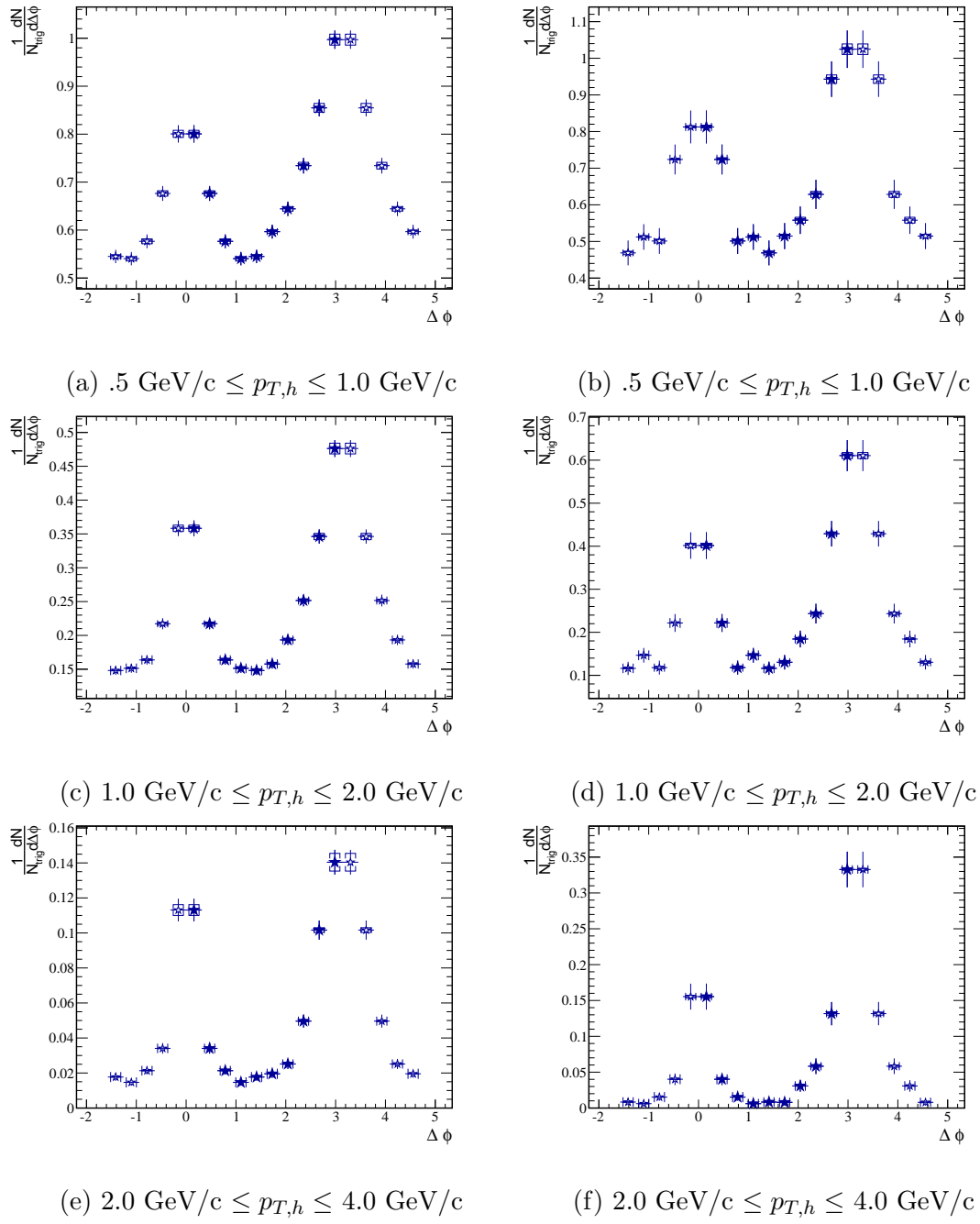


Figure 4.12: NPE-h correlations for p+p collisions at 200 GeV left column shows triggers with  $4.0 \text{ GeV}/c \leq p_T \leq 6.0 \text{ GeV}/c$  and right column is  $6.0 \text{ GeV}/c \leq p_T \leq 9.0 \text{ GeV}/c$ .

Associated $p_T$	$\Delta\phi$ region	Yield $\frac{1}{N_{trig}\Delta\phi}$	Stat. Error	Sys. Error
$p_{T,asso} \in (.5, 1.0)$ GeV/c	Near-side	0.814888	0.00977926	0.00360017
$p_{T,asso} \in (.5, 1.0)$ GeV/c	Head	0.812439	0.00965688	0.00511522
$p_{T,asso} \in (.5, 1.0)$ GeV/c	Shoulder	0.561056	0.00786714	0.00216749
$p_{T,asso} \in (1.0, 2.0)$ GeV/c	Near-side	0.279777	0.00536135	0.00167489
$p_{T,asso} \in (1.0, 2.0)$ GeV/c	Head	0.337404	0.00580794	0.00293765
$p_{T,asso} \in (1.0, 2.0)$ GeV/c	Shoulder	0.156817	0.00379766	0.000439399
$p_{T,asso} \in (2.0, 4.0)$ GeV/c	Near-side	0.057533	0.00242196	0.00096921
$p_{T,asso} \in (2.0, 4.0)$ GeV/c	Head	0.0916335	0.0030426	0.00164648
$p_{T,asso} \in (2.0, 4.0)$ GeV/c	Shoulder	0.019603	0.00132994	8.75715e-05

Table 4.8: Yields and Errors from NPE-h correlations in p+p collisions with trigger  $4.0\text{GeV}/c \leq p_t \leq 6.0\text{ GeV}/c$ .

Associated $p_T$	$\Delta\phi$ region	Yield $\frac{1}{N_{trig}\Delta\phi}$	Stat. Error	Sys. Error
$p_{T,asso} \in (.5, 1.0)$ GeV/c	Near-side	0.801004	0.0245826	0.00217934
$p_{T,asso} \in (.5, 1.0)$ GeV/c	Head	0.815639	0.025429	0.00632914
$p_{T,asso} \in (.5, 1.0)$ GeV/c	Shoulder	0.48424	0.0194036	0.00332109
$p_{T,asso} \in (1.0, 2.0)$ GeV/c	Near-side	0.278887	0.0138082	0.00181987
$p_{T,asso} \in (1.0, 2.0)$ GeV/c	Head	0.403106	0.0163408	0.00270691
$p_{T,asso} \in (1.0, 2.0)$ GeV/c	Shoulder	0.135421	0.00940179	0.000890293
$p_{T,asso} \in (2.0, 4.0)$ GeV/c	Near-side	0.0681146	0.00652803	0.000581799
$p_{T,asso} \in (2.0, 4.0)$ GeV/c	Head	0.164206	0.00992462	0.000868219
$p_{T,asso} \in (2.0, 4.0)$ GeV/c	Shoulder	0.0147791	0.00321696	0.000280081

Table 4.9: Yields and Errors from NPE-h correlations in p+p collisions with trigger  $6.0\text{GeV}/c \leq p_t \leq 9.0\text{ GeV}/c$ .

### 4.5.2 Charm to Bottom Ratios

We can use the p+p NPE-h correlations to investigate the relative contributions of charm and bottom to non-photonic electrons by fitting the observed correlations with those from  $B$  and  $D$  to find the ratio as a function of electron  $p_T$ . Several experiments have performed this measurement, making this a reasonable check that our method for constructing NPE-h correlations is working as intended.

The simulations are done with Pythia 8.2 with the standard STAR heavy flavor tune. To get reasonable samples across all electron  $p_T$  and to avoid the low  $p_T$  divergence in heavy flavor processes in Pythia we generate the correlations in several bins in  $\text{ptHat}$  and then piece them together according to a weighting, this closely follows the Pythia example `main08.cc`. For  $\text{ptHat} \leq 3.0 \text{ GeV}/c$  we use the “minbias” process `SoftQCD:nonDiffractive = on` for the bins above this we use the hard QCD processes `HardQCD:all = on`. Then to patch the different bins together we scale each bin by the generated cross section, the raw and scaled  $\text{ptHat}$  spectra can be seen in Figure 4.13.

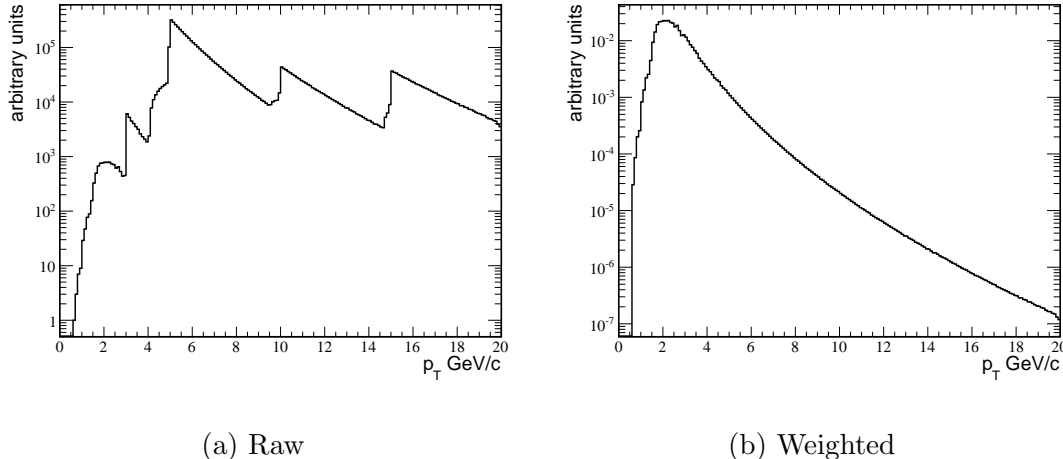


Figure 4.13: The raw and weighted  $\text{ptHat}$  spectra from Pythia.

Then we construct the electron-hadron correlations from the Pythia simulations in two separate cases one for initial  $b$  quarks and one for initial  $c$  quarks. We

check that the final state contains an electron and that the electron has a parent  $B$  or  $D$  meson. To increase statistics, if there is no final state electron we pick on of the heavy mesons, undo and then redo the decay until we get an electron effectively setting the branching ratio for semileptonic decays to 100%. Then we apply acceptance cuts that closely match the STAR acceptance:  $\eta_e \in (-.7, .7)$ ,  $p_{T,e} > 2.0 \text{ GeV/c}$ ,  $\eta_h \in (1.0, 1.0)$ , and  $p_{T,h} > 0.2 \text{ GeV/c}$ . This gives us the electron-hadron correlation that we use in the fit.

For the fit we compare the correlations for  $p_{T,h} > .2 \text{ GeV/c}$  and vary the  $p_T$  of the trigger particle. We fit the correlation with the function:

$$\frac{dN_{NPE-h}}{d\Delta\phi} = r_B f_B(\Delta\phi) + (1 - r_B) f_D(\Delta\phi) \quad (4.3)$$

Where  $f_B$  and  $f_D$  are the correlations for bottom and charm electron-hadron correlations from Pythia, and  $r_B = \frac{e_B}{e_B + e_D}$ . The fit is done in a range around the near side peak  $\Delta\phi < 1.5$  due to difficulties in Pythia accurately recreating away side behavior. Figure 4.14 shows an example fit, plus the correlations from Pythia.

Figure 4.15 shows the results for obtaining  $r_B$  from fits of the p+p correlation plus a comparison to previous published results. Errors are large at high trigger  $p_T$  due to the distributions from  $B$  and  $D$  becoming similar thus reducing the ability to distinguish between the contributions to the overall p+p correlation shape. Discrepancies in the mid  $p_T$  range may be due to difficulties in patching together the `ptHat` bins in the Pythia simulations and this could be fixed by only using `SoftQCD:nonDiffractive` to generate the simulated correlations, but this would be far more time consuming.

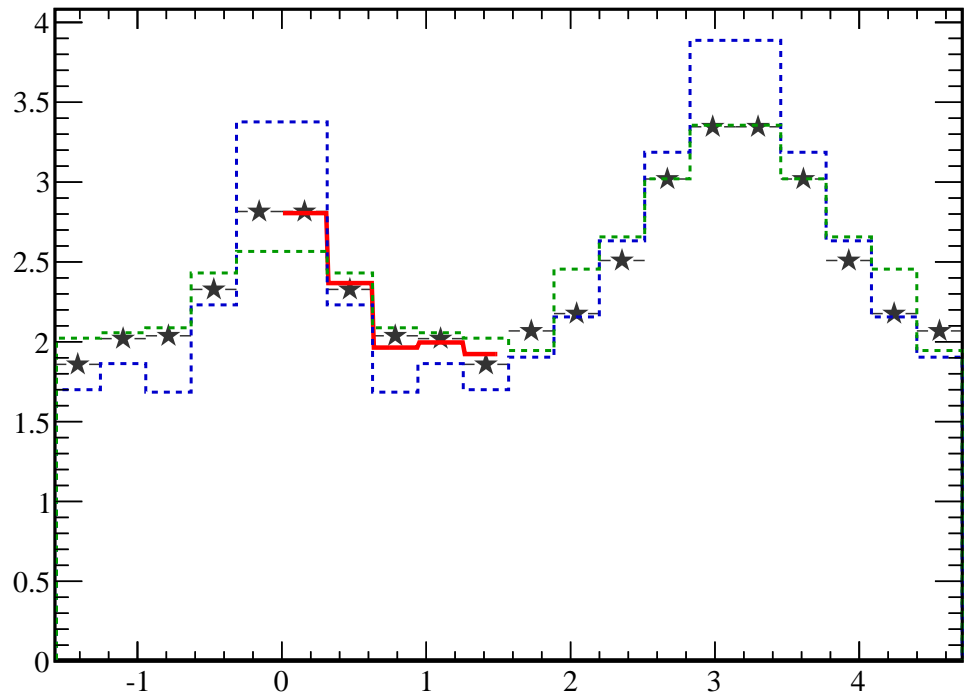


Figure 4.14: NPE-h correlation with  $5.0 \text{ GeV}/c < p_{T,e} < 6.0 \text{ GeV}/c$  and  $p_{T,h} > 0.2 \text{ GeV}/c$ . Pythia distributions are  $f_D(\Delta\phi)$  (blue),  $f_B(\Delta\phi)$  (green), and the distribution with best fit value of  $r_B$  (red).

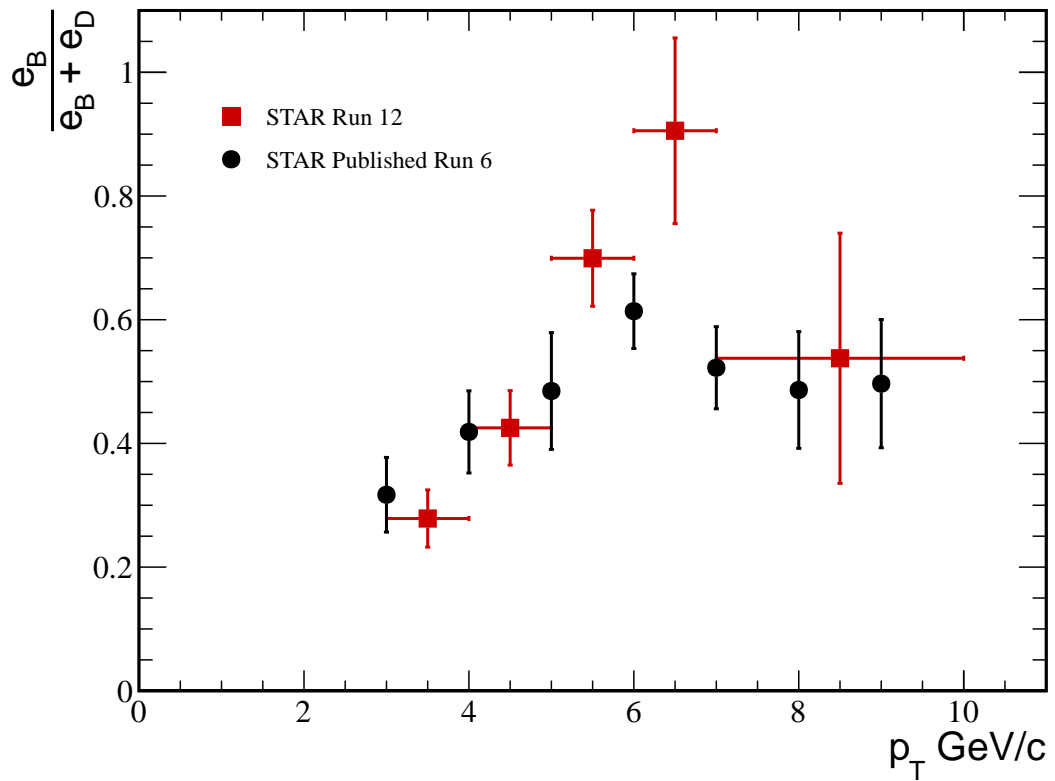


Figure 4.15: Measured value of  $r_B$  as a function of trigger  $p_T$ . Red points are for the current analysis and the black are from STAR published in Ref. Only statistical errors are shown.

## 4.6 Comparisons of Yields

We can use the yields we measured in p+p and Au+Au collisions to look for evidence of jet modification in the medium. To do this we will examine the away side peak shape by comparing the ratio of yields in the shoulder region to the head region (as defined previously). Interactions with the QGP may cause jets to be redirected or smeared out which would manifest as broader away side correlations in Au+Au collisions. We will also look at  $I_{AA}$ , the ratio of the integrated yield in Au+Au to p+p. Suppressions of yields in Au+Au could indicate jet suppression in the medium while increased yields may point to medium responses to the jet.

An important thing to note when comparing the yields from p+p and Au+Au is that we subtracted off a background correlation from Au+Au but performed no such ZYAM procedure for p+p. There is no standard way of accounting for this but we calculate a flat underlying event for p+p (essentially the ZYAM coefficient for background with  $v_2 = 0$ ), use this to estimate the oversubtraction of background in Au+Au and add this back to the Au+Au yields. As seen in Figure 4.12, this is not much of a concern at high associated hadron  $p_T$  but for the lower  $p_T$  bins it has a larger effect.

### 4.6.1 Away Side Shape

We define the yield  $Y$  in a region by:

$$Y(\Delta\phi_1, \Delta\phi_2) = \int_{\Delta\phi_1}^{\Delta\phi_2} \frac{dN_{NPE-h}}{d\Delta\phi} d\Delta\phi \quad (4.4)$$

We define the near side yield as  $Y(0, 2\pi/5)$  the head region as  $Y(7\pi/10, \pi)$ , and the shoulder region as  $Y(2\pi/5, 7\pi/10)$ . To see evidence of jet broadening we compare the yields in the shoulder and head regions. In particular we look at the ratio of the yields  $Y(\text{shoulder})/Y(\text{head})$ . We can see from the p+p data that this ratio tends to be below 1 as the away side peaks are narrow and contain

most of the yield in the region immediately around  $\pi$ . Figure 4.16 shows the the ratios for p+p data as well as Au+Au collisions with 0-10%, 10-40%, and 40-60% centralities. We see that for the most central bins the ratio is larger indicating wider correlations, but the errors on these yields are large. For the other bins, including the p+p data, the ratios seem to follow a similar trend with increasingly narrow correlations at higher hadron  $p_T$ .

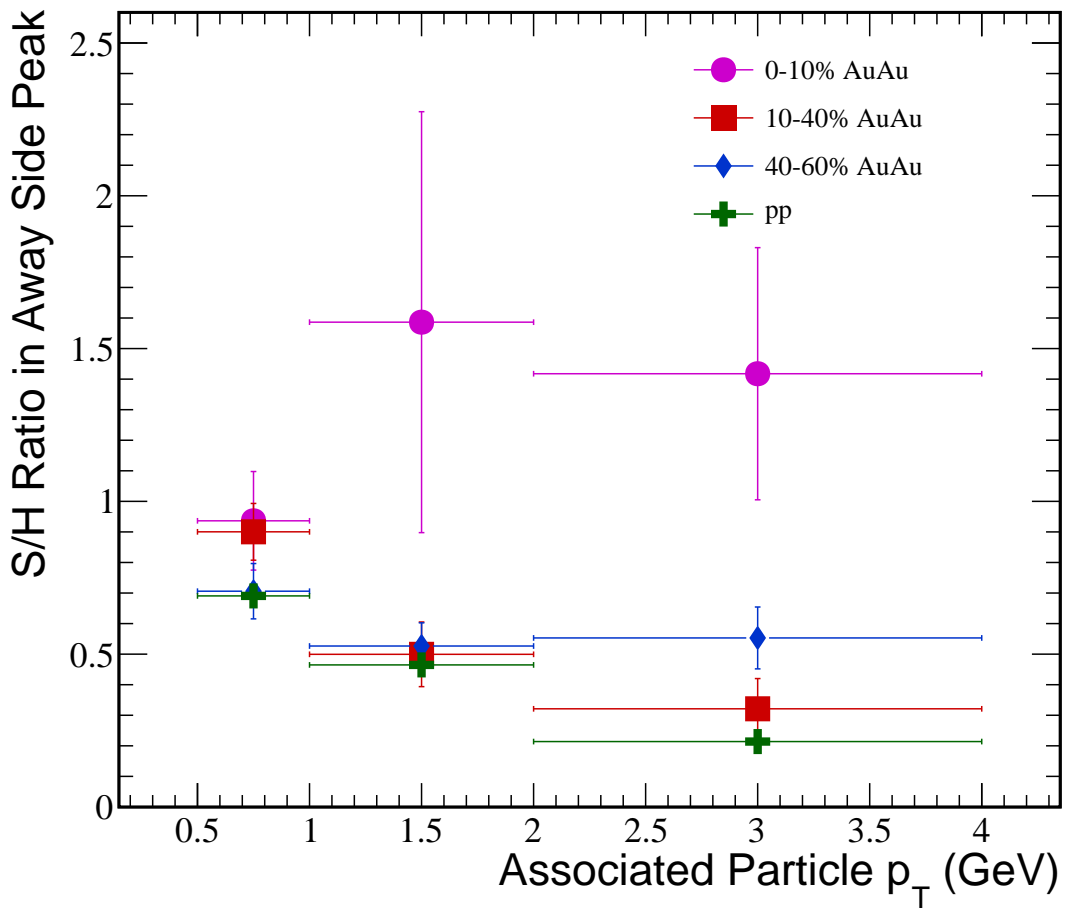


Figure 4.16: Ratio of yields in shoulder region to head region in NPE-h correlations for trigger electrons have  $4.0 \text{ GeV}/c \leq p_T \leq 6.0 \text{ GeV}/c$ . A larger ratio indicates a wider peak.

### 4.6.2 $I_{AA}$

We can also compare the yields in Au+Au collisions to p+p collisions directly to look for jet suppression in heavy flavor correlations. To do this we look at the ratio of yields  $I_{AA}$  defined by:

$$I_{AA} = \frac{Y_{AuAu}(\Delta\phi_1, \Delta\phi_2)}{Y_{pp}(\Delta\phi_1, \Delta\phi_2)} \quad (4.5)$$

$I_{AA}$  serves for jets as a rough analogue of  $R_{AA}$  which is typically used to compare particle spectra between heavy-ion and proton collisions. For identical yields in Au+Au and p+p we would get  $I_{AA} = 1$  and we look for deviations from 1, less than 1 indicating suppressed yield in Au+Au and greater than 1 an enhanced yield.

We measure  $I_{AA}$  for the near side as well as in the away side head region. As explained earlier we estimate the level for the underlying event in p+p and then add this back to the Au+Au data to make up for potential oversubtraction of background with the ZYAM normalization. Figure 4.17 show the near side  $I_{AA}$  and Figure 4.18 the away side. The results are largely inconclusive and it appears that with the errors the results are still largely consistent with 1.

## 4.7 Event-Plane Dependent Correlations

The motivation for measurements of two particle correlations in Au+Au comes from the fact that partons are expected to strongly interact with the color charges present in QGP and that the jet like correlations will depend on the path length traversed by the parton in QGP. Previously we have looked at comparisons between central and peripheral events as well as p+p collisions as a way of investigating the dependence on the presence of QGP. Now we will try to look at a more direct dependence on path length by measuring the correlations relative to

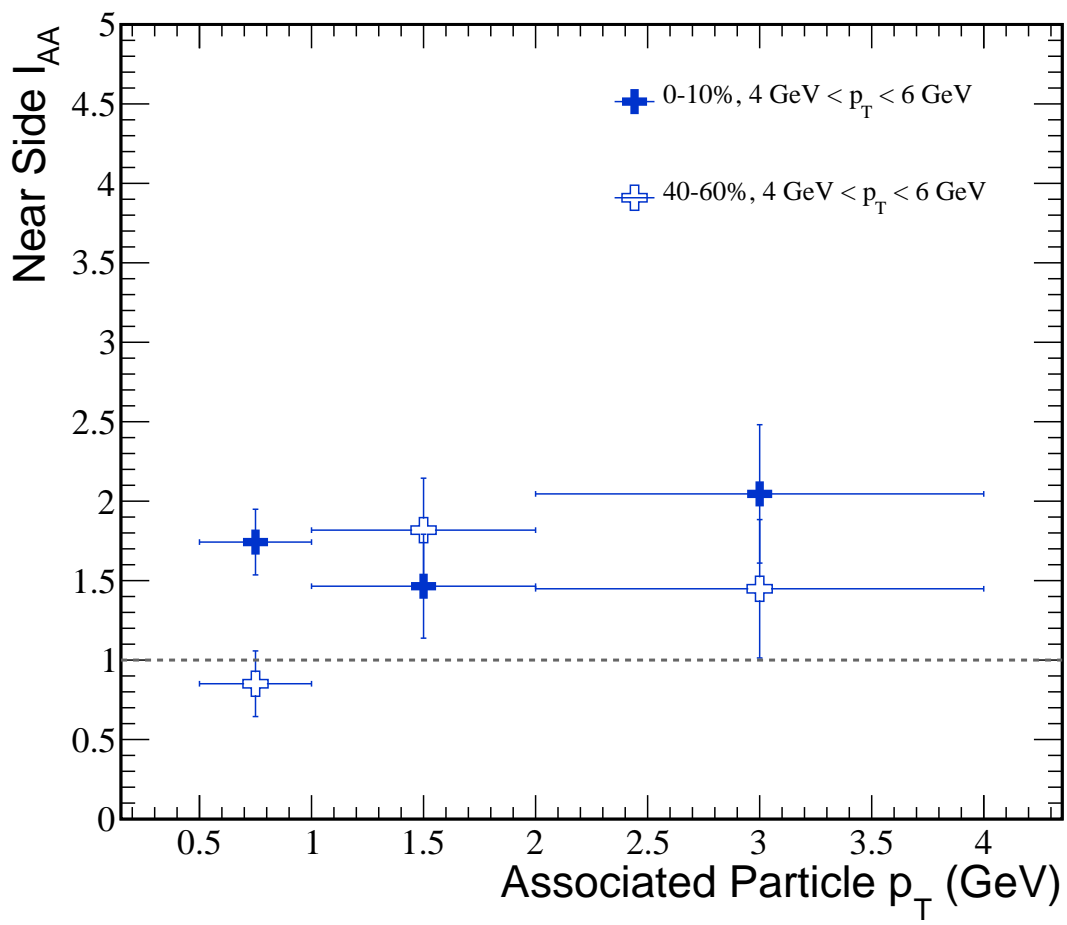


Figure 4.17: Near side

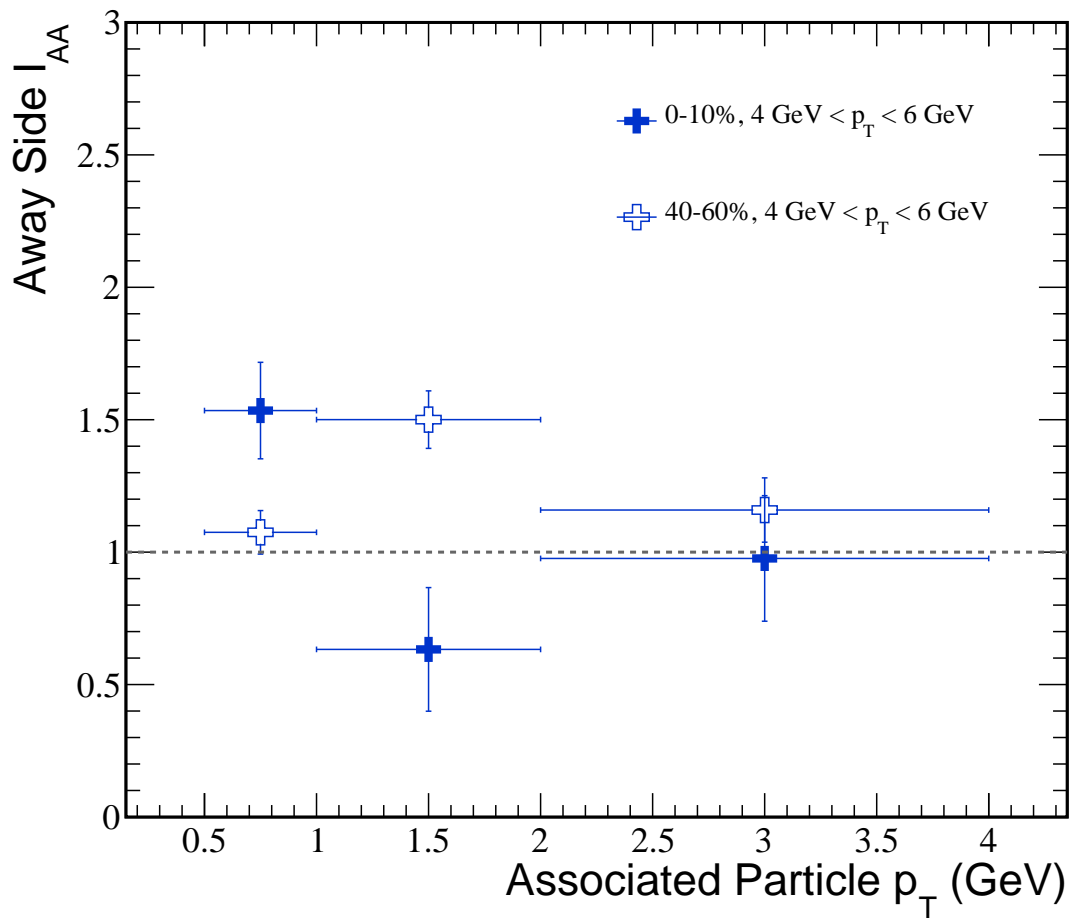


Figure 4.18: Away side

emmision in or out of the event plane.

In non-central Au+Au collisions the collision region formed from the overlap of the two incident nuclei is ellipsoidal. This initial anisotropy in the medium results in elliptic flow,  $v_2$ , and in the final state we observe anisotropic emissions relative to the reaction plane, defined by the momenta of the initial beam particles (see Figure 4.19).

Elliptic flow is defined relative to the reaction plane, however there is no way to experimentally determine the reaction plane in a given event. Instead we use the azimuthal distribution of observed particle to estimate the reaction plane. We get an angle for the estimated reaction plane which we call the event plane. Due to the fact that we calculate the event plane from a finite number of particles we also have some resolution of our event plane angle.

The event plane angle gives us an estimate for the reaction plane angle, we will then look at our trigger particle's angle relative to the event plane. As seen in Figure 4.19 particles traversing the medium perpendicular to the event plane should move through a larger part of the medium. We might guess that out-of-plane correlations show larger away side suppression compared to in-plane, which has already been observed in dihadron correlations. A large portion of our high tower trigger data comes from mid-centralities (30-60% central) which is useful for this analysis since that is where we have the best event plane resolution, but due to higher hadron  $v_2$  this region also has larger systematic uncertainties which may make drawing conclusions difficult.

#### 4.7.1 Event Plane Reconstruction

We use the azimuthal distribution of the particles in an event to calculate the event plane,  $\Psi_{EP}$ . Event planes can be calculated for any order of harmonic in the decomposition of the particle distribution, but since we are interested in  $v_2$  and

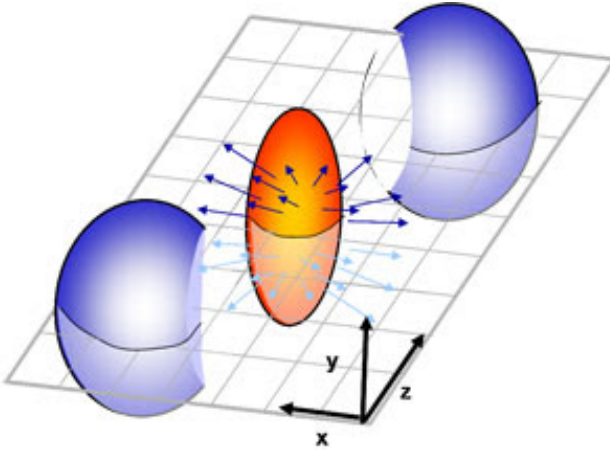


Figure 4.19: Illustration of non-central heavy ion collision and the resulting  $v_2$ . The reaction plane corresponds to the  $xz$ -plane in the diagram.

the second order event plane everything that follows is specifically the  $n = 2$  case. For a more general treatment see ref. First we apply single particle  $\phi$ -weighting to correct for the acceptance of the detector. This is the same procedure as used for the two-particle correlation.

We use the hadrons in the event with  $0.2 \text{ GeV}/c \leq p_T \leq 2.0 \text{ GeV}/c$  in the event plane calculation. Since these events are high tower triggered events there is also a high  $p_T$  leading particle in each event. Since the presence of a jet may bias the calculation of the event plane, we should try to remove this contribution. To do this we exclude the particles in the event with  $|\Delta\eta| < .5$ , where  $\Delta\eta$  is the pseudorapidity difference between the hadron and the leading particle in the event (in events used in NPE analysis this track is usually the electron). This procedure is called the Modified Reaction Plane (MRP) method.

With our sample of hadrons we then construct a flow vector  $\mathbf{Q}$  for the event. The components of this vector are:

$$X = \sum_i w_i \cos(2\phi_i) \quad (4.6)$$

$$Y = \sum_i w_i \sin(2\phi_i) \quad (4.7)$$

where  $w_i$  is some weight given to the particle, in this analysis we use the particle's  $p_T$  as the weight. The second order event plane angle is then given by:

$$\Psi_{EP} = \frac{1}{2} \tan^{-1}\left(\frac{Y}{X}\right) \quad (4.8)$$

The true distribution of the reaction planes should be uniform across all events, however there will still be some distortion in the event plane distribution which we need to correct. To do this we use a shifting method where the harmonics of the uncorrected distribution are used to flatten it. Figure 4.20 shows the distribution of the event plane angle after applying the shifting correction. We see that the resulting distribution is flat to within 1%.

When we calculate the event plane dependent NPE-h correlations we will potentially be correlating the trigger electron with some of the particles used in the event plane calculation. We would like the calculated event plane to be independent of the particles in the correlation so we will actually calculate 5 separate event planes per event. We calculate one for all hadrons in the range  $.2 \text{ GeV}/c \leq p_T \leq 2.0 \text{ GeV}/c$  then we calculate one for each case where the ranges  $.2 \text{ GeV}/c \leq p_T \leq .5 \text{ GeV}/c$ ,  $.5 \text{ GeV}/c \leq p_T \leq 1.0 \text{ GeV}/c$ ,  $1.0 \text{ GeV}/c \leq p_T \leq 1.5 \text{ GeV}/c$ , and  $1.5 \text{ GeV}/c \leq p_T \leq 2.0 \text{ GeV}/c$  are excluded. Each bin with an excluded  $p_T$  range will have a lower resolution due to fewer particles used in the event plane calculation.

Using a finite number of particles to calculate the event plane leaves us with an event plane resolution by which we must scale up our azimuthal anisotropy measurements to get the anisotropy relative to the true reaction plane. This

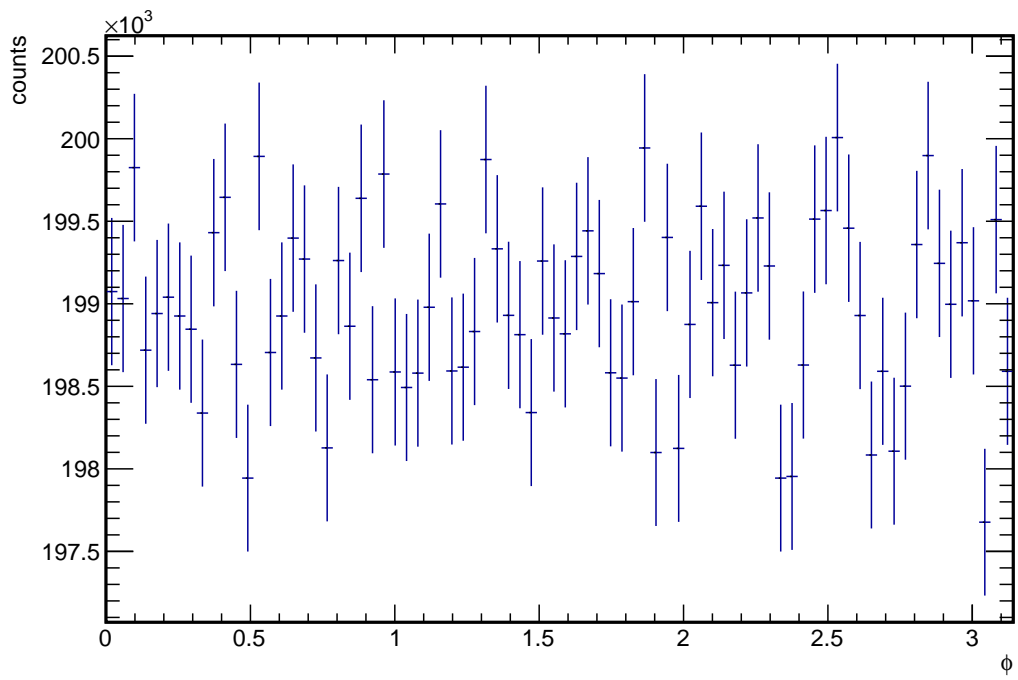


Figure 4.20: The  $\phi$  distribution of the event plane angle  $\Psi_{EP}$  after applying the shifting correction.

is done to get the correct value of  $v_2$  in flow analyses but we will also need the event plane resolution for calculating the event plane dependent  $v_2$  background for electron-hadron correlations. We calculate the resolution by subevent planes. We divide each event randomly into two equally sized sub events then independently calculate the event plane for each. The differences between the subevent planes can be used to measure the event plane resolution. Figure 4.21 summarizes the resolution as a function of event centrality as well for different hadron  $p_T$  slices. Resolution is best around 30% centrality and falls off in central events due to lower azimuthal anisotropy and in peripheral events because of lower multiplicity.

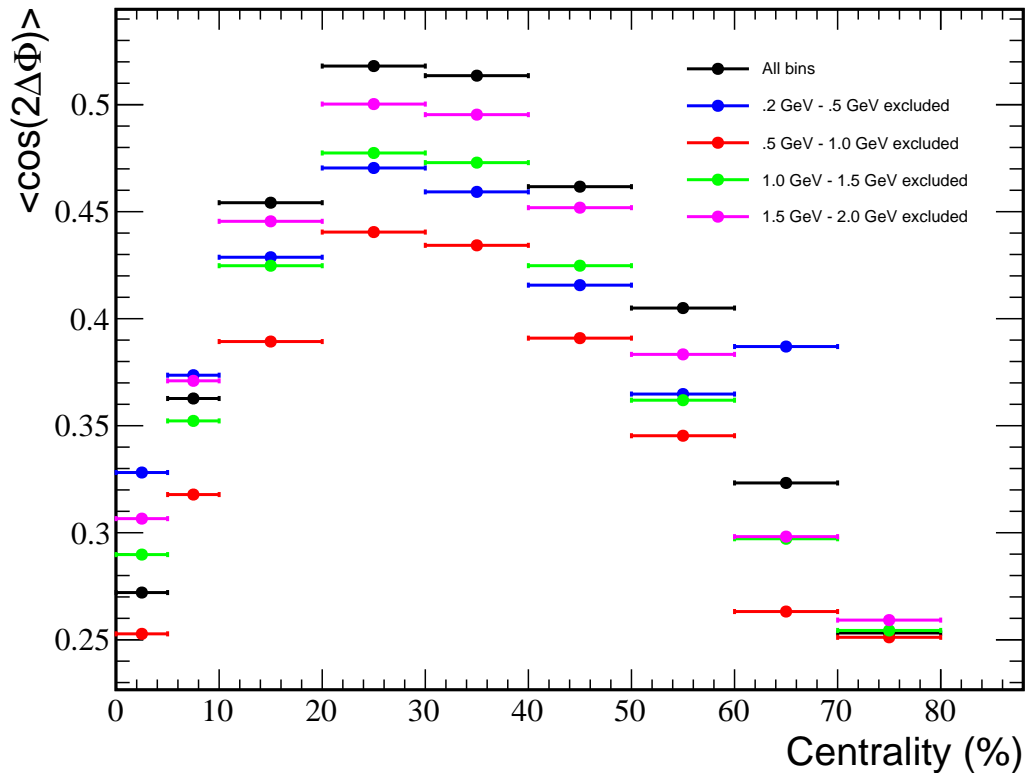


Figure 4.21: Event plane resolution as a function of centrality.

### 4.7.2 Correlations

Now we would like to calculate the NPE-h correlation and look at the dependence based on how the trigger particle is oriented relative to the event plane. Since for trigger particles which are out of the event plane the heavy quark traversed a longer path in medium, we might wonder if this could effect the correlation.

The correlation is constructed as previously described for Au+Au collisions with one important difference. Before the background from flow assumed no dependence of the trigger particle on the reaction plane. The form of this background resulted from the dependence on the reaction plane cancelling leaving only the difference  $\Delta\phi$  between the correlated particles. Now we are choosing specific orientations of the trigger particle relative to the event plane and thus the background will be different and depend on that orientation.

We use the same functional form for the background, Equation 4.1, as when we originally calculated the NPE-h correlations in Au+Au, but now we replace the  $v_2$  of the electron with an “effective”  $v_2$ , denoted  $\tilde{v}_2$ , which will depend on the electrons angle relative to the event plane as well as the event plane resolution. The effective  $v_2$  can be calculated for any arbitrary slice relative to the event plane, but we will only consider the case of two equal slices: in-plane and out-of-plane. For this case  $\tilde{v}_2$  is given by:

$$0 \leq |\phi_{trig} - \Psi_{EP}| \leq \frac{\pi}{4} : \tilde{v}_2 = \frac{\pi v_2 + 2\langle \cos(2\Delta\Psi) \rangle}{\pi + 4v_2\langle \cos(2\Delta\Psi) \rangle} \quad (4.9)$$

$$\frac{\pi}{4} \leq |\phi_{trig} - \Psi_{EP}| \leq \frac{\pi}{2} : \tilde{v}_2 = \frac{\pi v_2 - 2\langle \cos(2\Delta\Psi) \rangle}{\pi - 4v_2\langle \cos(2\Delta\Psi) \rangle} \quad (4.10)$$

where Equation 4.9 is for in-plane triggers and Equation 4.10 is for out-of-plane triggers.

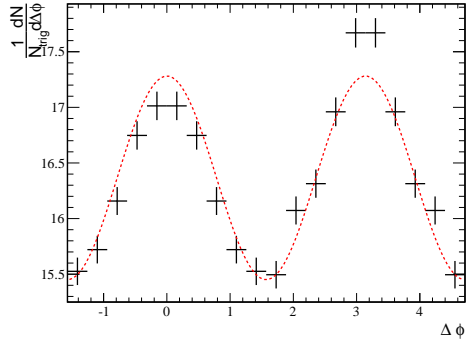
Now we construct the raw correlations for two cases: The trigger particle is

in-plane or out-of-plane and then subtract off the appropriate background for that case. We use the ZYAM method to normalize the bckground to the distributions, calculating each case individually. In principle it is possible to calculate what the normalization for each case should be just from the normalization of the background for all triggers, but we choose not to do this. When combining bins in centrality we calculate  $\tilde{v}_2$  from the average values in each bin, weighted by the number of NPE in each centrality bin.

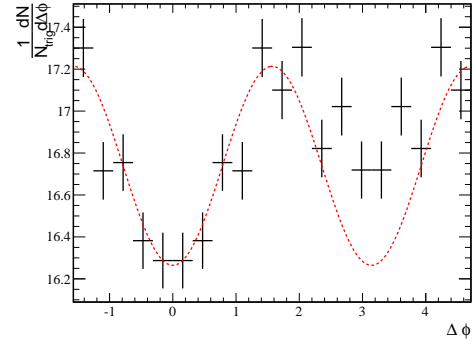
We construct the raw correlation for 20-60% central events. This is the region with the best event plane resolution due to the large elliptic flow and high multiplicity. It is also similar to the centrality region investigated by previous analyses of event plane dependent dihadron correlations. Figure 4.22 shows the resulting raw correlations for both cases and the dependence on the associated hadron  $p_T$ . We can also see how the background changes between in-plane and out-of-plane cases. For out-of-plane triggers the background appears shifted by  $\pi/2$  since the effective  $v_2$  has a negative value. This is not always the case though as for bins with large  $v_2$  but poor event plane resolution we could potentially find that  $\tilde{v}_2$  for out-of-plane triggers is still positive.

We can then subtract the backgrounds to get the correlations and yields to see if there is any significant difference between the in-plane and out-of-plane cases. The systematic errors from photonic eletron reconstruction efficiency and background normalization are calculated exactly as before. For the uncertainty in NPE  $v_2$  we again let the value vary between .05 and .15 calculate  $\tilde{v}_2$  for the extreme values and then take the difference between the points when fit with different backgrounds as the uncertainty.

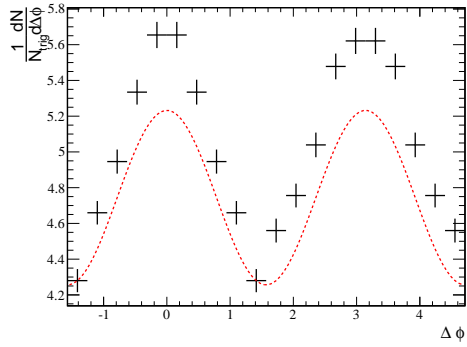
We can see from the subtracted distributions in Figure 4.23 that systematic uncertainties are quite large for lower hadron  $p_T$ . Above 2 GeV/c the uncertainties are less of a problem and this also happens to be the exact region looked at by a previous STAR analysis in dihadron collisions. In Figure 4.24 we show



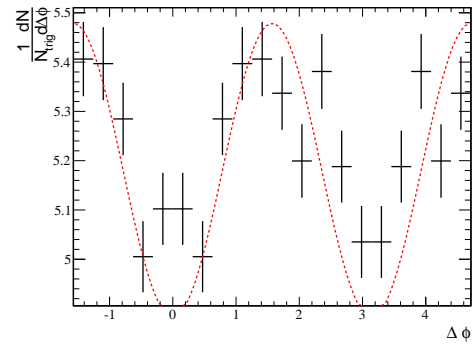
(a)  $.5 \text{ GeV}/c \leq p_{T,h} \leq 1.0 \text{ GeV}/c$



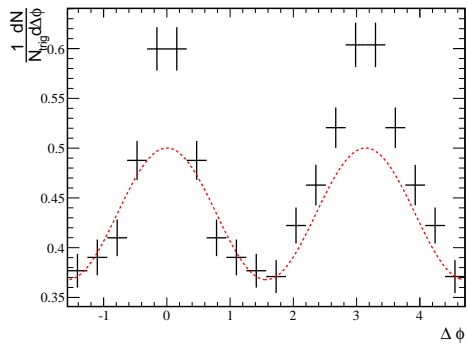
(b)  $.5 \text{ GeV}/c \leq p_{T,h} \leq 1.0 \text{ GeV}/c$



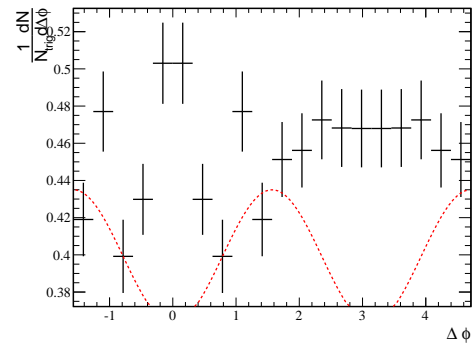
(c)  $1.0 \text{ GeV}/c \leq p_{T,h} \leq 2.0 \text{ GeV}/c$



(d)  $1.0 \text{ GeV}/c \leq p_{T,h} \leq 2.0 \text{ GeV}/c$



(e)  $2.0 \text{ GeV}/c \leq p_{T,h} \leq 4.0 \text{ GeV}/c$



(f)  $2.0 \text{ GeV}/c \leq p_{T,h} \leq 4.0 \text{ GeV}/c$

Figure 4.22: Raw NPE-h correlations for 20-60% centrality Au+Au collisions with  $4.0 \text{ GeV}/c \leq p_{T,e} \leq 6.0 \text{ GeV}/c$ . Left column shows correlations for in-plane electrons, right shows out-of-plane electrons.

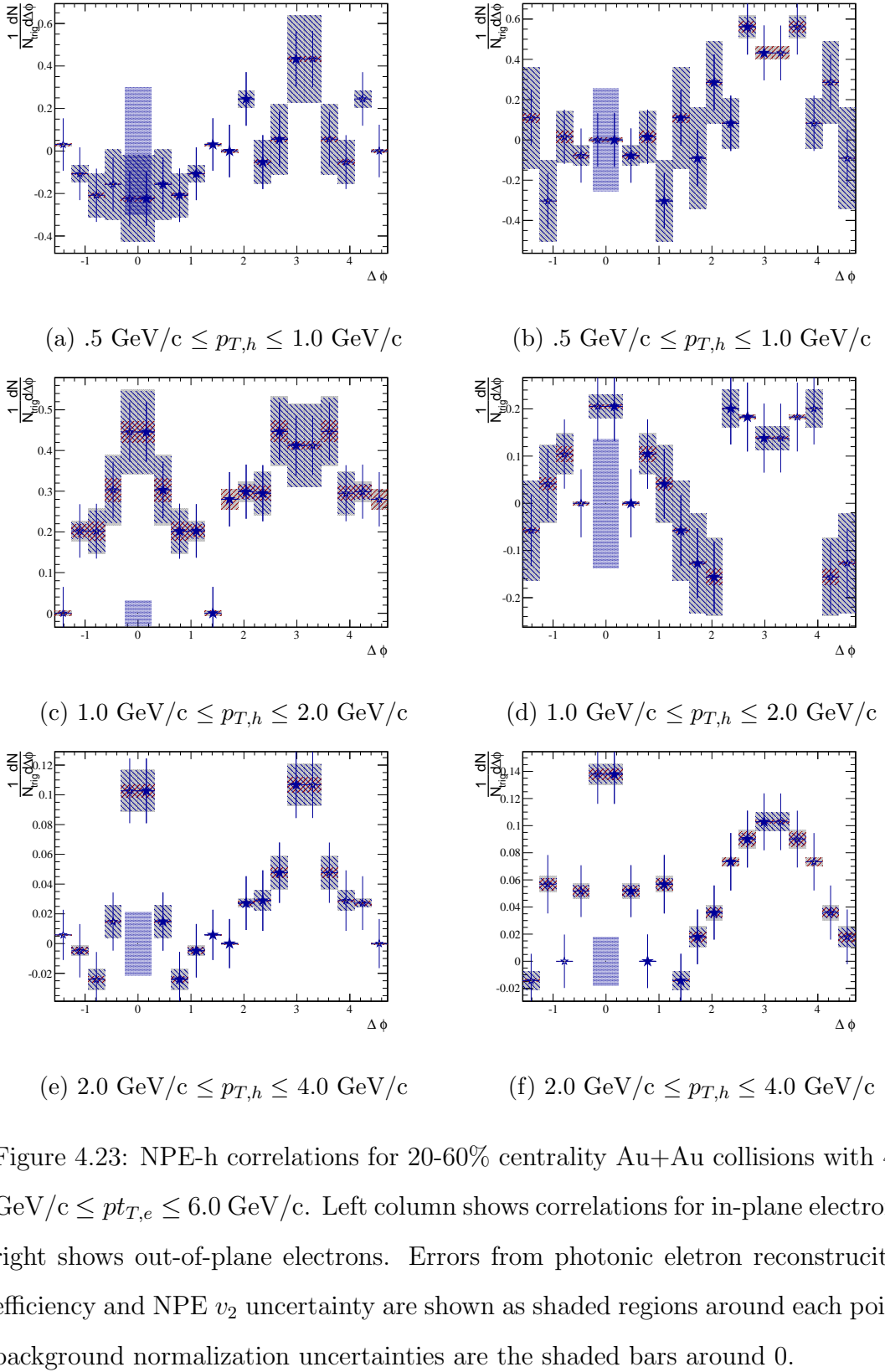


Figure 4.23: NPE-h correlations for 20-60% centrality Au+Au collisions with  $4.0 \text{ GeV}/c \leq p_{T,e} \leq 6.0 \text{ GeV}/c$ . Left column shows correlations for in-plane electrons, right shows out-of-plane electrons. Errors from photonic electron reconstruction efficiency and NPE  $v_2$  uncertainty are shown as shaded regions around each point, background normalization uncertainties are the shaded bars around 0.

the comparison of in-plane and out-of-plane correlations for NPE-h as well as dihadron correlations, p+p dihadron correlations are also shown. For the dihadron correlations only the statistical errors are shown. We see that while in dihadron correlations there is evidence of greater jet suppression in the out-of-plane correlations, there does not appear to be any discernable difference between in-plane and out-of-plane in NPE-h correlations. In fact, the NPE-h correlations appear comparable to the dihadron p+p data. There are a few possible explanations for this. The NPE-h correlation contains the decay products of the heavy  $B$  or  $D$  meson which happens after the freezeout of the QGP. Also in heavy flavor correlations the connection of the kinematics of the leading particle to the initial heavy quark is more tenuous, and the biases in these correlations may be different. We won't draw any definitive conclusions from these data and instead just present them as potential avenues for further study.

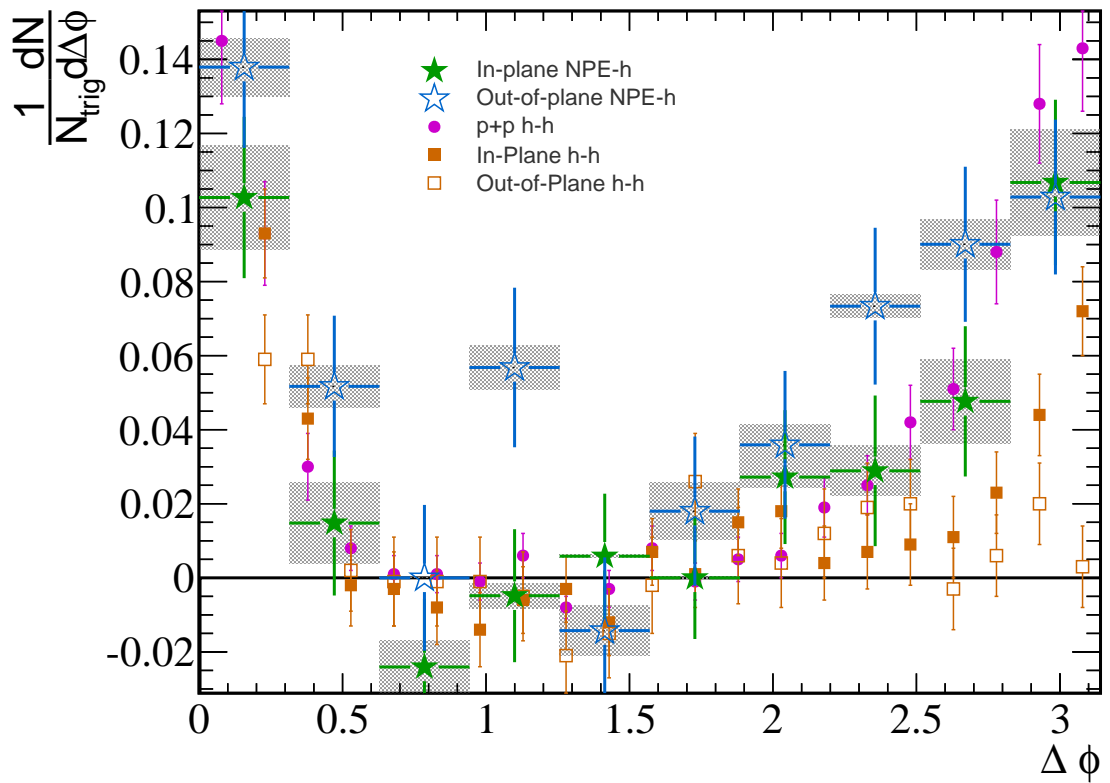


Figure 4.24: In-plane and out-of-plane correlations comparison for NPE-h and dihadron correlations.

# CHAPTER 5

## Conclusion

We have made measurements of azimuthal correlations between non-photonic electrons and hadrons in both Au+Au and p+p collisions. Results have improved statistics over previous studies allowing for more us to examine the correlations across centrality and  $p_T$  bins. This was possible due to the large statistics collected in STAR run 11 as well as improved condition of the TPC relative to run 10. We compared the away side jet shapes in Au+Au to collisions in p+p. We see some evidence for broadening of the away side peak in central Au+Au collisions. We also looked at the ratio of yields ( $I_{AA}$ ) between Au+Au and p+p as a function of associated particle  $p_T$  and collision centrality, but did not see any strong trend in these measurements.

We have also looked at correlations relative to the event plane to look for direction dependent jet suppression as a result of different path lengths through the medium. Interpretation of the results is difficult in part due to large systematic errors mainly from uncertainty in the non-photonic electron  $v_2$ , but in the one bin with large statistics and small systematic error we see no significant difference between the in-plane and out-of-plane cases unlike what was seen in dihadron correlations. The possibility still remains that the correlation shapes are the result of the decay products of the parent mesons. The relation of the kinematics of the final state particles to the underlying hard process are also different between light flavor and heavy flavor and this further complicates direct comparisons between the two measurements.

Upgrades at STAR and RHIC should improve our ability to measure two particle correlations in the heavy flavor sector and improve the insights we can make. The current STAR Au+Au program will provide a dataset even larger than run 11 and with the Heavy Flavor Tracker will greatly increase the ability to reconstruct  $D$  mesons. With these improved tools we can hope to construct two particle correlations ( $D$ -h, e-e, e- $\mu$ ,  $D$ - $D$ , etc.) which more directly probe the kinematics of the initial heavy quarks and create measurements which are easier to interpret and compare with theoretical models of heavy quark energy loss in quark gluon plasma.

## REFERENCES

- [1] X. Dong, “Open Charm Production at RHIC.” *Nucl. Phys. A* **774**, 343 (2006).
- [2] M. Gyulassy, M. Plumer, “Jet Quenching in Dense Matter.” *Phys. Lett. B* **243**, 4 (1990).
- [3] M. Beddo et al., “The STAR Barrel Electromagnetic Calorimeter.” *Nucl. Instrum. Methods* **499**, 725 (2003).
- [4] M. Anderson et al., “The STAR Time Projection Chamber: A Unique Tool for Studying High Multiplicity Events at RHIC.” *Nucl. Instrum. Methods* **499**, 659 (2003).
- [5] J. Adams et al., “Azimuthal Anisotropy in Au+Au Collisions at  $\sqrt{s_{NN}} = 200$  GeV.” *Phys. Rev. C* **72**, 014904 (2005).
- [6] A. Adare et al. “Azimuthal Correlations of Electrons from Heavy-Flavor Decay with Hadrons in p+p and Au+Au Collisions at  $\sqrt{s_{NN}} = 200$  GeV.” *Phys. Rev. C* **83**, 044912 (2011).
- [7] M.M. Aggarwal et al. “Measurement of the Bottom Quark Contribution to Nonphotonic Electron Production in p+p Collisions at  $\sqrt{s_{NN}} = 200$  GeV.” *Phys. Rev. Lett.* **105**, 202301 (2010).
- [8] M.M. Aggarwal et al. “Azimuthal Di-Hadron Correlations in d+Au and Au+Au Collisions at  $\sqrt{s_{NN}} = 200$  GeV Measured at the STAR Detector.” *Phys. Rev. C* **82**, 024912 (2010).
- [9] H. Agakishiev et al. “Measurements of Dihadron Correlations Relative to the Event Plane in Au+Au Collisions at  $\sqrt{s_{NN}} = 200$  GeV.” *Phys. Rev. C* **89**, 041901 (2014).
- [10] J. Adams et al., “Azimuthal Anisotropy and Correlations at Large Transverse Momenta in p+p and Au+Au Collisions at  $\sqrt{s_{NN}} = 200$  GeV.” *Phys. Rev. Lett.* **93**, 252301 (2004).
- [11] S.S. Adler et al., “Suppressed  $\pi^0$  Production at Large Transverse Momentum in Central Au+Au Collisions at  $\sqrt{s_{NN}} = 200$  GeV.” *Phys. Rev. Lett.* **91**, 7 (2003).